High Performance Hartree-Fock Exchange for Large and Condensed Phase Systems

Dissertation

zur

Erlangung der naturwissenschaftlichen Doktorwürde
(Dr. sc. nat.)

vorgelegt der

Mathematisch-naturwissenschaftlichen Fakultät

der

Universität Zürich

von

Manuel Guidon

von

Bergün GR

Promotionskomitee

Prof. Dr. Jürg Hutter (Vorsitz)

Dr. Joost VandeVondele (Leitung der Dissertation)

Prof. Dr. Markus Reiher

Zürich, 2010

Abstract

The objective of this thesis has been the development and implementation of algorithms that efficiently compute Hartree-Fock exchange (HFX) in extended systems. The motivation for this work is the observation that within the framework of density functional theory (DFT) most successful approximations for the treatment of exchange and correlation effects include a certain amount of HFX.
Much effort has been invested into reducing the formal fourth order scaling in computational cost with respect to system size to a linear one by employing several different screening techniques. Furthermore, a new methodology has been developed in order to retain efficiency when moving to large basis sets. In order to perform large scale condensed and liquid phase simulations, the gas phase formalism has been extended to periodic systems by developing a stable and accurate algorithm based on the Γ–point approximation.
Extensive serial performance optimization and an optimally load-balanced distribution of computational workload among many parallel processes based upon a hybrid `MPI/openMP` framework enables the algorithm to scale up to 64'000 compute-cores and beyond. Furthermore, highly efficient compression/decompression algorithms specifically targeted to integral storage have been developed in order to avoid evaluation of already computed integrals that are the main bottleneck in a HFX calculation.
This massively parallel implementation provides an important tool for investigating complex systems in gas and condensed phase within the framework of hybrid DFT. The applicability of the method has been demonstrated by extensive molecular dynamics simulations of liquid water, calculating fully solvated protein structures and determining properties of crystalline structures at the Hartree-Fock basis set limit.

Zusammenfassung

Ziel dieser Doktorarbeit war die Entwicklung und Implementierung von Algorithmen, welche es erlauben, die Hartree-Fock Austausch-Wechselwirkung in grossen Systemen auf effiziente Art und Weise zu berechnen. Die Motivation für diese Arbeit lässt sich dadurch begründen, dass die heutzutage besten Approximationen für das Austausch- und Korrelationsfunktional im Rahmen der Dichtefunktionaltheorie (DFT) auf der Miteinbeziehung eines gewissen Anteils von Hartree-Fock Austausch beruhen.
Da die Kosten für eine Hartree-Fock Rechnung in vierter Ordnung mit der Systemgrösse skalieren, wurden spezielle Selektionstechniken entwickelt, welche es ermöglichen diese Berechnungen linear in Bezug auf die Systemgrösse durchzuführen. Ausserdem wurde eine neue Methode eingeführt, dank derer es möglich ist diese Effizient auch unter Einbezug von sehr grossen Basissätzen beizubehalten. Um auch Simulationen von kondensierter oder flüssiger Materie zu ermöglichen, wurde die Standardformulierung der Theorie gasförmiger Systeme auf periodische Systeme erweitert und ein stabiler und akkurater Algorithmus basierend auf der Γ–Punkt Approximation entwickelt. Ferner wurde sehr viel Wert auf optimale serielle Performanz gelegt und durch fein abgestimmte Verteilung der einzelnen Arbeitsschritte auf mehrere Prozesse im Rahmen einer gemischten `MPI/openMP` Implementierung wurde es möglich die Methode so zu parallelisieren, dass sie auch auf mehr als 64'000 Prozessorkernen noch sehr gut skaliert. Desweiteren wurden hoch effiziente Kompressions- und Dekompressionsalgorithmen zur Speicherung von rechenaufwändigen Integralen entworfen, aufgrund derer eine Neuberechnung bereits vorhandener Integrale hinfällig wird.
Diese hoch parallelisierte Software ermöglicht es schliesslich komplizierte Systeme gasförmiger und kondensierter Materie innerhalb der hybrid Dichtefunktionaltheorie zu behandeln. Die Anwendbarkeit der Methode wurde am Beispiel ausgedehnter Moleküldynamik-Simulationen von Wasser in der Flüssigphase, Berechnungen von solvatisierten Proteinstrukturen sowie bei der Ermittlung von Eigenschaften kristalliner Strukturen erfolgreich unter Beweis gestellt.

Acknowledgement

I would like to thank Professor Jürg Hutter for giving me the opportunity to do my PhD in his group. His profound knowledge about the field was always a great help when there were problems.

It is hard to express my gratitude for my supervisor Dr. Joost VandeVondele and his support and encouragement from the beginning to the end of this work. Without his help and advice in understanding complex physical and computational problems, this project would not have been possible. His infectious enthusiasm turned even the unpleasant task of chasing bugs in the code into a cheerful experience. I very much enjoyed the many extended discussion about technical details and will sorely miss our daily coffee breaks. I hope he does not take it amiss that despite his various efforts my knowledge about chemistry did not improve significantly during the last four years.

I would like to thank my friend Florian who shared with me the ups and downs of life as a PhD student and who brought the extensively used coffee machine into our group.

Furthermore, I would like to offer my regards to all members of the working group being responsible for the great atmosphere at this working place.

Contents

1 Introduction **5**

I Theory and Implementation 8

2 Theory **9**
2.1 Wavefunction formalism 9
2.2 DFT formalism 16
2.3 Exchange-Correlation functionals 20

3 Implementation **28**
3.1 Gaussian basis sets 28
3.2 Integral evaluation 30
3.3 Scaling with respect to system size 30
3.4 Compression algorithm 32
3.5 Parallelization 32
3.6 Scaling with respect to basis set quality 40

II Validation, Benchmarks and Applications 42

4 Ab initio MD using hybrid density functionals **43**
4.1 Introduction 43
4.2 Theory 45
4.3 Methods 47
4.4 Benchmarks and validation 57
4.5 Symmetric radical cation dimers 66
4.6 Liquid water 68
4.7 Conclusions 75

5 Robust periodic Hartree-Fock Exchange for large scale simulations using Gaussian basis sets 77
5.1 Introduction 77
5.2 The truncated Coulomb operator for calculations at the Γ–point using Gaussian basis sets 79
5.3 Assessment and validation of the method 89
5.4 Conclusions 97
5.5 Appendix 99

6 Accurate Hartree-Fock energy of extended systems using large Gaussian basis sets 104
6.1 Introduction 104
6.2 Computational details 106
6.3 Results 112
6.4 Conclusions 117

7 Auxiliary Density Matrix Methods (ADMM) for Exact Exchange calculations 119
7.1 Introduction 119
7.2 Theory 122
7.3 Assessment and validation of the method 129
7.4 Summary 144
7.5 Appendix 145

8 Summary and Outlook 158
8.1 Summary 158
8.2 Outlook 159

Chapter 1

Introduction

Studying atoms and molecules *in silicio* has become more and more popular during the last decades. At small scale, quantum effects need to be taken into account in order to produce qualitatively and quantitatively acceptable results that can be used to support and/or explain experimental or theoretical predictions. In many applications, the underlying physics for that kind of problems is governed by the non-relativistic many body Schrödinger equation (SE). Once solved, this equation provides the wavefunction which is the relevant quantity at that level of theory and hence completely determines the behavior of the system under consideration.
However, due to the complexity of the SE, a straight forward algorithm for its solution scales exponentially with the system size and thus, several approximations are required. The theoretically most appealing methods directly work with the wavefunction of the system as the basic variable and there exist schemes that improve the quality of results by systematically enlarging the space of solutions until convergence is reached. These methods have unprecedented predictive power and can be considered as the most accurate strategies for including electron-electron correlation effects. However, the associated cost in terms of computer time that needs to be invested until the solution is available can be significant. Although most of nowadays applied algorithms scale polynomial with system size, they are, in practice, limited to 10 to 100 atoms depending on the applied algorithm and implementation details.

A different approach can be obtained by recognizing that the electron density contains exactly the same information as the corresponding wavefunction. The advantage of this formalism can be attributed to the fact that the electron density is completely defined by only three degrees of freedom while the wavefunction is a much more complicated object. The theoretical

framework behind this alternative formulation is called density functional theory (DFT) and has evolved to one of the most widely used methods for studying atoms and molecules at quantum mechanical level. If offers a reasonable trade-off between computational workload and accuracy of results. Most electronic structure programs based on DFT rely on so called linear scaling algorithms that allow scientists to treat fairly big systems at low cost and with respectable accuracy. It has become standard to perform molecular dynamics (MD) simulations with DFT for thousands of atoms and ten thousands of electrons,
However, although formulated as an exact theory in a general theoretical framework, DFT relies on some fundamental approximations concerning the correlation of electron-electron interactions. These approximations culminate in exchange and correlation functionals that are needed to model the behavior of electrons in the presence of others. Since, so far, there is no exact expression known for those parts of the energy, DFT stands and falls with the quality of the approximate exchange and correlation functionals. There exists a broad catalogue of functionals that perform differently depending on the specific physics of the underlying problem. Contrary to wavefunction theory there is no systematic procedure that allows to improve results in a satisfactory way. Although there exist some empirical guidelines of how to chose among the available approximations, this must be considered as the major drawback in DFT.
Wavefunction methods on the other side do not suffer from this conceptual problem. For the exchange part, there is an analytical expression available, namely Hartree-Fock exchange (HFX), and the correlation is usually explicitly treated as correlation between excited states. This methodology allows to treat electron-electron interactions at arbitrary precision but unfortunately comes along with much increased computational cost. Nevertheless, the wavefunction approach offers one pathway to improve DFT. Since up to 95 % of the non-classical electron-electron interaction energy can be assigned to the exchange energy, for which an analytical expression based on the electronic wavefunction exists, the obvious way of refining DFT is merging the two worlds. Indeed, many of the embarrassing failures of DFT can be resolved by taking wavefunction based exchange into account. These so called hybrid functionals typically consist of a certain fraction of HFX that is mixed with a standard DFT exchange functional. However, even though being a first order theory, HFX is computationally much more demanding than the most efficient DFT implementations available. In order to fruitfully combine both worlds, it is therefore crucial to have access to highly accurate and very efficient algorithms for the HFX part. All wavefunction parts should seamlessly integrate into the highly optimized existing parallel implementations

of DFT and, in addition, should not be limited by the applied boundary conditions (open or periodic). Providing such a framework to the scientific community was the main purpose of the present work.
This thesis consists of eight chapters. After this introduction the basic theoretical framework of DFT and Hartree-Fock will be summarized. Chapter three discusses some of the key algorithms that have been developed for the integration of HFX into existing DFT code and presents some specific implementation details. Chapters four to seven summarizes all publications resulting from this work which will as well give some examples of applications and discuss some implementation specific details. Finally all results will be recapitulated and an outlook, discussing how to adapt the methodology to future hardware and some ideas how to extend the algorithms will be presented.

Part I

Theory and Implementation

Chapter 2

Theory

This chapter reviews the basic theoretical concepts that build the foundation of wavefunction and density functional theory. Starting from the time-independent Schrödinger equation, the relevant formalism for Hartree-Fock and DFT used throughout this work will be derived. Special attention will be paid to the approximations within DFT and its failures in special cases. Furthermore, the theoretical background for periodic systems in the context of exact exchange will be discussed. A more detailed review of the topics can be found for example in the standard textbooks [1, 2, 3].

2.1 Wavefunction formalism

2.1.1 Born-Oppenheimer approximation

All properties of matter are governed by the time-dependent Schrödinger equation. However, if interactions between atoms, molecules and electrons do not explicitly depend on time, as it is the case throughout this work, it is sufficient to concentrate on its static counterpart. In addition, quantum mechanical modeling of matter typically assumes that materials consist of delocalized electrons moving in space around fixed classical nuclei. This simplification directly translates into a separation of the electronic and nuclear degrees of freedom in the underlying wavefunction. As a result, the solution of the Schrödinger equation decouples into a nuclear and a electronic part where the position of the nuclei enters parametrically. Under this assumptions, also referred to as Born-Oppenheimer (BO) approximation [4], the equation to solve reads

$$H(\mathbf{R})\Psi(\mathbf{x}) = E(\mathbf{R})\Psi(\mathbf{x}), \tag{2.1}$$

with the Hamiltonian H and the energy E being functions of the nuclear positions $\mathbf{R} = (\mathbf{R}_1, ..., \mathbf{R}_M)$ and the spin dependant electronic wavefunction Ψ with $\mathbf{x} = (\mathbf{r}_1, \sigma_1, ...\mathbf{r}_n, \sigma_N)$ containing spatial and spin coordinates. The Hamiltonian is uniquely defined by the number of electrons N and nuclei M and by their charges and has the following form (in atomic units):

$$H(\mathbf{R}) = -\frac{1}{2}\sum_{i=1}^{N}\nabla_i^2 - \sum_{A=1}^{M}\sum_{i=1}^{N}\frac{Z_A}{|\mathbf{r}_i - \mathbf{R}_A|} + \sum_{i<j}^{N}\frac{1}{|\mathbf{r}_i - \mathbf{r}_j|} + \sum_{A<B}^{M}\frac{Z_A Z_B}{|\mathbf{R}_A - \mathbf{R}_B|}. \tag{2.2}$$

Here, the first term is the electronic kinetic energy and the three other terms arise from the electron-nuclei, electron-electron and nuclei-nuclei interaction due to the Coulomb potential. The kinetic energy contribution of the nuclei can be neglected in the electronic Hamiltonian because the nuclei are assumed to be static, i.e. the electrons instantaneously adapt to the slowly moving cores. This simplification is assisted by the fact that the masses of electron and proton differ by three orders of magnitude. Based on the same reasoning, the last term describing the nuclei-nuclei interactions can be assumed to be constant and thus, has no effect on eigenfunctions and only results in a constant shift of eigenvalues. This part of the Hamiltonian will therefore be omitted in the following.
Even though the BO approximation decouples the nuclear and electronic motion, the solution of Eq. 2.1 is far from being trivial and can only analytically be solved for systems containing one electron. Therefore, further approximations are needed that will finally allow to take advantage of numerical methods in order to calculate properties of electronic systems.

2.1.2 Hartree-Fock approximation and variational principle

Since electrons belong to the class of Fermionic particles, the corresponding spin dependant wavefunction $\Psi(\mathbf{x})$ must be totally antisymmetric. Under the assumption that this wavefunction can be decomposed into a product of N orthonormal spin orbitals $\psi_i(\mathbf{x})$, the antisymmetry condition results in the following approximation

$$\Psi_{\mathrm{HF}} = \frac{1}{\sqrt{N!}}\begin{vmatrix} \psi_1(\mathbf{x}_1) & \psi_2(\mathbf{x}_1) & \dots & \psi_N(\mathbf{x}_1) \\ \psi_1(\mathbf{x}_2) & \psi_2(\mathbf{x}_2) & \dots & \psi_N(\mathbf{x}_2) \\ \vdots & \vdots & \ddots & \vdots \\ \psi_1(\mathbf{x}_N) & \psi_2(\mathbf{x}_N) & \dots & \psi_N(\mathbf{x}_N) \end{vmatrix}, \tag{2.3}$$

also known as Hartree-Fock approximation.
The energy of an electronic system is defined via Eq. 2.1 and given as a function of Ψ

$$E[\Psi] = \frac{\langle\Psi| H |\Psi\rangle}{\langle\Psi|\Psi\rangle}, \tag{2.4}$$

with the expectation value

$$\langle\Psi| H |\Psi\rangle = \int \Psi^*(\mathbf{x}) H(\mathbf{R}) \Psi(\mathbf{x}) d\mathbf{x}. \tag{2.5}$$

Let E_0 define the ground state energy corresponding to the ground state wavefunction $\Psi_0(\mathbf{r})$. By definition, it immediately follows for a trial wavefunction $\tilde{\Psi}$

$$E[\tilde{\Psi}] \geq E_0, \tag{2.6}$$

i.e. the energy given by $\tilde{\Psi}$ is always an upper bound for the ground state energy. Thus, one can rewrite Eq. 2.1 as a variational problem,

$$E_0 = \min_{\Psi} E[\Psi], \tag{2.7}$$

where the minimization is done with respect to the space of all valid N–electron wavefunctions.
In this context, the Hartree-Fock ground state energy E_{HF} is defined as the minimum of the expectation value for the Hamiltonian with respect to the spin orbitals $\psi_i(\mathbf{x})$

$$E_{\mathrm{HF}} = \min_{\psi_i} \langle\Psi_{\mathrm{HF}}| H |\Psi_{\mathrm{HF}}\rangle \tag{2.8}$$

under the constraint that the spin orbitals ψ_i are orthonormalized

$$\int \psi_i^*(\mathbf{x}) \psi_j(\mathbf{x}) d\mathbf{x} = \delta_{ij}. \tag{2.9}$$

The Hartree-Fock expectation value of the energy in the Born Oppenheimer approximation is found to be

$$E_{\mathrm{HF}} = \langle\Psi_{\mathrm{HF}}| H |\Psi_{\mathrm{HF}}\rangle = \sum_{i=1}^{N} H_i(\mathbf{R}) + \frac{1}{2} \sum_{i,j,i\neq j}^{N} (J_{ij} - K_{ij}) \tag{2.10}$$

with the following one- and two-electron integrals

$$H_i(\mathbf{R}) = \int \psi_i^*(\mathbf{x}) \left[-\frac{1}{2}\nabla^2 + v(\mathbf{x}, \mathbf{R}) \right] \psi_i(\mathbf{x}) d\mathbf{x} \tag{2.11}$$

$$J_{ij} = \int\int \psi_i(\mathbf{x}_1) \psi_i^*(\mathbf{x}_1) \frac{1}{|\mathbf{r}_2 - \mathbf{r}_1|} \psi_j^*(\mathbf{x}_2) \psi_j(\mathbf{x}_2) d\mathbf{x}_1 d\mathbf{x}_2 \tag{2.12}$$

$$K_{ij} = \int\int \psi_i^*(\mathbf{x}_1) \psi_j(\mathbf{x}_1) \frac{1}{|\mathbf{r}_2 - \mathbf{r}_1|} \psi_i(\mathbf{x}_2) \psi_j^*(\mathbf{x}_2) d\mathbf{x}_1 d\mathbf{x}_2, \tag{2.13}$$

where the external potential $v(\mathbf{x}, \mathbf{R})$ collects the electron-nuclei interactions. The two-center integrals J_{ij} and K_{ij} are also called Hartree- and Exchange-integrals respectively.

2.1.3 The Roothaan equations

Restricted closed-shell Hartree-Fock

So far, the Hartree-Fock approximation has been discussed within the framework of a general set of spin-orbitals $\psi_i(\mathbf{x})$. These spin-orbitals can be expanded into products of orthonormal spatial orbitals, only depending on the spatial coordinates $\mathbf{r}_i$ and in two orthonormal spin functions, corresponding to the electron spin pointing either up or down, i.e.

$$\psi_i(\mathbf{x}) = \begin{cases} \psi_i^{\alpha}(\mathbf{r}_i)\alpha(\sigma_i) \\ \psi_i^{\beta}(\mathbf{r}_i)\beta(\sigma_i) \end{cases} , \tag{2.14}$$

where the superscripts α and β accommodate the fact that the spatial part could be spin dependant. Without loss of generality, restricted closed-shell systems will be discussed in the following. In that case, only an even number of N of electrons is considered which all doubly occupy the spatial orbitals. The energy expression Eq. 2.10 thus becomes

$$E_{\mathrm{HF}} = 2\sum_{k=1}^{N/2} H_k + \sum_{k,l=1}^{N/2} (2J_{kl} - K_{kl}) \tag{2.15}$$

where the spin part has been integrated out and the one- and two-center integrals are now purely spatial

$$H_k = \int \psi_i^*(\mathbf{r}) \left[-\frac{1}{2}\nabla^2 + v(\mathbf{r}, \mathbf{R}) \right] \psi_i(\mathbf{r}) d\mathbf{r} \tag{2.16}$$

$$J_{ij} = \int\int \psi_i(\mathbf{r}_1)\psi_i^*(\mathbf{r}_1) \frac{1}{|\mathbf{r}_2 - \mathbf{r}_1|} \psi_j^*(\mathbf{r}_2)\psi_j(\mathbf{r}_2) d\mathbf{r}_1 d\mathbf{r}_2 \tag{2.17}$$

$$K_{ij} = \int\int \psi_i^*(\mathbf{r}_1)\psi_j(\mathbf{r}_1) \frac{1}{|\mathbf{r}_2 - \mathbf{r}_1|} \psi_i(\mathbf{r}_2)\psi_j^*(\mathbf{r}_2) d\mathbf{r}_1 d\mathbf{r}_2, \tag{2.18}$$

Plugging these results into the minimization problem of Eq. 2.8 yields the so called Hartree-Fock equations

$$F(\mathbf{r})\psi_k(\mathbf{r}) = \sum_{l=1}^{N/2} \epsilon_{kl}\psi_l(\mathbf{r}), \tag{2.19}$$

with the Fock-operator F defined as

$$F(\mathbf{r}) = -\frac{1}{2}\nabla^2 + v(\mathbf{r}) + j(\mathbf{r}) - k(\mathbf{r}), \tag{2.20}$$

and the action of j and k on an arbitrary function $f(\mathbf{r_1})$ given by

$$j(\mathbf{r}_1)f(\mathbf{r_1}) = 2\sum_{m=1}^{N/2}\int |\psi(\mathbf{r_2})|^2 \frac{1}{|\mathbf{r}_2 - \mathbf{r}_1|} d\mathbf{r}_2 f(\mathbf{r}_1) \tag{2.21}$$

$$k(\mathbf{r}_1)f(\mathbf{r}_1) = \sum_{m=1}^{N/2}\int \psi_m^*(\mathbf{r}_2)f(\mathbf{r}_1) \frac{1}{|\mathbf{r}_2 - \mathbf{r}_1|} d\mathbf{r}_2 \psi_m(\mathbf{r}_1) \tag{2.22}$$

The matrix ϵ can be interpreted as the Lagrangian multipliers associated with the orthonormality constraint Eq. 2.9. Furthermore, the operator $j - k$ can be interpreted as an effective one-electron operator $v^{\mathrm{HF}}(\mathbf{r}_1)$. It is the average potential experienced by an electron at position $\mathbf{r}_1$ due to the presence of all the other electrons. The essence of the Hartree-Fock approximation is to treat the electron-electron interactions in this mean-field approach. As a consequence, the Fock operator applied to the i-th electron, itself depends on the spatial orbitals of all the others. Thus, the Hartree-Fock equations are highly non-linear and need to be solved self consistently. The procedure of solving this problem is called self-consistent field (SCF) method. By making an initial guess for the orbitals ψ_k, the potential v^{HF} can be calculated, which again gives rise to a new set of orbitals. This procedure is then repeated until self-consistency has been reached, i.e. the orbitals do not change any longer.

Introduction of a basis

Since the operator F is hermitian, it is possible, via unitary transformation, to bring Eq. 2.19 into canonical form

$$F(\mathbf{r})\psi_k(\mathbf{r}) = \epsilon_k \psi_k(\mathbf{r}). \tag{2.23}$$

In order to solve these differential equations numerically, they can be transformed algebraically into a matrix eigenvalue equation. This can be achieved by introducing a set of basis functions, by means of which the wavefunctions can be expanded into molecular orbitals

$$\psi_k(\mathbf{r}) = \sum_{\nu} C_{\nu k}\phi_\nu(\mathbf{r}), \tag{2.24}$$

with the molecular (MO) coefficients $C_{\nu k}$. However, for practical reasons, the set $\{\phi_\nu\}$ cannot be chosen to be complete and the number of basis functions is

thus finite. With this ansatz, the canonical Hartree-Fock equations Eq. 2.23 transform into

$$F(\mathbf{r}) \sum_{\nu} C_{\nu k} \phi_{\nu}(\mathbf{r}) = \epsilon_k \sum_{\nu} C_{\nu k} \phi_{\nu}(\mathbf{r}). \tag{2.25}$$

Setting $\mathbf{r} = \mathbf{r}_1$ and by multiplication by $\phi^*_{\mu}(\mathbf{r}_1)$ from the left and integration, this becomes the desired matrix equation

$$\sum_{\nu} C_{\nu k} \int \phi^*_{\mu}(\mathbf{r}_1) F(\mathbf{r}_1) \phi_{\nu}(\mathbf{r}_1) d\mathbf{r}_1 = \epsilon_k \sum_{\nu} C_{\nu k} \int \phi^*_{\mu}(\mathbf{r}_1) \phi_{\nu}(\mathbf{r}_1) d\mathbf{r}_1. \tag{2.26}$$

With the definition of the Fock Matrix

$$F_{\mu\nu} = \int \phi^*_{\mu}(\mathbf{r}_1) F(\mathbf{r}_1) \phi_{\nu}(\mathbf{r}_1) d\mathbf{r}_1 \tag{2.27}$$

and the overlap matrix

$$S_{\mu\nu} = \int \phi^*_{\mu}(\mathbf{r}_1) \phi_{\nu}(\mathbf{r}_1) d\mathbf{r}_1 \tag{2.28}$$

this finally reads

$$\sum_{\nu} F_{\mu\nu} C_{\nu k} = \epsilon_k \sum_{\nu} S_{\mu\nu} C_{\nu k}. \tag{2.29}$$

These are the so called Roothaan equations [5] which can be written in compact matrix notation

$$FC = SC\epsilon. \tag{2.30}$$

2.1.4 The exchange part

For what follows, only the expression of the Fock matrix for the exchange part will be required. For that purpose, a matrix representation for the electron density is needed. The electron density $\rho(\mathbf{r})$ is defined as a probability distribution function describing the probability of finding an electron in a volume element $d\mathbf{r}$ around the point $\mathbf{r}$ and can be expressed in terms of the wavefunction

$$\rho(\mathbf{r}) = 2 \sum_{i}^{N/2} |\psi_i(\mathbf{r})|^2. \tag{2.31}$$

In a basis set representation with MO coefficients $C_{\mu i}$, this becomes

$$\begin{aligned} \rho(\mathbf{r}) &= 2 \sum_{i}^{N/2} \psi^*_i(\mathbf{r}) \psi_i(\mathbf{r}) = \sum_{\mu\nu} \left[2 \sum_{i}^{N/2} C_{\mu i} C^*_{\nu i} \right] \phi_{\mu}(\mathbf{r}) \phi^*_{\nu}(\mathbf{r}) \\ &= \sum_{\mu\nu} P_{\mu\nu} \phi_{\mu}(\mathbf{r}) \phi^*_{\nu}(\mathbf{r}), \end{aligned} \tag{2.32}$$

with the density matrix elements $P_{\mu\nu}$. Using this notation, the exchange part of the Fock matrix, F^{x} reads

$$F^{\mathrm{x}}_{\mu\nu} = -\frac{1}{2}\sum_{\lambda\sigma} P_{\lambda\sigma} \int\int \phi^*_\mu(\mathbf{r}_1)\phi_\lambda(\mathbf{r}_1)\frac{1}{|\mathbf{r}_1-\mathbf{r}_2|}\phi_\sigma(\mathbf{r}_2)\phi_\nu(\mathbf{r}_2)d\mathbf{r}_1 d\mathbf{r}_2. \quad (2.33)$$

Throughout this thesis, the following notation will be used for the two-electron integrals

$$(\phi_\mu\phi_\nu|\phi_\lambda\phi_\sigma) = (\mu\nu|\sigma\lambda) = \int\int \phi^*_\mu(\mathbf{r}_1)\phi_\nu(\mathbf{r}_1)\frac{1}{|\mathbf{r}_1-\mathbf{r}_2|}\phi_\lambda(\mathbf{r}_2)\phi_\sigma(\mathbf{r}_2)d\mathbf{r}_1 d\mathbf{r}_2. \quad (2.34)$$

The Hartree-Fock exchange energy can thus be expressed as

$$E_x^{\mathrm{HF}} = -\frac{1}{2}\sum_{\mu\nu\lambda\sigma} P_{\mu\sigma}P_{\nu\lambda}(\mu\nu|\lambda\sigma). \quad (2.35)$$

2.1.5 Correlation energy

Since the Hartree-Fock approximation can be interpreted as a mean-field theory, the electron-electron interactions are not treated exactly. While the correlation among same-spin electrons due to the Pauli-principle is fully included through the exchange term in the energy expression, the correlation arising from other electron-electron interactions is completely absent. This deficiency arises from the fact that the true underlying wavefunction is never a single determinant or a linear combination of a few determinants. The resulting error in energy is called correlation energy and is defined as

$$E_{\mathrm{c}}^{\mathrm{HF}} = E_{\mathrm{exact}} - E_{\mathrm{HF}}. \quad (2.36)$$

Several methods have been developed in order to improve upon Hartree-Fock results. These so called post-Hartree-Fock methods typically start with the Hartree-Fock wavefunction as a reference and try to improve upon it. Among them is perturbation theory that treats correlation as a perturbation of the Fock operator. Other methods expand the electron wave function in terms of a linear combination of Slater determinants such as configuration interaction or use an exponential ansatz based on a excitation operator (coupled cluster) in order to obtain correlation corrected results. All above stated methodologies have in common that they can systematically be improved either by enlarging the perturbation expansion or by taking higher excitations into account. However, this improved accuracy comes along with the price of significant increase in computational cost.

Although correlation is not treated at an adequate level, the Hartree-Fock approximation provides an analytical expression for the exchange energy which is usually orders of magnitudes larger than the correlation counterpart. Eq. 2.35 can thus be defined as the exact exchange energy, or briefly, exact exchange, and will be reused in the context of hybrid density functionals later on.

2.2 DFT formalism

2.2.1 Density functional theory

Density functional theory is based on the discovery [6, 7, 8, 9] that the complicated N-electron wavefunction $\Psi(\mathbf{r}) = \Psi(\mathbf{r}_1, \mathbf{r}_2, ..., \mathbf{r}_N)$ can be replaced by the much more convenient electron-density $\rho(\mathbf{r})$ defined as

$$\rho(\mathbf{r}) = \rho(\mathbf{r}_1) = N \int d\mathbf{r}_2 \int d\mathbf{r}_3 ... \int d\mathbf{r}_N \Psi^*(\mathbf{r}_1, \mathbf{r}_2, ..., \mathbf{r}_N)\Psi(\mathbf{r}_1, \mathbf{r}_2, ..., \mathbf{r}_N). \tag{2.37}$$

The above relation does as well hold for the ground-state wavefunction

$$\Psi_0(\mathbf{r}) = \Psi_0(\mathbf{r}_1, \mathbf{r}_2, ..., \mathbf{r}_N) \tag{2.38}$$

and the ground-state density $\rho_0(\mathbf{r})$.
The remarkable Hohenberg-Kohn theorems [10] now state, that the above expression is invertible for ground states, i.e. given the ground-state density ρ_0 it is possible to reconstruct the underlying wavefunction $\Psi_0(\mathbf{r})$, and thus both functions have to be considered as equivalent. In terms of complexity of the problem, that means that a function of only one spatial variable contains the same information as the complicated wavefunction that depends on N spatial variables.
It also implies that the ground-state density must minimize the energy of the system, and thus gives raise to a variational formulation in terms of the density. Particularly, for any trial density $\tilde{\rho}(\mathbf{r})$ it must hold

$$E[\tilde{\rho}] \geq E_0 \tag{2.39}$$

The starting point for the derivation of a minimization problem is again the Schrödinger equation in the BO approximation

$$(T + U + V)\Psi(\mathbf{x}) = E\Psi(\mathbf{x}), \tag{2.40}$$

with the abbreviations

$$T = -\frac{1}{2}\sum_{i}^{N}\nabla_i^2 \tag{2.41}$$

$$U = \sum_{i<j}^{N}\frac{1}{|\mathbf{r}_i - \mathbf{r}_j|} \tag{2.42}$$

$$V = \sum_{A=1}^{M}\sum_{i=1}^{N}\frac{Z_A}{|\mathbf{r}_i - \mathbf{R}_A|} = \sum_{i=1}^{N} v(\mathbf{r}_i) \tag{2.43}$$

for kinetic energy, electron-electron interaction and electron-nuclei interaction respectively. The minimization problem in terms of the density now reads

$$\begin{aligned} E[\rho] &= \min_{\Psi\to\rho}\langle\Psi|\, T+U+V\,|\Psi\rangle \\ &= \min_{\Psi\to\rho}\langle\Psi|\, T+U\,|\Psi\rangle + \int \rho(\mathbf{r})v(\mathbf{r})d\mathbf{r} \\ &=: F[\rho] + \int \rho(\mathbf{r})v(\mathbf{r})d\mathbf{r}. \end{aligned} \tag{2.44}$$

The ground-state density is the density that minimizes this expression and fulfills thus the Euler equation

$$\mu = v(\mathbf{r}) + \frac{\delta F[\rho]}{\delta\rho(\mathbf{r})}, \tag{2.45}$$

where μ is the Lagrange multiplier associated with the particle conservation constraint

$$\int \rho(\mathbf{r})d\mathbf{r} = N. \tag{2.46}$$

The above energy expression $E[\rho]$ is an exact reformulation of the original Schrödinger equation in terms of the electron density and can, in principle, be used to calculate properties of electronic systems. However, since there is no known closed form expression for the functional $F[\rho]$ available, further approximations have to be made.
The unknown functional $F[\rho]$ in Eq. 2.44 can be decomposed as follows

$$F[\rho] = T[\rho] + U[\rho] = T[\rho] + J[\rho] + E_{\mathrm{nc}}[\rho], \tag{2.47}$$

where J denotes the classical Hartree term, also present in the Hartree-Fock approximation and E_{nc} contains all non-classical electron-electron interaction

energies, among them the exchange energy as well present in the Hartree-Fock approximation.
Despite this decomposition, the problem of finding expressions for the kinetic energy functional and the non-classical part remains. The Thomas-Fermi (TF) model [6, 7] is a first approximation. It makes the rather crude assumptions that the non-classical electron-electron interactions are zero and that the kinetic energy $T[\rho]$ can be obtained from the theory of a non-interacting uniform electron gas. As a next step, in the Thomas-Fermi-Dirac (TFD) approximation [6, 7, 11], the non-classical term is approximated by the exchange-energy formula for the uniform electron gas. Both approximations suffer from their underlying simplifications and typically perform much worse than the Hartree-Fock approximation. The missing correlation term results in the unphysical prediction that the energy of isolated atoms is lower than in bounded systems. In addition, the construction of an accurate model for the kinetic energy $T[\rho]$ turns out to be very difficult.

2.2.2 Kohn-Sham equations

In contrast to the direct approach in the TF and TFD model, Kohn and Sham invented an indirect approach [12] in order to compute the kinetic energy $T[\rho]$. The basic idea behind their ansatz is to split the kinetic energy into a part that can easily and accurately be calculated, and a small remainder, which can be handled separately.
This can be achieved by considering a non-interacting reference system in which no electron-electron interactions are present but the corresponding ground-state electron density is exactly the same as the interacting one. In this case, Eq. 2.40 simplifies to

$$(T_s + V)\Psi_s(\mathbf{x}) = E_s\Psi_s(\mathbf{x}). \tag{2.48}$$

The advantage of introducing the reference system is the fact, that within this approach an analytical formula for the kinetic energy, T_s is available in terms of orbitals, namely

$$T_s[\rho] = \sum_{i=1}^{N} \langle\psi_i| - \frac{1}{2}\nabla^2 |\psi_i\rangle \tag{2.49}$$

As a side effect, the introduction of orbitals provides a practical way to calculate the density matrix in terms of the orbitals:

$$\rho(\mathbf{r}) = \sum_{i=1}^{N} |\psi_i(\mathbf{x})|^2. \tag{2.50}$$

$T_s[\rho]$ can now be used to repartition Eq. 2.47

$$F[\rho] = T_s[\rho] + J[\rho] + E_{\text{xc}}[\rho], \tag{2.51}$$

with

$$E_{\text{xc}}[\rho] = T[\rho] - T_s[\rho] + E_{\text{nc}}[\rho]. \tag{2.52}$$

E_{xc} is the so called exchange-correlation functional and contains the non-classical part of the electron-electron interaction as well as the missing correlation in the non-interacting kinetic energy.
The orbital dependant energy functional now reads

$$E[\rho] = \sum_{i=1}^{N} \int \psi_i^*(\mathbf{x}) \left(-\frac{1}{2}\nabla^2\right) \psi_i(\mathbf{r}) d\mathbf{x} + J[\rho] + E_{\text{xc}}[\rho] + \int v(\mathbf{r})\rho(\mathbf{r}) d\mathbf{r}. \tag{2.53}$$

As in standard DFT, the variational principle is still valid, and the ground-state density minimizes this expression. Due to the introduction of orbitals, the constraint of Eq. 2.46 has to be replaced by

$$\int \psi_i^*(\mathbf{x})\psi_j(\mathbf{x}) d\mathbf{x} = \delta_{ij}. \tag{2.54}$$

Minimizing Eq. 2.53 with respect to this orthonormality constraint and assuming restricted closed-shell configurations, yields the Kohn-Sham equations

$$K(\mathbf{r})\psi_k(\mathbf{r}) = \sum_{l=1}^{N/2} \epsilon_{kl}\psi_l(\mathbf{r}), \tag{2.55}$$

with the Kohn-Sham operator K defined as

$$K(\mathbf{r}) = -\frac{1}{2}\nabla^2 + v_{\text{eff}}(\mathbf{r}) \tag{2.56}$$

and

$$v_{\text{eff}}(\mathbf{r}) = v(\mathbf{r}) + \frac{\delta J[\rho]}{\delta\rho(\mathbf{r})} + \frac{\delta E_{\text{xc}}[\rho]}{\delta\rho(\mathbf{r})} \tag{2.57}$$

$$= v(\mathbf{r}) + \int \frac{\rho(\mathbf{r}')}{|\mathbf{r} - \mathbf{r}'|} d\mathbf{r}' + v_{\text{xc}}(\mathbf{r}), \tag{2.58}$$

with the exchange-correlation potential v_{xc}.
Similar as in the Hartree-Fock approximation, since $K(\mathbf{r})$ is hermitian, it is possible, via unitary transformation, to bring Eq. 2.55 into canonical form

$$K(\mathbf{r})\psi_k(\mathbf{r}) = \epsilon_k\psi_k(\mathbf{r}). \tag{2.59}$$

Again, introduction of a finite basis set transforms these equations into a matrix eigenvalue problem, that can be solved numerically.

2.2.3 Comparison with Hartree-Fock

Eq. 2.23 and Eq. 2.59 look very similar from a structural point of view. They both have to be solved in a SCF approach because the operators on the left hand side both depend on the solution of the corresponding eigenvalue problem. However, since the Kohn-Sham formalism is, in principle, exact it allows to incorporate correlation effects in a very convenient way, namely through the exchange-correlation functional. On the other hand, the Hartree-Fock approximation completely lacks of a description of such effects and they can only be incorporated using very demanding post-Hartree-Fock methods. Furthermore, the evaluation of the Kohn-Sham operator is much cheaper in terms of computational costs, since the exchange contributions do not rely on evaluating two-center electron integrals and efficient techniques exist for the Coulomb part (see for example [13, 14, 15, 16, 17].
However, Kohn-Sham theory stays and falls with the quality of the exchange-correlation functional. Contrary to post-Hartree-Fock methods, there is no systematic scheme for improvements available and the accuracy of results strongly depends on the choice of an appropriate approximated functional.

2.3 Exchange-Correlation functionals

There is, so far, no closed form expression available for the exchange and correlation functional $E_{\mathrm{xc}}[\rho]$ and developing good approximations is a very active field in the DFT community. As a consequence there exists a whole universe of density functionals based on different approximations and models. Most of the available functionals can be divided into three classes

- Local functionals,
- Semi-local functionals and
- Hybrid functionals

This section will discuss some of the few known analytical properties of the exchange-correlation energy and will briefly present some of the underlying approximations.

2.3.1 General considerations

The adiabatic connection

Consider a parameterization that controls the strength of the electron-electron interaction U in the minimization problem Eq. 2.44

$$F_\lambda[\rho] = \min_{\Psi\to\rho} \langle\Psi|\, T + \lambda U \,|\Psi\rangle = \langle\Psi_\lambda|\, T + \lambda U \,|\Psi_\lambda\rangle\,. \tag{2.60}$$

Assuming the partitioning of the Kohn-Sham ansatz, this immediately yields

$$F_0[\rho] = T_s[\rho], \quad \text{and} \quad F_1[\rho] = F[\rho] = T_s[\rho] + J[\rho] + E_{\mathrm{xc}}[\rho], \tag{2.61}$$

or

$$E_{\mathrm{xc}}[\rho] = F_1[\rho] - F_0[\rho] - J[\rho]. \tag{2.62}$$

The last equation can be written in integral form and the result is known as the adiabatic connection [18, 19, 20, 21]

$$E_{\mathrm{xc}}[\rho] = \int_0^1 \frac{\partial F_\lambda[\rho]}{\partial\lambda} d\lambda - J[\rho]. \tag{2.63}$$

In order to calculate the exchange-correlation energy, an expression for the partial derivative is required. It turns out, that this quantity is related to the expectation value of the electron-electron interaction operator U

$$\frac{\partial F_\lambda[\rho]}{\partial\lambda} = \langle\Psi_\lambda|\, U \,|\Psi_\lambda\rangle\,. \tag{2.64}$$

In order to simplify this expression, the concept of reduced density matrices has to be introduced.

Reduced density matrices and expectation values

The density matrix of an N electron system is defined via its wavefunction

$$\begin{aligned} \gamma_N(\mathbf{x}', \mathbf{x}) &= \gamma_N(\mathbf{x}'_1\mathbf{x}'_2\cdots\mathbf{x}'_N, \mathbf{x}_1\mathbf{x}_2\cdots\mathbf{x}_N) \\ &= \Psi^*(\mathbf{x}'_1\mathbf{x}'_2\cdots\mathbf{x}'_N)\Psi(\mathbf{x}_1\mathbf{x}_2\cdots\mathbf{x}_N) \end{aligned} \tag{2.65}$$

Based on that definition, one can obtain reduced density matrices of order p by integrating over $N-p$ variables

$$\gamma_p(\mathbf{x}'_1\mathbf{x}'_2\cdots\mathbf{x}'_p, \mathbf{x}_1\mathbf{x}_2\cdots\mathbf{x}_p) = \binom{N}{p} \int\cdots\int \gamma_N(\mathbf{x}, \mathbf{x}') d\mathbf{x}_{p+1}\cdots d\mathbf{x}_N. \tag{2.66}$$

A similar definition holds for spinless reduced density matrices and the expressions for the special cases $p = 1$ and $p = 2$ are given by

$$\rho_1(\mathbf{r}'_1, \mathbf{r}_1) = \int \gamma_1(\mathbf{r}'_1\sigma_1, \mathbf{r}_1\sigma_1) d\sigma_1 \tag{2.67}$$

$$\rho_2(\mathbf{r}'_1\mathbf{r}'_2, \mathbf{r}_1\mathbf{r_2}) = \int\int \gamma_2(\mathbf{r}'_1\sigma_1\mathbf{r}'_2\sigma_2, \mathbf{r}_1\sigma_1\mathbf{r}_2\sigma_2) d\sigma_1 d\sigma_2 \tag{2.68}$$

This notation allows to express expectation values of spinless local one- and two-particle operators

$$O_1 = \sum_{i=1}^{N} O_1(\mathbf{r}_i) \tag{2.69}$$

$$O_2 = \sum_{i<j} O_2(\mathbf{r}_i, \mathbf{r}_j) \tag{2.70}$$

in a very convenient way via traces

$$\begin{aligned} \langle O_1 \rangle &= \mathrm{tr}(O_1 \rho_N) \\ &= \int [O_1(\mathbf{r}_1)\rho_1(\mathbf{r}'_1, \mathbf{r}_1)]_{\mathbf{r}'_1=\mathbf{r}_1} \, d\mathbf{r}_1 d\mathbf{r}_2 \end{aligned} \tag{2.71}$$

$$\begin{aligned} \langle O_2 \rangle &= \mathrm{tr}(O_2 \rho_N) \\ &= \int\int [O_2(\mathbf{r}_1\mathbf{r}_2)\rho_2(\mathbf{r}'_1\mathbf{r}'_2, \mathbf{r}_1\mathbf{r}_2)]_{\mathbf{r_1}'=\mathbf{r}_1, \mathbf{r}'_2=\mathbf{r}_2} \, d\mathbf{r}_1 d\mathbf{r}_2. \end{aligned} \tag{2.72}$$

Exchange-correlation holes

The concept of second order reduced density matrices allows to rewrite the expectation value for the electron-electron interaction energy:

$$\begin{aligned} \langle U \rangle &= \int\int \frac{1}{|\mathbf{r}_2 - \mathbf{r}_1|} \rho_2(\mathbf{r}_1\mathbf{r}_1, \mathbf{r}_2\mathbf{r}_2) d\mathbf{r}_1 d\mathbf{r}_2 \\ &= \int\int \frac{1}{|\mathbf{r}_2 - \mathbf{r}_1|} \rho_2(\mathbf{r}_1, \mathbf{r}_2) d\mathbf{r}_1 d\mathbf{r}_2 \end{aligned} \tag{2.73}$$

Since $J[\rho]$, as a part of $U[\rho]$, denotes the classical electron-electron interaction it is given as

$$J[\rho] = \frac{1}{2} \int\int \frac{1}{|\mathbf{r}_2 - \mathbf{r}_1|} \rho(\mathbf{r}_1)\rho(\mathbf{r}_2) d\mathbf{r}_1 d\mathbf{r}_2 \tag{2.74}$$

i.e. as the Hartree energy of a charge distribution $\rho(\mathbf{r})$ in a Coulomb potential. This suggests to define the diagonal second order reduced density

matrix $\rho_2(\mathbf{r}_1, \mathbf{r}_2)$ in terms of a pair correlation function that describes all non-classical effects

$$\rho_2(\mathbf{r}_1, \mathbf{r}_2) = \frac{1}{2}\rho(\mathbf{r}_1)\rho(\mathbf{r}_2)\left[1 + h(\mathbf{r}_1, \mathbf{r}_2)\right]. \tag{2.75}$$

With this terminology, the expression for the exchange-correlation energy in Eq. 2.64 becomes

$$\begin{aligned} E_{\mathrm{xc}}[\rho] &= \int_0^1 \langle\Psi_\lambda| U |\Psi_\lambda\rangle \, d\lambda - J[\rho] \\ &= \frac{1}{2}\int\int \frac{1}{|\mathbf{r}_2 - \mathbf{r}_1|}\int_0^1 \rho_2^\lambda(\mathbf{r}_1, \mathbf{r}_2)d\lambda - \frac{1}{2}\int\int \rho(\mathbf{r}_1)\rho(\mathbf{r}_2)d\mathbf{r}_1 d\mathbf{r}_2 \\ &= \frac{1}{2}\int\int \frac{1}{|\mathbf{r}_2 - \mathbf{r}_1|}\rho(\mathbf{r}_1)\rho(\mathbf{r}_2)\int_0^1 h^\lambda(\mathbf{r}_1, \mathbf{r}_2)d\lambda d\mathbf{r}_1 d\mathbf{r}_2 \\ &= \frac{1}{2}\int\int \frac{1}{|\mathbf{r}_2 - \mathbf{r}_1|}\rho(\mathbf{r}_1)\rho_{\mathrm{xc}}(\mathbf{r}_1, \mathbf{r}_2)d\mathbf{r}_1 d\mathbf{r}_2, \end{aligned} \tag{2.76}$$

with the exchange-correlation hole $\rho_{\mathrm{xc}}(\mathbf{r}_1, \mathbf{r}_2) = \rho(\mathbf{r}_2)\int_0^1 h^\lambda(\mathbf{r}_1, \mathbf{r}_2)d\lambda$. Comparison with Eq. 2.74 suggests to interpret this result as the classical Coulomb interaction of a charge distribution $\rho(\mathbf{r})$ and the exchange correlation hole $\rho_{\mathrm{xc}}(\mathbf{r}_1, \mathbf{r}_2)$.
The exchange correlation hole has the important property that it obeys a sum rule

$$\int \rho_{\mathrm{xc}}(\mathbf{r}_1, \mathbf{r}_2)d\mathbf{r}_2 = -1. \tag{2.77}$$

Furthermore, the exchange-correlation energy only depends on the spherically averaged behavior of $\rho_{\mathrm{xc}}(\mathbf{r}_1, \mathbf{r}_2)$, i.e

$$E_{\mathrm{xc}}[\rho] = \frac{1}{2}\int \rho(\mathbf{r})\int_0^\infty 4\pi s\rho_{\mathrm{xc}}^{SA}(\mathbf{r}, s)dsd\mathbf{r}, \tag{2.78}$$

where s denotes the electron electron distance. This expression for $E_{\mathrm{xc}}[\rho]$ will turn out later on, to be a good starting point for generalizations to interaction potentials different from Coulombic, for example truncated Coulomb or short-range erfc type potentials. For practical reasons, the exchange-correlation hole is typically partitioned into a exchange and a correlation part, ρ_x and ρ_c respectively. Since the Hartree-Fock approximation gives an exact expression for exchange, one obtains, by comparison, the following two sum rules

$$\int \rho_x(\mathbf{r}_1, \mathbf{r}_2)d\mathbf{r}_2 = -1, \quad \text{and} \quad \int \rho_c(\mathbf{r}_1, \mathbf{r}_2)d\mathbf{r}_2 = 0, \tag{2.79}$$

which can be used to assess the quality of models for each hole.

Self interaction error (SIC)

The Hamiltonian Eq. 2.2 reflects the fact that there is no self-interaction present for identical electrons by removing such interactions by explicitly summing over $i < j$. In the Hartree-Fock approximation, this self-interaction term is exactly canceled because it is present in both, the Hartree- and the Exchange term. However, in DFT, where these terms are defined via integrals over charge distributions and modeled exchange-correlation holes, it is much harder to avoid spurious self-interaction contributions. This leads to unphysical delocalization of the electronic wavefunction. Although there exist schemes that try to avoid or reduce this self-interaction error, there is no procedure available that generally fixes that problem.

2.3.2 Local functionals

Historically, the most important type of approximation for the exchange correlation functional is the so called local-density approximation (LDA). It is based on considerations of the homogeneous electron gas, because in that case, the exchange energy density e_x^{hom} is known in closed form [11]

$$e_x^{\text{hom}} = -\frac{3}{4}\left(\frac{3}{\pi}\right)^{1/3}\rho^{4/3}, \tag{2.80}$$

where ρ is constant. The generalization to the inhomogeneous system is then done by assuming a locally constant electron density (thus the name local density approximation)

$$e_x^{\text{inhom}}(\mathbf{r}) = -\frac{3}{4}\left(\frac{3}{\pi}\right)^{1/3}\rho(\mathbf{r})^{4/3}. \tag{2.81}$$

Integration over all space yields

$$E_x^{\text{LDA}}[\rho] = -\frac{3}{4}\left(\frac{3}{\pi}\right)^{1/3}\int \rho(\mathbf{r})^{4/3}d\mathbf{r}. \tag{2.82}$$

The situation for the correlation energy is slightly different. Unfortunately, no analytical expression for the correlation density e_c^{hom} exists. However, expressions for the high and low density limit are available, and values in-between can be fitted to highly accurate quantum Monte Carlo calculations [22]. The final expression reads

$$e_c^{\text{hom}} = \begin{cases} \frac{\gamma_c}{1+\beta_1\sqrt{r_s}+\beta_2 r_s}, & r_s > 1 \\ A\ln r_s + B + Cr_s\ln r_s + Dr_s, & r_s < 1 \end{cases} \tag{2.83}$$

with

$$r_s = \left[\frac{3}{4\pi\rho}\right]^{1/3} \tag{2.84}$$

and some constants $A, B, C, D, \gamma_c, \beta_1$, and β_2. The total correlation energy is then obtained in a similar fashion as for the exchange energy by assuming locally constant electron density.
Despite the rather crude approximations, LDA does perform quite respectably in terms of the accuracy of results. The reason behind this surprising finding is the fact that every LDA exchange-correlation hole does obey the sum-rules from Sec. 2.3.1. As a consequence there is a systematic error cancellation between the typically overestimated exchange and underestimated correlation part.

2.3.3 Semi-local functionals

The LDA approximation only incorporates the knowledge of the density at a certain point $\mathbf{r}$ in space and assumes a certain spatial homogeneity of the electron density $\rho(\mathbf{r})$. However, any real physical system is typically inhomogeneous and has a varying density. In order to improve upon LDA, it might therefore help to include some information on the rate of how the density changes in space. This approach yields the so called gradient-expansion approximations (GEA) that try to exploit an expansion of the density in terms of its gradients or higher order derivatives. In practice, it turns out that it is firstly not easy to derive expressions for this expansions and secondly, results are typically even worse than in the LDA case.
A better approach is to consider a less systematic expansion, where the density and its gradients are allowed to appear in a more general functional way. Such functionals are of the form

$$E_{\mathrm{xc}}^{\mathrm{GGA}}[\rho] = \int e_{\mathrm{xc}}(\rho(\mathbf{r}), \nabla\rho(\mathbf{r}))d\mathbf{r} \tag{2.85}$$

where the exchange-correlation energy density e_{xc} is an arbitrary function of the density and its gradient. Since such models not only consider the density at a certain point in space but as well its local variation, such generalized gradient approximations (GGAs) are considered to be semi-local.
GGAs significantly improve upon the LDA and allow to describe most types of chemical bonds in a qualitatively and quantitatively acceptable fashion. It needs to be emphasized that similar as in the LDA case, most functionals benefit from an intrinsic systematic error cancellation among the exchange and correlation parts. Typically, the two parts itself do not obey the correspond-

ing sum rules, but in combination, the overall sum rule is approximately fulfilled. This effect can nicely be illustrated with the so called BLYP functional, a combination of Becke's 1988 exchange functional [23] and Lee, Yang and Parrs correlation functional [24]. In that case, the exchange approximation is known to have the wrong asymptotic decay for largely separated electrons while the correlation approximation severely violates the correlation-hole sum rule under this condition and actually turns into an exchange-hole from that point of view. However, the combination of both models seems to recover the correct analytical property and thus explains why BLYP is still one of the most widely used density functionals.
Even though GGA functionals made DFT a standard tool for studying a broad range of applications, two embarrassing failures remain unsolved: Firstly, common GGAs fail to describe weak van der Waals interactions, and secondly, more importantly, the problem of the self-interaction error remains unaddressed in most of nowadays popular functionals but can partially be solved by going to a non-local form of the exchange hole.

2.3.4 Hybrid functionals

The expressions for Hartree and kinetic energy are identical in Kohn-Sham and Hartree-Fock theory and differ only in the sense that the latter is evaluated in terms of Hartree-Fock orbitals instead of Kohn-Sham orbitals. Furthermore, Hartree-Fock provides an analytic expression for the exchange energy and has the favorable property of being self-interaction error free. It is therefore tempting to replace the approximated exchange functional $E_x^{\mathrm{DFT}}[\rho]$ in DFT with the corresponding orbital dependant $E_x^{\mathrm{HFX}}[\Psi]$ from Hartree-Fock theory. Due to the systematic error cancellations discussed in Sec. 2.3.2 and Sec. 2.3.3 this naive approach has the effect that deficiencies in the correlation functional are not compensated any longer and the gain in accuracy of the exchange description has only minor impact on the overall accuracy.
However, it is possible to mix only a certain fraction of Hartree-Fock exchange to the DFT energy expression and treat the reminder with an approximated exchange functional. Since the Hartree-Fock exchange operator Eq. 2.22 is non-local in nature, i.e. the exchange potential observed from an electron at a an arbitrary point in space depends on the average potential determined by all the others, these hybrid functionals build the class of so called non-local functionals.
The first successful hybrid functional has been suggested by Becke and was based on the adiabatic connection formula Eq. 2.63. At the point $\lambda = 0$ this expression yields the exchange energy of the Kohn-Sham system, while at $\lambda = 1$ the full exchange-correlation energy of the interacting system is

reached. The integral over the interaction strength parameter λ can be approximated using a simple quadrature formula based on the endpoints 0 and 1. Under the assumption that the exchange-correlation energy at the point $\lambda = 1$ is reasonably well described by a standard DFT functional this leads to the following expression for the Becke Half and Half hybrid functional (BH&HLYP) [25, 24]

$$E_{\mathrm{xc}}^{\mathrm{BHaH}}[\rho] = \frac{1}{2}\left(E_x^{\mathrm{HF}}[\rho(\psi_i)] + E_x^{\mathrm{GGA}}[\rho]\right) + E_c^{\mathrm{GGA}}[\rho]. \tag{2.86}$$

This expression can be generalized by introducing a parameter α which defines the fraction of Hartree-Fock that should be mixed to the DFT part:

$$E_{\mathrm{xc}}^{\mathrm{hybrid}}[\rho] = \alpha E_x^{\mathrm{HF}}[\rho] + (1-\alpha)E_x^{\mathrm{DFT}}[\rho] + E_c^{\mathrm{DFT}}[\rho]. \tag{2.87}$$

The marriage of wavefunction theory based exact exchange and DFT based models for exchange and correlation has proven to be very fruitful. Indeed, nowadays most successful density functionals are non-local in nature and include a certain fraction of Hartree-Fock exchange, among them B3LYP [26, 24, 27], PBE0 [28, 29, 30] or HSE06 [31, 32]. The reason for this improvement is the fact that many properties are overestimated by DFT and underestimated by HFX or vice versa and the mixture of both gives good intermediate results. Furthermore, adding a certain fraction of HFX reduces the self-interaction error and properties that rely on the qualitatively correct localization of the underlying wavefunction can significantly better be predicted.

Chapter 3

Implementation

The main purpose of this work was to implement fast and accurate algorithms that compute the Hartree-Fock exchange energy

$$E_x^{\mathrm{HFX}} = -\frac{1}{2}\sum_{\mu\nu\lambda\sigma} P_{\mu\sigma}P_{\nu\lambda}(\mu\nu|\lambda\sigma)_g \tag{3.1}$$

and its periodic counterpart in Γ–point approximation

$$E_x^{\mathrm{HFX},\Gamma} = -\frac{1}{2}\sum_{\mu\nu\lambda\sigma}\sum_{\mathbf{M},\mathbf{N},\mathbf{L}} P_{\mu\sigma}P_{\nu\lambda}(\mu\nu^{\mathbf{L}}|\lambda^{\mathbf{N}}\sigma^{\mathbf{M}+\mathbf{L}})_g \tag{3.2}$$

where g denotes a general potential of the form $g(|\mathbf{r}_2 - \mathbf{r}_1|)$.
At first sight, this seems to be a minor challenge because from a conceptual point of view all that needs to be done is calculating integrals and contract them with density matrix elements. However, the sheer enormity of number of integrals that have to evaluated, the amount of work scales with the fourth power in the number of contracted basis functions, makes a straight forward approach unfeasible. This chapter briefly presents the basic principles that have been used to reduce this workload and outlines the parallelization strategy that has been chosen. A more detailed discussion can be found in the second part of this thesis, where publications resulting from this work are presented.

3.1 Gaussian basis sets

As discussed in Sec. 2.1.3, introducing basis functions based on which the molecular orbitals are expressed is a key requirement for the numerical treatment of electronic systems. The most natural choice for such basis functions

are atom centered hydrogen-like exponential Slater functions $e^{-\alpha r}$ that are the analytical solutions of the single particle Schrödinger equation. However, since the calculation of the Fock matrix elements Eq. 2.27 involves many one- or two-center integrals, that cannot be evaluated analytically with this ansatz, one typically moves to Gaussian functions $e^{-\alpha r^2}$. In both cases, the parameter α, the exponent of the basis, defines the diffuseness of the basis. Small values of α imply a broader, more delocalized function while larger values imply a less diffuse, more localized function. The main difference of this two approaches lies in their asymptotic limit. Gaussian functions decay faster at large distance and do not have a finite slope at $r = 0$, i.e. they cannot describe the cusps around the center of an atom. From a physical point of view, Slater functions would thus be preferable, because they are known to resemble the exact hydrogenic solution. On the other hand Gaussian functions are more efficient because all occurring integrals can be calculated analytically with very fast algorithms. Using Gaussian functions, many basis functions would be needed in order to reproduce the behavior of one single Slater function. The solution to this problem is to use fixed linear combinations of primitive Gaussian functions that approximate the physical behavior of Slater functions. In general, such a contracted Cartesian Gaussian basis function centered around $\mathbf{A}$ can be written as

$$\phi_\nu(\mathbf{r}-\mathbf{A}) = \sum_{i=1}^{L} c_i (x-A_x)^l (y-A_y)^m (z-A_z)^n e^{-\alpha_i(\mathbf{r}-\mathbf{A})^2}, \tag{3.3}$$

where L denotes the length of the contraction, c_i are the fixed contraction coefficients, the sum $l' = l+m+n$ refers to the Cartesian angular momenta and α_i defines the exponent. The wavefunction for an electron k centered around atom $\mathbf{A}$ can thus be expressed as

$$\psi_k(\mathbf{r}-\mathbf{A}) = \sum_\nu C_{\nu k} \sum_{i=1}^{L} c_i (x-A_x)^l (y-A_y)^m (z-A_z)^n e^{-\alpha_i(\mathbf{r}-\mathbf{A})^2}. \tag{3.4}$$

3.2 Integral evaluation

The introduction of contracted Cartesian Gaussian basis functions leads to six dimensional four-center integrals of the following form

$$\begin{aligned}(\mu\nu|\lambda\sigma)_g &= \sum_{a=1}^{L_A}\sum_{b=1}^{L_B}\sum_{c=1}^{L_C}\sum_{d=1}^{L_D}\int\int g(|\mathbf{r}_2-\mathbf{r}_1|) \\ &\cdot\ c_a(x-A_x)^{l_A}(y-A_y)^{m_A}(z-A_z)^{n_A} \\ &\cdot\ c_b(x-B_x)^{l_B}(y-B_y)^{m_B}(z-B_z)^{n_B} \\ &\cdot\ c_c(x-C_x)^{l_C}(y-C_y)^{m_C}(z-C_z)^{n_C} \\ &\cdot\ c_d(x-D_x)^{l_D}(y-D_y)^{m_D}(z-D_z)^{n_D} \\ &\cdot\ e^{-\alpha_a(\mathbf{r}-\mathbf{A})^2}e^{-\alpha_b(\mathbf{r}-\mathbf{B})^2}e^{-\alpha_c(\mathbf{r}-\mathbf{C})^2}e^{-\alpha_d(\mathbf{r}-\mathbf{D})^2}d\mathbf{r}_1 d\mathbf{r}_2 \qquad (3.5)\end{aligned}$$

i.e. each integral is a function of the atomic positions $\mathbf{A}, \mathbf{B}, \mathbf{C}, \mathbf{D}$, the angular momenta $l_A, l_B, l_C, l_D, m_A, m_B, m_C, m_D, n_A, n_B, n_C, n_D$ and the exponents $\alpha_a, \alpha_b, \alpha_c, \alpha_d$. Since a product of two atomic centered Gaussian functions with polynomial prefactor is again a Gaussian function with polynomial prefactor centered at a different position, the integrals are in fact two-center integrals and can be calculated analytically. Note that the number of integrals for a given system hence scales as the product of the number of basis functions N^4, the number of contractions $L_A \cdot L_B \cdot L_C \cdot L_D$ and the total number of angular momenta $\frac{1}{16} \cdot l'_A(l'_A+1) \cdot l'_B(l'_B+1) \cdot l'_C(l'_C+1) \cdot l'_D(l'_D+1)$, which can indeed become huge.
The actual calculation of above integrals is typically based on recurrence schemes such as the Obara-Saika method [33] or variations thereof. These recursive procedures take integrals of the $l' = 0$ basis functions, i.e. s-functions as initial starting point and produce the higher angular momentum integrals based on that input. A very efficient implementation of this scheme is provided via the external library `LIBINT` [34] which has been used throughout this work. This library can also be used in order to calculate derivatives with respect to atomic centers which is required for ionic force calculations in molecular dynamics or during geometry optimization procedures.

3.3 Scaling with respect to system size

Some DFT codes scale (quasi-) linearly with respect to system size N at least in the dominant part of solving the Kohn-Sham equations, namely the Kohn-Sham matrix construction. From that point of view, an implementation of Hartree-Fock exchange that scales with the fourth power in the number of

basis functions is of no practical use.
However, there are two observations that allow to circumvent this disadvantage. Firstly, if the spatial distance of the Gaussian products $\langle\mu\nu|$ and $|\lambda\sigma\rangle$, the codensities, becomes large, the associated two-center integrals $(\mu\nu|\lambda\sigma)_g$ become small. Secondly, depending on the specific properties of the system under consideration, the density matrix elements may or may not decay fast with respect to increasing inter-electronic distance r_{12}. Since the HFX energy is mainly computed as a product of these two objects, it becomes possible to significantly speed up calculations by avoiding taking negligible terms into account. This is achieved by applying so called screening techniques, namely integral screening and density matrix screening.
Both screening techniques are used to construct pair lists that only contain pairs of products $(\mu\nu|$ and $|\lambda\sigma)$ that give raise to non-negligible contributions to the exchange part of the Fock-matrix $F^x_{\nu\lambda} = \sum_{\mu\sigma} P_{\mu\sigma}(\mu\nu|\lambda\sigma)$. The criterion whether a pair needs to be added or not is based on an estimate of the value of $(\mu\nu|\lambda\sigma)$ which, since this is a well-defined scalar-product, can be obtained from the Schwarz inequality

$$|(\mu\nu|\lambda\sigma)| \leq \sqrt{|(\mu\nu|\mu\nu)| \cdot |(\lambda\sigma|\lambda\sigma)|}. \tag{3.6}$$

In practice, a threshold $\epsilon_{\text{schwarz}}$ is introduced and only pairs that have contributions larger than this threshold are added to the list. For efficiency reasons, this screening takes place at several hierarchies in the code. The highest level is defined by atomic sites, i.e. all pairs of basis functions that belong to the same atom are taken into account and if the estimate for the largest contribution within this estimate passes the screening, the basis functions for the corresponding atom are added to this atomic pair list. Since Gaussian basis functions are typically grouped into sets of same angular momenta or exponents, this naturally defines the second screening level. The maximum contributions of these set-set interactions are estimated and define set lists of integrals that have to computed. Finally, the lowest level of screening is defined at the level of the uncontracted primitive Gaussian functions (pgfs) and results in pgf pair lists.
The integral screening can be interpreted as a short-range screening and brings the computational cost down to $\mathcal{O}(N^2)$. If the interaction potential is chosen to be the truncated Coulomb potential, then an additional long-range screening can be applied. Since all interactions are truncated by the cutoff radius R_c all products of codensities that have a larger spatial separation than this cutoff are analytically zero. This long-range screening results in almost linear scaling. For other potentials, multi-pole expansions of the charge codensities are available and can be used for the same purpose but are usually not as efficient.

The screening on the density matrix is a little bit more involved. In order to be consistent throughout the SCF procedure, it is mandatory to use the same initial density matrix in all steps. This requires a good initial guess at the very beginning of the wavefunction optimization. However, in molecular dynamics (MD) simulations this requirement can easily be met by the usage of an extrapolated wavefunction obtained from previous time steps. For single point calculations, the initial guess is usually taken from a precomputed GGA calculation. For systems with a large band-gap, the density matrix decays exponentially with respect to spatial separation and is thus a very efficient way to further reduce the cost.

3.4 Compression algorithm

All integrals that have to be considered in a HFX calculation depend on the basis set parameters and the atomic positions in the system. During the SCF procedure they remain thus constant and only need to be calculated in the very first step. It is therefore advantageous to store them in a convenient way, that allows to re-read them from main memory in the subsequent steps. Since the calculation of these integrals is typically the bottleneck in a HFX calculation this procedure reduces the cost of a wavefunction optimization significantly. However, storing them in 64-bit floating point representation is rather memory consuming and actually not needed. The screening algorithms described in the previous section offer an estimate of the magnitude for the current bunch of integrals that needs to be calculated. This estimate together with the threshold $\epsilon_{\text{schwarz}}$ defines the number of bits that are needed to reproduce the integral values to within the desired precision. With this compression, the memory requirements can typically be reduced by a factor of 4 to 8, depending on the actual choice of $\epsilon_{\text{schwarz}}$. Fig. 3.1 illustrates this effect for a polyacetylene chain consisting of 30 carbon atoms.

3.5 Parallelization

Although the above introduced procedure scales linearly with respect to system size, there is still a large prefactor associated with the screening algorithms. In fact, for large systems, most of the time in the construction of $F^x_{\lambda\mu}$ is spent in estimating whether a bunch of integrals needs to be calculated or not. In order to apply the algorithm to large systems, a very fine tuned parallelization algorithm is required that distributes the total work among multiple CPUs.

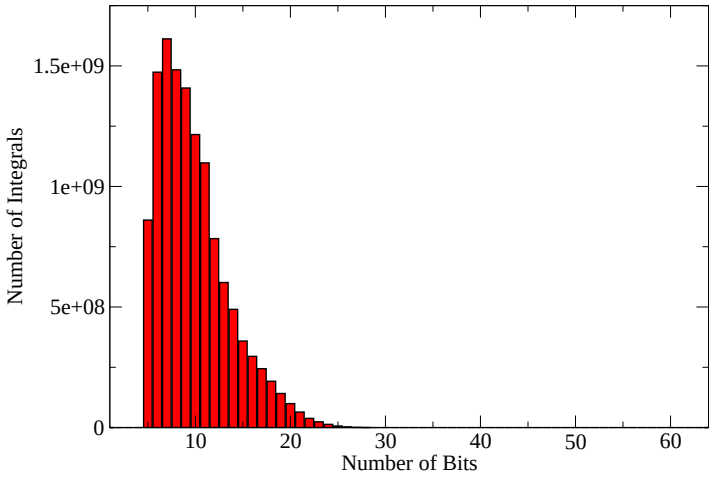

Figure 3.1: The graph shows a histogram of four center integrals with respect to the number of bits that are needed to store them in order to retain the accuracy of $\epsilon_{\text{schwarz}} = 10^{-8}$ All data are obtained from a calculation on a polyacetylene chain. Most of the integrals can be stored with sufficient accuracy using a 10 bit floating point representation and almost no integrals need to be stored with more than 23 bits, the mantissa of single precision floating point representation.

The current parallel implementation is optimized for hardware that consists of several nodes which are connected via fast interconnects and can communicate via the message passing interface (`MPI`). The nodes itself typically provide several CPUs in a multi-core environment with substantial amount of shared memory. Thus, within a node, shared memory parallelism (`openMP`) can be used which is much more efficient when data has to be exchanged among CPUs on the same node. In addition, this framework saves a lot of communication time because only the master process has to deal with `MPI` communication. This results in a higher bandwidth because only one computing entity needs to access the physical link, that would otherwise be shared among all CPUs of the node.

3.5.1 Units of work

In order to distribute all work among the CPUs, a cost model is needed that efficiently and accurately assigns costs to each unit of work. In the current

implementation, the basic unit is defined as a collection of batches of integrals into bins. Such a bin is defined as

$$\mathrm{bin}_i = -\frac{1}{2} \sum_{\mu_{\mathrm{start},i}}^{\mu_{\mathrm{end},i}} \sum_{\nu_{\mathrm{start},i}}^{\nu_{\mathrm{end},i}} \sum_{\lambda_{\mathrm{start},i}}^{\lambda_{\mathrm{end},i}} \sum_{\sigma_{\mathrm{start},i}}^{\sigma_{\mathrm{end},i}} P_{\mu\sigma} P_{\mu\lambda} \sum_{\mathbf{M},\mathbf{N},\mathbf{L}} (\mu\nu^{\mathbf{L}}|\lambda^{\mathbf{N}}\sigma^{\mathbf{M}+\mathbf{L}})_g, \tag{3.7}$$

i.e. all periodic images that are contracted with the same density-matrix element are contained in the same bin. Since, depending on species and its associated basis functions the cost for a bin can vary dramatically and is far from being homogeneously distributed, the bin sizes $\mu_{\mathrm{end}} - \mu_{\mathrm{start}}$, $\nu_{\mathrm{end}} - \nu_{\mathrm{start}}$, $\lambda_{\mathrm{end}} - \lambda_{\mathrm{start}}$ and $\sigma_{\mathrm{end}} - \sigma_{\mathrm{start}}$ need to be optimized in order to guarantee that there are no bins that are by order of magnitudes more expensive than others. This is achieved by recursively splitting the most expensive bins into smaller ones until the largest deviation from the mean cost is not higher than a given threshold, typically a factor of 1.5 to 2.

3.5.2 Cost model

In order to estimate the cost of a bin, a rather complicated empirical function has been developed that reliably predicts the computational workload of processing a bin. The model predicts the cost of all set based batches in a bin ($N_{\mathrm{set},i}$), i.e. all integrals that belong to the same set of Gaussian basis functions. It is determined by the number of Cartesian and spherical basis functions in each subset and depends on the threshold $\epsilon_{\mathrm{schwarz}} = \epsilon$ as well as on the screening estimates from the integral and density matrix screening. The functional form of the model is given as

$$\mathrm{cost}(\mathrm{bin}_i) = \sum_{j=1}^{N_{\mathrm{set},i}} f(ns_{\mu,i}, ns_{\nu,i}, ns_{\lambda,i}, ns_{\sigma,i}, nc_{\mu,i}, nc_{\nu,i}, nc_{\lambda,i}, nc_{\sigma,i}, EST, \epsilon), \tag{3.8}$$

where ns denotes the number of spherical functions and nc the number of Cartesian functions respectively in each set and EST is the estimate from the screening. The function f contains in total 26 fitting parameters that have been optimized with respect to actual CPU timings obtained from a representative benchmark system and reads

$$f = \frac{g(P_1)(1-F) + g(P_2)F}{1000} + 1 \tag{3.9}$$

where

$$\begin{aligned} g(P) &= g(p_1,p_2,p_3,p_4,p_5,p_6,p_7,p_8,p_9,p_{10},p_{11},p_{12}) \\ &= 1 + \left| \left[\prod_{a=\mu,\nu,\lambda,\sigma} h(ns_a,p_1,p_2,p_3) \cdot h(nc_a,p_1,p_2,p_3) \right] \cdot e^{-p_7 r + p_8 r^2} \right. \\ &+ \left. 1000p_9 + \prod_{a=\mu,\nu,\lambda,\sigma} h(ns_a,p_{10},p_{11},p_{12}) \right|, \end{aligned} \tag{3.10}$$

with

$$r = EST/\epsilon \tag{3.11}$$

$$h(x,\alpha,\beta,\gamma) = \alpha + \beta x + \gamma x^2 \tag{3.12}$$

$$F = F(f_1,f_2) = \frac{1}{1+e^{\frac{\log g(P_1)-f_1}{f_2}}} \tag{3.13}$$

and

$$f_1 = \log\left(|10^6 \cdot P_3(1)| + 1\right) \tag{3.14}$$

$$f_2 = \frac{P_3(2)}{10} \cdot f_1. \tag{3.15}$$

The rational behind this functional form can be explained as follows: The cost for a given batch is determined by the actual calculation of Cartesian integrals, which is roughly given by its number, $nc_\mu \cdot nc_\nu \cdot nc_\lambda \cdot nc_\sigma$, and the number of spherical integrals $ns_\mu \cdot ns_\nu \cdot ns_\lambda \cdot ns_\sigma$ that need to be contracted with the density matrix elements. The exponential term depends on the ratio between screening estimate and threshold and takes into account that the screening estimate might not be optimal in the sense that only few integrals within a subset are actually larger than the threshold. The last term in the function g that only depends on the number of spherical functions takes the memory usage into account. Since only spherical integrals will be compressed and stored, it is important that there is a certain memory load balance among the CPUs. If one CPU is running out of memory because it has to store too many integrals, it will start calculating them on the fly which would result in a tremendous slowdown of the SCF procedure. The fact that the estimate for the cost is given by a Fermi switching function consisting of two parts depending on two different parameter sets P_1 and P_2 is borrowed from the theory of artificial neural networks. Tab. 3.1 lists all 26 parameters that have been obtained using a Powell optimizer. Since also forces are involved in some applications, the table contains as well the parameter sets for that

case.
Fig. 3.2 depicts the correlation between actual cost and the cost estimated by the model. It impressively shows that the prediction quality of the applied cost model is indeed very good, especially if ones takes into account the costs per batch can differ by several orders of magnitude. The data presented is taken from the benchmark run, where the parameters have been fitted to. The total number of data points that have been used for fitting amounts to more than 150'000 batches of four center integrals.

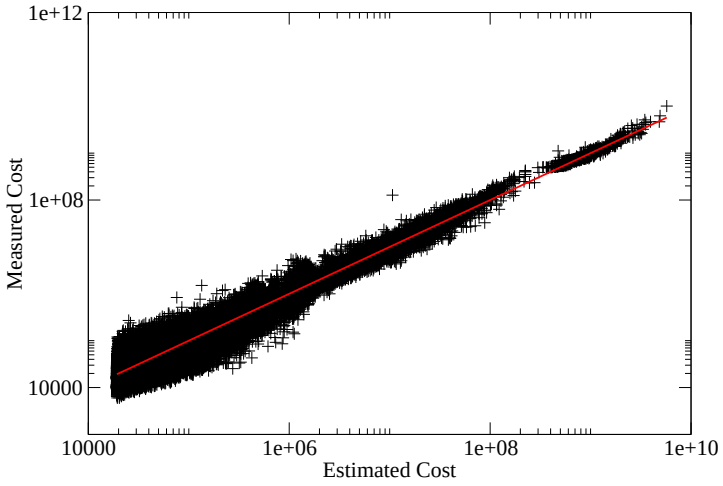

Figure 3.2: Shown is a correlation plot between estimated cost and measured cost for the benchmark system consisting of more than 150'000 subsets. It shows the impressive prediction quality of the cost model spanning several order of magnitudes.

3.5.3 Load balancing

Grouping all the batches into bins is the second important ingredient towards a well load-balanced distribution of work. As mentioned in Sec. 3.5.1 it is important to have dynamically adjusted bin sizes. Thus, in a first step the ranges $\mu_{\text{end}} - \mu_{\text{start}}$ need to be optimized. (For symmetry reasons, it is not necessary to have different ranges for the summations over ν, λ, σ.) This is done in an atom blocking fashioned way, i.e. the smallest amount of work a single bin can contain is given by all basis functions that belong to a certain atom. As an initial guess, this partitioning is assumed to be equidistant pre-

Set	Parameter	Energy	Force
P_1	p_1	$2.94614 \cdot 10^0$	$2.57462 \cdot 10^0$
	p_2	$1.06247 \cdot 10^0$	$1.34205 \cdot 10^0$
	p_3	$-1.91570 \cdot 10^{-2}$	$-9.41673 \cdot 10^{-2}$
	p_4	$1.66685 \cdot 10^0$	$0.94568 \cdot 10^0$
	p_5	$1.75126 \cdot 10^0$	$-1.45118 \cdot 10^0$
	p_6	$-9.76074 \cdot 10^{-2}$	$0.59178 \cdot 10^0$
	p_7	$2.62308 \cdot 10^0$	$2.72911 \cdot 10^0$
	p_8	$-0.31870 \cdot 10^0$	$-0.50555 \cdot 10^0$
	p_9	$7.95882 \cdot 10^0$	$8.35081 \cdot 10^0$
	p_{10}	$1.83314 \cdot 10^0$	$1.68299 \cdot 10^0$
	p_{11}	$0.15427 \cdot 10^0$	$-0.74895 \cdot 10^0$
	p_{12}	$0.19749 \cdot 10^0$	$0.43801 \cdot 10^0$
P_2	p_1	$2.31046 \cdot 10^0$	$2.63985 \cdot 10^0$
	p_2	$1.87440 \cdot 10^0$	$2.30249 \cdot 10^0$
	p_3	$-9.36564 \cdot 10^{-2}$	$5.33216 \cdot 10^{-3}$
	p_4	$0.64284 \cdot 10^0$	$0.45572 \cdot 10^0$
	p_5	$1.01375 \cdot 10^0$	$1.81197 \cdot 10^0$
	p_6	$-6.80088 \cdot 10^{-3}$	$-0.12533 \cdot 10^0$
	p_7	$1.16926 \cdot 10^0$	$-1.40403 \cdot 10^0$
	p_8	$-2.63147 \cdot 10^0$	$-4.53316 \cdot 10^0$
	p_9	$19.23781 \cdot 10^0$	$12.59343 \cdot 10^0$
	p_{10}	$1.05059 \cdot 10^0$	$1.13119 \cdot 10^0$
	p_{11}	$0.80382 \cdot 10^0$	$1.42459 \cdot 10^0$
	p_{12}	$0.49903 \cdot 10^0$	$1.14253 \cdot 10^0$
P_3	p_1	$7.82336 \cdot 10^{-3}$	$0.12051 \cdot 10^0$
	p_2	$0.38073 \cdot 10^0$	$1.38280 \cdot 10^0$

Table 3.1: Shown are the 26 parameters used in the cost model function f for energy and forces respectively.

defined by a block size N_b. With other words, block 1 contains initially the atoms 1 to N_b, block 2 the atoms $N_b + 1$ to $2N_b$ and block N_{blocks} contains the atoms $N_{\text{atoms}} - N_b$ to N_{natoms}. At the end of this initial blocking, each bin contains N_{blocks}^4 atomic ranged blocks.
In a second step, the cost for each of this blocks is estimated using the cost model from the previous section. For the optimization of the block partitioning it is sufficient to consider diagonal integrals only, because they are usually the most expensive ones. That is, the four fold sum in Eq. 3.7 is evaluated for $\mu = \nu = \lambda = \sigma$. During this optimization process, the width N_b of an atomic block is dynamically adjusted until the variation in cost from the mean is sufficiently small. In practice, the most expensive atomic kinds are typically collected in small blocks whereas less computationally demanding species such as hydrogen atoms belong to larger blocks. As shown in Fig. 3.3 dynamically sized atomic blocks reduce the outliers dramatically which is very important for obtaining good scalability.

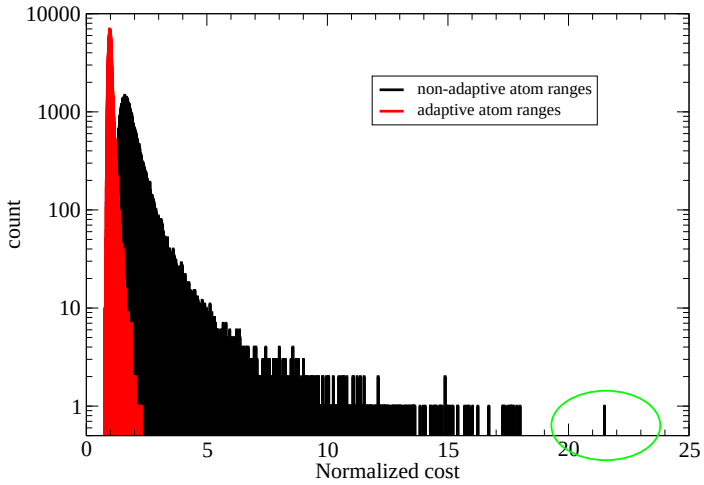

Figure 3.3: Shown are normalized bin costs as obtained from the benchmark system for the case of non-adaptive atom ranges and adaptive atom ranges. The adaptive scheme is far superior from the non-adaptive one with respect to the spread of the cost. Furthermore, as indicated by the green circle, non-adaptive atom ranges may lead to large outliers which would prevent the algorithm from scaling since this bin cannot be distributed further.

At that stage, the actual load balance procedure can start. Each involved process is provided with roughly the same portion of the in total $N_{\text{blocks,opt}}^4$

atomic blocks, estimates the associated cost based on the cost model and divides this work into bins of roughly equivalent cost. In this way, each process creates a vector of typically 64 bins that contains information about the starting and ending indices as well as the estimated cost. Once provided with this cost vector, the actual distribution of work is straightforward: Firstly, all processes communicate their cost vector and all bins are sorted with respect to its cost. Secondly, all these bins are distributed in a Round-Robin fashioned procedure, i.e. process 1 gets the most expensive bin, process 2 the next less expensive one and so on.
Through this procedure, each process gets a well defined task list consisting of several bins that needs to be processed in order to construct a local Fock matrix. At the end, all processes exchange this local Fock matrix and a single global one is constructed.

3.5.4 Data handling and hybrid `MPI/openMP` programming model

Each integral $(\mu\nu|\lambda\sigma)_g$ has by definition an eight-fold permutational symmetry

$$(\mu\nu|\lambda\sigma)_g = (\nu\mu|\lambda\sigma)_g = (\lambda\sigma|\mu\nu)_g = \cdots . \tag{3.16}$$

This symmetry is respected in the current implementation and hence results in a speed-up of factor 4 and a memory reduction of the same size. In practice, that means that every integral needs to be contracted with four different density matrix elements, which thus need to be present on the corresponding process. Since it is far from being easy to perform the load balance under the constraint that each process gets a minimal number of matrix elements it has been decided to replicate the full density matrix on each compute core. The same observation is valid for the Fock matrix and therefore a respectable amount of memory needs to be dedicated to this two matrices which unfortunately reduces the space available for integral storage.
This is the reason why a hybrid `MPI/openMP` programming model has been used for the parallelization. The Fock and density matrices are only replicated once on each node and the dedicated master process forks as many `openMP` threads as there are compute cores. These subprocesses then concurrently access both data structures. Of course, the Fock matrix needs to be updated in a synchronized way such that it is granted that only one process at a time can write into that buffer. However, the `openMP` standard provides highly efficient intrinsics that take care of this synchronization and the loss in performance is small. Due to the fact that both matrices can become rather big ($\mathcal{O}(N^2)$ floating point numbers) prefetching strategies are necessary in

order to reduce cache miss cycles. This is achieved by collecting all matrix elements that will be used for processing the current bin into a local buffer that usually fits into the high level caches of the CPU.
The shared memory approach has an additional advantage. The involved threads can create a master task list containing all task lists from the processes obtained from the load balance procedure. Even though these task lists are very well load balanced, typically to within less than 5% overhead, an additional fine grained load balance can be achieved by distributing the bins in the master task list in a first-come-first-serve fashion among the child processes.
The main advantage of this approach is the easy communication pattern. At the beginning of the calculation, the density matrix needs to be replicated and at the end the local Fock matrices need to be summed and redistributed. However, for larger systems, this communication can easily become the bottleneck and prevent the algorithm from scaling further.
Depending on system size, the current algorithm scales almost perfectly up to ten thousands of cores and has proven to be very efficient. Benchmarks and scaling plots can be found in the second part of this thesis.

3.6 Scaling with respect to basis set quality

So far, only scaling with respect to system size N has been discussed. The picture completely changes when one considers scaling with respect to basis set quality. The problem is, that algorithms that rely on screening techniques based on a threshold break down, when higher quality basis sets are applied. This has to do with the fact that the screening thresholds have to be chosen much tighter in order to retain stability throughout the wavefunction optimization. Furthermore, the number of higher angular momentum basis functions (i.e. polarization functions) scales quadratically with quantum number l which again increases the computational workload. Since higher quality basis set typically contain more diffuse Gaussian primitives, this leads to extended spatial overlap in the wavefunctions which has disadvantageous impact on the screening efficiency. As a consequence, the construction of the Fock-matrix still scales linearly with system size but at significantly increased computational cost.
Introducing an auxiliary density matrix that replaces the real density matrix in the high quality basis set representation with an approximated one seems to solve this problem. Within this work, several schemes have been elaborated in order to obtain such an approximation. Extensive testing of these auxiliary density matrix methods (ADMM) reveal that without significant

loss of accuracy, the efficiency of the of the screening based HFX algorithm can be retained.
Chapter 7 discusses and illustrates ADMM in detail.

Part II

Validation, Benchmarks and Applications

Chapter 4

Ab initio MD using hybrid density functionals [35]

Ab initio molecular dynamics simulations with hybrid density functionals have so far found little application due to their computational cost. In this work, an implementation of Hartree-Fock exchange is presented that is specifically targeted at ab initio molecular dynamics simulations of medium sized systems. We demonstrate that our implementation, which is available as part of the `CP2K/Quickstep` program, is robust and efficient. Several prescreening techniques lead to a linear scaling cost for integral evaluation and storage. Integral compression techniques allow for in-core calculations on systems containing several thousands of basis functions. The massively parallel implementation respects integral symmetry and scales up to hundreds of CPUs using a dynamic load balancing scheme. A time-reversible multiple time step scheme, exploiting the difference in computational efficiency between hybrid and local functionals, brings further time savings. With extensive simulations of liquid water, we demonstrate the ability to perform, for several tens of picoseconds, ab initio molecular dynamics based on hybrid functionals of systems in the condensed phase containing a few thousand Gaussian basis functions.

4.1 Introduction

Density functional theory (DFT) has become an established method for computing the electronic structure and properties of molecules, solids and liquids. The success of DFT can be attributed to the quality of the approximate exchange and correlation (XC) functionals that have been developed. Since the introduction of the generalized gradient approximation (GGA), such as

for example Becke's exchange functional [23], DFT provides in many cases a respectable accuracy at a relatively low computational cost. GGAs depend only on the electronic density and gradient, and this dependency is local in space, i.e. the XC potential in a given point can be obtained directly from the electron density and its gradients in that point. The low computational cost of DFT can to a large extend be attributed to the local nature of the XC functionals. Nowadays it is possible to compute the electronic structure of systems containing thousands of atoms and to perform ab initio molecular dynamics (MD) simulations of systems containing hundreds of atoms for tens of picoseconds. Several simulation packages are available that focus on DFT in the GGA approximation, and that specifically target large systems and/or molecular dynamics simulations. Most linear scaling DFT implementations and plane wave based approaches fall in this category. In this work, we will focus on one such code, namely `CP2K/Quickstep` [36, 14]. `CP2K` is a freely available implementation of the Gaussian and plane waves (GPW) method [13] that is specifically designed to deal accurately and efficiently with systems containing a few thousand atoms and is able to perform high quality molecular dynamics simulations in gas and condensed phases. The GPW method employs a dual representation of the electron density, in Gaussians and plane waves, to compute all terms of the Kohn-Sham equations, and in particular the Hartree energy and potential, in linear scaling time.

A significant fraction of the XC functionals that have been developed in the last twenty years are non-local in nature. The non-locality results from Hartree-Fock exchange (HFX) terms that are part of these functionals. Since these functionals do not only depend on the electronic density, but also on the Kohn-Sham orbitals (in a non-local way), these are considered 'hybrid' functionals, as opposed to the 'pure' or (semi-)local functionals that only depend on the density and its gradients. Such hybrid functionals are almost always more accurate than their pure counterparts, and are therefore commonly employed for typical quantum chemical calculations on (small) molecules. Furthermore, it is now generally accepted that non-locality is key to address some of the more embarrassing failures of GGAs, in particular those related to the self-interaction error. New developments (see e.g. Ref. [37]) suggest that significant progress has been made in this area. We can safely conclude that hybrid functionals are here to stay. However, the computational cost of non-local functionals is, almost unavoidably, larger than that of local functionals. Despite the fact that also hybrid functionals have been implemented in a linear scaling fashion, the pre-factor is normally significantly larger for hybrid than for local functionals. However, the increase in computational cost is not prohibitive, depending on implementation details, basis set and system, a hybrid is typically less than 100 times more expensive than a lo-

cal functional. Nevertheless, the significant computational cost is the main reason why hybrid functionals have so far found little application for extensive ab initio MD simulations. In this work, we seek to close this gap, and report on our implementation of HFX that is specifically targeted at MD simulations of gas and condensed phase systems.

Ab initio molecular dynamics simulations are only practical if a full electronic optimization, including the calculation of the forces, takes less than a couple of minutes, ideally a couple of seconds. We therefore focus on medium sized systems, typically up to 5000 basis functions or a few hundred atoms, and a massively parallel implementation. In the following sections, we will discuss how this choice allows us to make certain design decisions, for example for the in-core and parallelization schemes, that yield a highly efficient implementation. As many interesting chemical systems are in condensed phases or on surfaces, periodic boundary conditions, in addition to cluster (free) boundary conditions, have been implemented. Clearly, the implementation must be accurate and robust, since noise, inconsistencies or instabilities could quickly invalidate the MD procedure, which requires thousands of successive electronic structure calculations. The outline of this paper is as follows: Basic HFX theory is reviewed in Sec. 4.2, in Sec. 4.3 all techniques that we have incorporated in our implementation are discussed in detail, in Sec. 4.4 benchmark results demonstrating the applicability of the tool are presented, in Sec. 4.5 we study radical cations dimers with some recent functionals, and in Sec. 4.6 we present extensive molecular dynamics simulations of liquid water based on hybrid functionals.

4.2 Theory

Hybrid functionals have in common that they incorporate a certain amount of Hartree-Fock exchange (HFX) with a generalized interaction potential $g(r)$:

$$E_x^{HF} = -\frac{1}{2}\sum_{k,l}\int d\mathbf{r}_1 d\mathbf{r}_2 \psi_k^*(\mathbf{r}_1)\psi_l^*(\mathbf{r}_2)g(r_{12})\psi_k(\mathbf{r}_2)\psi_l(\mathbf{r}_1) \tag{4.1}$$

In an atomic orbital basis this is conveniently expressed as

$$E_x^{HF} = -\frac{1}{2}\sum_{\mu\nu\lambda\sigma} P_{\mu\lambda}P_{\nu\sigma}\left(\mu\nu|\lambda\sigma\right)_g, \tag{4.2}$$

where $P_{\mu\lambda}$ denotes the density-matrix element corresponding to an atomic orbital basis and

$$\left(\mu\nu|\lambda\sigma\right)_g = \int d\mathbf{r}_1 d\mathbf{r}_2 \mu(\mathbf{r}_1)\nu(\mathbf{r}_1)g(r_{12})\lambda(\mathbf{r}_2)\sigma(\mathbf{r}_2), \tag{4.3}$$

are the four-center electron repulsion integrals (ERIs) arising from an interaction potential $g(r)$. Plane wave based approaches will naturally base their implementation on the first expression Eq. 4.1 while Gaussian based codes typically start from the second expression Eq. 4.2. HFX calculations in `CP2K` are based on Eq. 4.2.

The interaction potential $g(r)$ takes different forms for different hybrid functionals. The most common choice is the standard Coulomb potential

$$g(r) = \frac{1}{r} \tag{4.4}$$

and this form is employed in well established hybrid functionals such as B3LYP [38, 24, 27] or PBE0 [28, 29, 30]. Currently, there is great interest in functionals that split the Coulomb operator in a short and a long-range part

$$\frac{1}{r} = \frac{\mathrm{erfc}(\omega r)}{r} + \frac{\mathrm{erf}(\omega r)}{r} \tag{4.5}$$

There is no fundamental reason to prefer the error function in the above equation, but it is a convenient choice, which allows for tuning the range of the respective parts with the parameter ω. Depending on the purpose of the XC functional, short and long-range parts might be omitted, or added with different weights. For the condensed phase, early work on HFX [39] as well as more recent functionals such as HSE06 [31, 40] retain only the short-range Coulomb potential. More general functional forms such as a linear combination of long-range Coulomb and Gaussian-type interactions

$$g(r) = \alpha \frac{\mathrm{erf}(\omega r)}{r} + \beta \exp\left(-\omega^2 r^2\right), \tag{4.6}$$

have been employed as well, for example in MCY3 [41]. All the above integrals can be evaluated analytically when Cartesian Gaussian-type orbitals are employed

$$\phi(\mathbf{r} - \mathbf{A}) = \sum_i c_i (x - A_x)^l (y - A_y)^m (z - A_z)^n \exp\left(-\alpha_i (\mathbf{r} - \mathbf{A})^2\right), \tag{4.7}$$

in which $\mathbf{A} = (A_x, A_y, A_z)$ refers to the orbital center, α_i to the exponent, c_i to the contraction coefficient and l, m, n to the angular momenta.

The computational cost of HFX increases with the size of the system and/or the basis employed. A brute force implementation of Eq. 4.2 would require $\mathcal{O}(N^4)$ operations, where N is the number of basis functions. Actual implementations employ the Schwarz inequality:

$$\left| \left(\mu\nu|\lambda\sigma\right)_g \right| \leq \left[\left(\mu\nu|\mu\nu\right)_g\right]^{\frac{1}{2}} \left[\left(\lambda\sigma|\lambda\sigma\right)_g\right]^{\frac{1}{2}}, \tag{4.8}$$

to obtain an upper bound for the ERIs. With this upper bound, which is non-negligible only if μ is close to ν and λ close to σ, a large number of tiny contributions to the energy can be ignored, so that the cost of HFX reduces to $\mathcal{O}(N^2)$ with increasing system size. [42] Linear scaling, i.e. $\mathcal{O}(N)$, calculation of the HFX energy can be obtained by exploiting the fact that individual terms in Eq. 4.2 become smaller as the distance between the atomic centers of μ and λ or ν and σ increases. There are two possible reasons for this decrease. Firstly, for some choices of the operator $g(r)$, for example the short-range Coulomb operator in Eq. 4.5, the matrix elements $(\mu\nu|\lambda\sigma)_g$ decay rapidly. Secondly, the density matrix elements $P_{\mu\lambda}$ become smaller as the distance increases [43, 44]. These features can be employed to obtain improved efficiency and ultimately linear scaling HFX algorithms. [45, 46, 47, 48] It is important to point out that the reduction from $\mathcal{O}(N^4)$ to $\mathcal{O}(N)$ with increasing system size does not hold for increasing the basis set size at fixed system size. In the latter case, for a typical atomic orbital implementation, the scaling remains $\mathcal{O}(N^4)$.

4.3 Methods

In this section, we will describe all the techniques we have employed to compute the HFX as given by Eq. 4.2 as efficiently as possible, while retaining accuracy and stability. For many techniques, very similar methods have been reported in literature before. Nevertheless, we believe that the combination employed in this implementation is unique, and allows us to perform ab initio molecular dynamics based on hybrid density functionals for a range of system size and timescale that has not yet been explored. In practice, we obtain, for systems with a gap, a linear scaling construction of the Fock matrix based on a screening of the integrals, taking into account the density matrix elements. Furthermore, a significant time saving is obtained by performing in core calculations, i.e. by storing ERIs into main memory (RAM) at the first step of the self-consistent (SCF) procedure, and reusing these integrals at successive steps. Using ERI compression algorithms and exploring parallelism, we show that this is feasible even for systems containing thousands of basis functions and hundreds of atoms. Parallelism is of central importance, and during MD simulations, we employ timings obtained at previous MD steps to dynamically load balance the calculation. Finally, we exploit the large difference in computational cost between GGA and hybrid calculations by performing multiple time step MD, which requires hybrid calculations only every Nth time step, where N can be 5 or more, depending on the system.

4.3.1 Calculation of the ERIs

For the calculation of the ERIs and their analytic derivatives with respect to the corresponding atomic centers, we rely on the external library `LIBINT` [34]. This library encapsulates an implementation of the recursive Obara-Saika (OS) method [33] and Head-Gordon and Pople's [49] variation thereof. The advantage of this recursive approach is the simple way the algorithm can be enhanced to handle various interaction potentials. [50] Indeed, the OS scheme only needs the $(ss|ss)_g$ integral, i.e. the lowest angular momentum interaction, as a starting point for the recursion, and can thus be straightforwardly extended to $g(r)$'s other than the usual $1/r$. This makes our implementation flexible enough to include all kind of hybrid functionals mentioned in the introduction.

In order to speed up the calculation, and to reduce the total amount of memory needed for integral storage, we take the full permutational symmetry of the ERIs into account, i.e.

$$\begin{aligned}(\mu\nu|\lambda\sigma)_g &= (\nu\mu|\lambda\sigma)_g = (\nu\mu|\sigma\lambda)_g = (\mu\nu|\sigma\lambda)_g \\ &= (\lambda\sigma|\mu\nu)_g = (\lambda\sigma|\nu\mu)_g = (\sigma\lambda|\nu\mu)_g = (\sigma\lambda|\mu\nu)_g. \end{aligned} \quad (4.9)$$

While this symmetry is commonly employed in serial codes, we also use this symmetry in the parallel version of the algorithm. In this way, we save a factor of approximately 8 in the number of integrals that have to be considered.

4.3.2 Integral screening

Screening methods improve the efficiency of the Fock-matrix construction by providing an easily computable upper bound for the value of an ERI or a set of ERIs. In this way, one can avoid calculating interactions whose contributions are smaller than a given threshold ϵ. One well-known upper bound is the already introduced Schwarz inequality Eq. 4.8. In our scheme, before starting the calculation of the ERIs we precompute all the two-index quantities $(\mu\nu|\mu\nu)_g$ and utilize the maximum value in a given set as an estimate for its contribution to the Fock-matrix. This screening reduces the total number of ERIs to be considered from $\mathcal{O}(N^4)$ to $\mathcal{O}(N^2)$. [42] The Schwarz procedure takes advantage of the exponential decay of the charge distributions $\mu\nu$ with respect to the distance between the Gaussian centers μ and ν.

If a rapidly decaying interaction potential such as the short-range potential $\mathrm{erfc}(\omega r)/r$ is employed, also the distance of two Gaussian product distributions $\mu\nu$ and $\lambda\sigma$ decay rapidly with respect to the distance between their centers. Following the approach proposed by Izmaylov et al. [51], we

therefore introduce a far-field box screening, which yields significant savings in computational cost if short-range exchange is used in large systems. This technique groups charge distributions in real space boxes for the purpose of screening and is based on the following integral-estimate:

$$\left\{(\mu\nu|\frac{\mathrm{erfc}(\omega r_{12})}{r_{12}}|\lambda\sigma), \mu\nu \in B_i, \lambda\sigma \in B_j\right\} \lesssim \frac{\mathrm{erfc}(\theta_{B_iB_j}R_{B_iB_j})}{R_{B_iB_j}} K_{B_i}K_{B_j}. \tag{4.10}$$

Here, B_i and B_j denote boxes in real space to which pairs of charge distributions $\mu\nu$ are assigned. To perform the screening, the following descriptors are required:

$$K_{B_i} = \max_{\mu\nu\in B_i} K_{\mu\nu} = \max_{\mu\nu\in B_i} \frac{\sqrt{2}\pi^{5/4}}{\alpha+\beta} \exp\left[-\frac{\alpha\beta}{\alpha+\beta}(\mathbf{A}-\mathbf{B})^2\right], \tag{4.11}$$

$$R_{B_i} = \max_{\mu\nu\in B_i} R(\Omega_{\mu\nu}, B_i), \tag{4.12}$$

$$\alpha_{B_i} = \min_{\mu\nu\in B_i} \alpha_{\mu\nu} = \min_{\mu\nu\in B_i} \frac{\alpha\beta}{\alpha+\beta}, \tag{4.13}$$

$$\theta_{B_iB_j} = \left(\frac{1}{\alpha_{B_i}} + \frac{1}{\alpha_{B_j}} + \frac{1}{\omega^2}\right)^{-1}, \tag{4.14}$$

$$R_{B_iB_j} = R(B_i, B_j) - R_{B_i} - R_{B_j} \tag{4.15}$$

where $R(\Omega_{\mu\nu}, B_i)$ is the distance between the centers of Box B_i and the charge distribution $\mu\nu = \Omega_{\mu\nu}$, R_{B_i} is the box range, $\alpha_{\mu\nu}$ is the exponent of the charge distribution, and $\Omega_{\mu\nu}$ and $R(B_i, B_j)$ is the distance between the centers of the boxes.

However, the right-hand side in the above estimate is not a strict upper bound, but only valid in the far field. In numerical tests we observed that the largest error in total energy due to this distance screening never exceeded the applied threshold by more than two orders of magnitude. Therefore, in order to achieve consistently accurate results, two thresholds $\epsilon_{Schwarz}$ and ϵ_{Box} have been introduced, and the latter is normally set 10 to 100 times smaller than the first.

4.3.3 Density matrix screening

As mentioned previously, it is possible to exploit the decay of the density matrix and screen on density matrix elements $P_{\mu\nu}$. Indeed, it can be shown [43, 44] that the density matrix of insulators decays exponentially as

$$\lim_{|\mathbf{r}_1-\mathbf{r}_2|\to\infty} \rho(\mathbf{r}_1, \mathbf{r}_2) \sim \exp\left(-\sqrt{E_{gap}}|\mathbf{r}_1 - \mathbf{r}_2|\right), \tag{4.16}$$

where E_{gap} is the energy difference between the highest occupied (HOMO) and the lowest unoccupied (LUMO) molecular orbital. For metallic systems, the decay is algebraic at zero temperature, and only becomes exponential at a finite electronic temperature. [44] The basic modification to obtain a more efficient, and even linear scaling HFX calculation is to introduce the density matrix elements in the Schwarz screening procedure as

$$P_{max} \times |(\mu\nu|\mu\nu)_g|^{1/2} |(\lambda\sigma|\lambda\sigma)_g|^{1/2} \leq \epsilon_{Schwarz}, \tag{4.17}$$

where P_{max} is given by

$$P_{max} = \max \{|P_{\mu\lambda}|, |P_{\mu\sigma}|, |P_{\nu\lambda}|, |P_{\nu\sigma}|\} . \tag{4.18}$$

Note that several density matrix elements are required for P_{max}, which is related to the fact that ERI symmetry is exploited in the implementation.

Screening on the density matrix is slightly tricky during the SCF procedure, because the density matrix is not yet known, or at least, only partially converged. Commonly, the density matrix from the previous SCF iteration is used for the screening in the next iteration, and this procedure is typically stable. [45] However, we prefer, for two reasons, a procedure in which the density matrix used for screening is fixed at the first SCF iteration. Firstly, this simplifies an in-core scheme, because for each SCF iteration, exactly the same set of integrals is needed, in the same order. There is thus no need to store the indices of the quartets, and ERIs can be accessed in a first-in-first-out (FIFO) manner. A second reason is that this makes the wavefunction optimization more robust, in particular for direct minimization methods, such as the orbital transformation (OT) method. [52] These methods perform best if the the Fock matrix is the exact derivative of the HFX energy, and if the HFX energy functional is invariant throughout the minimization procedure, i.e. if exactly the same terms are retained in Eq. 4.2 at all steps. This allows for minimizing the functional to machine precision, despite the fact that the functional itself is defined by a tolerance ($\epsilon_{Schwarz}$) that can be much larger than machine precision. This is important for robust and accurate molecular dynamics simulations.

We have two recipes to obtain a density matrix for screening. A first choice is to employ a density matrix that is obtained from a converged GGA calculation. As we will show in the following section, GGA calculations are typically much faster than hybrid calculations, so this is a very effective strategy. This is also a rather reliable estimate of the density matrix, indeed, it is well known that non-self-consistent 'post-GGA' calculations already provide relatively accurate total energies for hybrid functionals, and such a 'post-GGA' strategy is often employed in functional development. Nevertheless,

we would like to point out that using a GGA density matrix is likely to be a conservative choice for screening. Indeed, Eq. 4.16 shows that the decay of the density matrix is proportional to the electronic gap. Since it is well known that GGAs tend to underestimate the gap, we can infer that GGA density matrices decay slower than the corresponding hybrid ones, and hence are a conservative choice for the screening procedure. A second, and even more accurate scheme is available only during MD simulations. During an ab initio molecular dynamics simulation in `CP2K`, an initial density matrix is obtained from an extrapolation of the density matrix of previous time steps [52]. We find that the density matrix generated in such a way is very accurate, typically the total energy at the first SCF step is within a few micro-Hartrees of the converged result. As this is more accurate than a density matrix from a GGA calculation, we prefer this option during MD.

4.3.4 ERI compression

As mentioned previously, in-core calculations are significantly faster than 'direct' calculations (which recompute integrals at every SCF step). Of course, the available main memory (RAM) is potentially a limiting factor. However, in a massively parallel environment, it is not uncommon to have several hundreds of Gigabytes of RAM available, so that this is less of an issue than a couple of years ago. Nevertheless, RAM remains a valuable resource. In order to treat really large systems, and to gain efficiency on systems with limited RAM, we have implemented an in-core compression scheme. In this scheme ERIs are stored with just enough bits, as required by the screening tolerance. Similar techniques have previously been implemented for approaches based on disk storage [53, 54]. We find that an in-core compression scheme can be implemented very efficiently, i.e. without significant slow-down of the in-core SCF steps, and that it allows for a five- to tenfold increase in the number of ERIs stored in-core. This is a very significant saving, and we expect this method to find application in other codes and approaches where in-core performance is beneficial.

All integrals that pass the screening procedures mentioned above must be compressed during the first SCF step, and decompressed at all steps. Integrals are compressed one set at the time. For a given set of integrals we compute the corresponding maximum absolute value b_{max} and the maximum corresponding contraction coefficient c_{max} and store this in a persistent array for future use. If the condition

$$P_{max} \times b_{max} \times c_{max} \geq \epsilon_{Schwarz} \tag{4.19}$$

holds, we have to compress the corresponding integrals, otherwise there is

even no need to contract that set. If the set has to be compressed, $P_{max} \times b_{max} \times c_{max}$ is compared with the given threshold ϵ that defines the required accuracy of the compression. In particular, the number of bits required to store these integrals is given by

$$N_{bits} = \text{EXPONENT}\left(\frac{P_{max} \times b_{max} \times c_{max}}{\epsilon}\right) + 1, \tag{4.20}$$

where EXPONENT(x) returns the exponent of x in the base 2. The compression algorithm then proceeds in three steps:

- Convert the double precision values (r) of the integrals in the current batch to integer values (i) so that $\tilde{r} = \text{ANINT}(r/\epsilon) \times \epsilon$ becomes a properly rounded approximation to r. In particular, it holds that $|r - \tilde{r}| \leq \epsilon/2$, since the rounding error of the intrinsic integer-truncation routine ANINT(x) is $\pm 1/2$.

- Store the integer values to an array that has the function of a cache. For each value of N_{bits} there is a different cache.

- As soon as a cache is full, flush the cache to a storage-container in an actual compression step. In doing so, all integers are converted to a stream of bits by truncating these integers to the significant number of bits, and 'pasting' these bits in a contiguous stream.

In the above procedure, the intermediate cache is introduced for efficiency reasons. When operating on a cache of sufficient size (e.g. 1000 to 4000 values), the actual compression is approximately as fast a just copying the data. Decompression proceeds similarly. For each set, retrieve b_{max} and determine if integrals are needed and what the required precision is. Obtain these integrals from an integer cache, which is refilled by decompressing a bit stream as needed.

Three further details are important as well. Firstly, even at the first SCF iteration, the decompressed integrals are employed for the assembly of the Fock matrix. This guarantees consistency throughout the SCF procedure. Secondly, an additional memory reduction is obtained by compressing the exponents of the b_{max} values with a fixed bit-number. Finally, via an input parameter, the user can define the maximal amount of memory that should be reserved for the storage of ERIs. If this limit is reached, all integrals are recomputed every step using a direct approach. Of course, this event coincides with a massive slow down of the method.

4.3.5 Calculation of HFX forces

The calculation of the ionic forces resulting from the HFX terms is relatively straightforward. As mentioned previously, derivatives of the ERIs are directly obtained from `LIBINT`, and there is no reason to store or compress these integrals. We employ the same screening matrices for the near- and far-field estimates as in the construction of the Fock-matrix, but screen differently on the density matrix. In particular, we employ the converged density matrix for the screening. Furthermore, because the contributions of the density-matrix elements enter quadratically into the HFX forces, the Schwarz criterion can be adapted to

$$2 \times \max\left\{|P_{\mu\lambda}| \times |P_{\nu\sigma}|, |P_{\mu\lambda}| \times |P_{\nu\sigma}|\right\} \times |(\mu\nu|\mu\nu)_g|^{1/2} |(\lambda\sigma|\lambda\sigma)_g|^{1/2} \leq \epsilon_{Schwarz}. \tag{4.21}$$

As a result of this improved screening, the calculation of the forces is computationally less expensive than the first SCF step, despite the fact that higher order angular momentum ERIs are needed.

4.3.6 Periodic boundary conditions

The proper implementation of HFX in periodic boundary conditions (PBC) is non-trivial. An interaction energy in PBC is given by an infinite sum over image cells. It is well known that the electrostatic energy of a periodic system is the result of a conditionally convergent sum. The value thus depends on the exact order that is employed to perform this sum, and on the boundary conditions that are employed. [55] The same holds for standard HFX, which is Coulombic in nature. [56, 16, 57] As soon as the interaction potential decays rapidly enough, the sum is unconditionally convergent, and these issues are absent. This is one reason why screened exchange was introduced in early implementations of periodic exact exchange [39, 58] and recent hybrid functionals for the condensed phase. [31]

We have decided to base our periodic implementation on a scheme recently proposed by Tymczak et al. [59] In this scheme, PBC are obtained by applying the minimum image convention (MIC) at the level of primitives in a Γ-point approximation. In this context the periodic Fock-matrix reads as follows:

$$H_{\mu\nu}^{HFX} = -\frac{1}{2} \sum_{\mathbf{MN},\mu\lambda} P_{\mu\lambda} \left(\mu\nu^{\mathbf{M}}|\lambda\sigma^{\mathbf{N}}\right)_g, \tag{4.22}$$

where $\mathbf{M}$ and $\mathbf{N}$ denote the summation over lattice vectors. In practice, for fairly large unit cells it is sufficient to retain the largest integral in the sum. The latter we obtain by applying the MIC to the interaction vector

PQ, where **P** and **Q** are defined as the centers of the product distributions $\mu\nu$ and $\lambda\sigma$ respectively, for that choice of **M** and **N** that yield maximum overlap of $\mu\nu^{\mathbf{M}}$ and $\lambda\sigma^{\mathbf{N}}$. The advantage of the MIC scheme is its simplicity. Furthermore, in case the unit cell is sufficiently large, it is basically exact for short-range operators such as screened exchange. However, if unit cells are smaller, or if unscreened exchange is being employed, the MIC scheme is an approximation. In Ref. [59] it is shown that this approximation can be very good, converging exponentially to an asymptotic value with respect to the size of the unit cell, even if unscreened exchange is employed. Unfortunately, we find that the MIC can be an unstable approximation if the range of the operator is not sufficiently small. This instability introduces a spurious minimum in the energy functional, which yields an unphysical wavefunction, with an energy that can be several Hartrees beyond the stable solution. Whether or not this minimum is present appears to depend on the atomic configuration, and on the basis set. The more flexible the basis set, the more likely it appears to minimize towards this unphysical solution. In the condensed phase and for applications such as MD, where a wide range of configurations is explored, and stability is important, we have to recommend the use of screened exchange in combination with the MIC.

4.3.7 Parallelization strategy

The parallelization of `CP2K` is mainly based on the message passing interface (`MPI`), but also a hybrid mode based on `MPI/openMP` is possible. A central choice in our HFX parallelization strategy is that we replicate the density and Fock matrix on each `MPI` process. This scheme has a trivial communication pattern. It involves no other significant communication than replicating the density matrix before the Fock assembly, and distributing the Fock matrix after assembly. A significant advantage is that one can easily make use of the full ERI symmetry, saving typically a factor of four over codes that ignore the symmetry. Furthermore, since any element of the Fock matrix can be computed by any process, it simplifies the load balancing procedure. The downside of this approach is that it limits both system size and ultimately parallel scalability. The limit in system size arises from the RAM required to store the matrices on each process. For example, with 1Gb per process, 4000 basis functions is approximately the limit. This roughly coincides with the expected typical size of the systems for which hybrid MD will be performed. On multi-core or shared memory systems, it can be beneficial to use the hybrid `MPI/openMP` implementation. In this implementation, only one `MPI` process is needed per node, while a variable number of threads can be employed. The threads share the matrices, so that the full memory of the

node can be employed for a single copy of these matrices. Nowadays, it is common to have 4–64 Gb of memory per node, thus allowing for significantly larger systems. The replication of the density matrix, and the distribution of the Fock matrix is an operation with a cost that does not scale with the number of processes. We find that this step ultimately limits the parallel scalability of our approach.

What remains to be specified is how we distribute the workload among the processes. For this, we have developed a load balance optimization based on simulated annealing, and a binning procedure to coarse grain the load balancing problem. Once the screening matrices have been computed, bins are created that group the successive sets of ERIs that pass the screening procedure. Such a bin just records the starting and ending indices of the four-center loop, and approximately 10 to 100 bins are created per CPU. Each bin is constructed such that the corresponding integrals will approximately require the same amount of memory. The above steps are executed fully in parallel, based on a distribution of the two outer most loop indices. To make the load balance of this step insensitive to the order of the atoms, we first convert these two loop indices into a hash value before modulo distributing it. Subsequently, all bins are redistributed to improve the load balance. This redistribution is based on an estimated cost of each bin, and a simulated annealing procedure to minimize the maximum estimated cost over all processes. The simulated annealing procedure is based on Monte Carlo (MC), in which bins can be swapped between two processors or moved from one processor to another. After a few MC steps, in which the temperature is gradually reduced, we end up with a quasi optimal distribution of the bins, according to which we schedule now the workload on each CPU.

Since the MC procedure schedules the bins quasi optimally, the remaining load-imbalance should be attributed to the inaccuracy of modeling the cost of each bin. Initially, the cost of a bin is estimated from the number of integrals that pass the screening procedure. This is not necessarily optimal, because a given integral might take longer to compute, or might actually be skipped for the in core steps. During MD, a better, dynamic strategy is available. Indeed, we can simply measure the time it takes to process a given bin, and use this as the cost for the load balance procedure in the next MD step. Since bins typically contain thousands of integrals, the measurement is accurate without the need to resort to high resolution timers. As the cost of the bins varies slowly during the MD, this leads to a particularly well load-balanced scheme.

4.3.8 Multiple time step MD

In this section, we describe how the computational cost of a hybrid molecular simulation can be reduced by a multiple time step scheme. In such a scheme, the calculation is split in an inexpensive part and an expensive part that can be evaluated with different frequencies, i.e. with time steps of different length. Using a carefully constructed integration scheme, the time evolution remains reversible, and the molecular dynamics simulation remains accurate and energy conserving. Here, we describe how to use the reversible reference system propagator algorithm (r-RESPA) [60] to achieve this in the context of hybrid molecular dynamics simulations. In our scheme, the difference in computational cost between a hybrid and a local functional is exploited, by performing a hybrid calculation only after several pure DFT calculations. A similar approach, although not within a time reversible framework, has been demonstrated with local functionals [61].

r-RESPA is derived from the Liouville operator representation of Hamilton mechanics

$$iL = \sum_{j=1}^{f} \left[\frac{\partial H}{\partial p_j} \frac{\partial}{\partial x_j} + \frac{\partial H}{\partial x_j} \frac{\partial}{\partial p_j} \right], \tag{4.23}$$

where L denotes the Liouville operator for the system containing f degrees of freedom. This operator is then used to create the classical propagator $U(t)$ for the system:

$$U(t) = e^{iLt}. \tag{4.24}$$

Decomposing the Liouville operator into two parts

$$iL = iL_1 + iL_2, \tag{4.25}$$

and applying a 2nd-order Trotter-decomposition to the corresponding propagator yields

$$e^{i(L_1+L_2)\Delta t} = \left[e^{i(L_1+L_2)\Delta t/n}\right]^n = \left[e^{iL_1(\delta t/2)} e^{iL_2 \delta t} e^{iL_1(\delta t/2)}\right]^n + O(\Delta t^3/n^2), \tag{4.26}$$

with $\delta t = \Delta t/n$. For this propagator several integrator schemes can be derived [62]. The extension for multiple time step (MTS) MD is obtained by a decomposition of the force in the Liouville operator into two or more separate forces

$$iL = \sum_{j=1}^{f} \left[\dot{x}_j \frac{\partial}{\partial x_j} + F_j^1 \frac{\partial}{\partial p_j} + F_j^2 \frac{\partial}{\partial p_j} \right]. \tag{4.27}$$

For that specific case, the propagator reads

$$e^{iL\Delta t} = e^{(\Delta t/2)F^2\frac{\partial}{\partial p}}\left[e^{(\delta t/2)F^1\frac{\partial}{\partial p}}e^{\delta t\dot{x}_j\frac{\partial}{\partial x_j}}e^{(\delta t/2)F^1\frac{\partial}{\partial p}}\right]^n e^{(\Delta t/2)F^2\frac{\partial}{\partial p}}. \qquad (4.28)$$

This allows to treat F^1 and F^2 with different time steps, while the whole propagator still remains time reversible. We will refer to an inner and an outer loop to describe the procedure for F^1 and F^2, respectively.

In our approach, we split the forces in the following way

$$\begin{aligned} F^1 &= F^{local} \\ F^2 &= F^{hybrid} - F^{local} \end{aligned}$$

where F^{hybrid} are the forces as obtained from a hybrid calculation, and F^{local} the forces as obtained from a local functional. It is obvious that the corresponding Liouville operator equals a purely hybrid one. The advantage of this splitting is that the magnitude of F^2 is usually much smaller that of F^1 or F^{hybrid}. To appreciate that, one has to consider how closely geometries and frequencies obtained by a hybrid functional normally match the ones obtained by a local functional, in particular for stiff degrees of freedom. The difference of the corresponding Hessians is therefore small and low-frequent. However, we do not remove analytically the high-frequency part, so the theoretical upper limit for the time step of the outer loop remains half the period of the fastest vibration [63]. What we gain is an increased accuracy and stability for larger time steps in the outer loop integration. Even using an outer loop time step close to the theoretical limit, a stable and accurate MD is obtained. In particular, contrary to the single time step case, there is no shift to higher frequencies as the (outer loop) time step is increased. In Sec. 4.4.5, we will show that at least a five-fold increase in time step is possible for a system as delicate as liquid water.

4.4 Benchmarks and validation

In the following, results are provided that illustrate the performance of the code, and that validate the implemented methods. Of particular interest is the comparison between local and hybrid calculations. Unless mentioned otherwise, all calculations have been performed with the following thresholds: $\epsilon_{Schwarz} = 10^{-6}$, $\epsilon_{Box} = 10^{-7}$ and $\epsilon_{Storage} = 10^{-7}$ HSE calculations are based on the HSE06 functional form [32, 40] for which the screening parameter ω is the same in the Hartree-Fock part and the long range exchange functional. In the earlier HSE03 [31, 32] functional, these two screening parameters are

different. Depending on the application, we vary the parameter ω between 0.11, recommended in Ref. [32], and 0.15, which yields more strongly screened exchange.

4.4.1 Basis sets

In this work, we have emphasized the difference in cost between local and hybrid functionals. Clearly, this difference depends on the implementation and can only be large if the difference between local and non-local functionals is exploited in the particular implementation. Timings as obtained with `CP2K` are shown in Tab. 4.1 for a water cluster containing 32 molecules and several different basis sets.

All-electron calculations are performed with the standard Pople basis sets, while pseudopotential calculations use split valence basis sets [14]. We note that in the GPW scheme, family basis sets are inexpensive, while this is not the case for the hybrid implementation. Furthermore, screening is on a set by set basis. It is therefore necessary that the basis sets have optimized contractions and are properly split in sets, also for the pseudopotential calculations [64, 65, 66].

Particularly striking is the difference in scaling behavior with respect to the basis set quality between the hybrid and the local functional. While the cost appears to scale roughly linearly with the size of the basis for the GGA calculations, the scaling is at least cubic for the hybrid functional. In the limit of very large basis sets, scaling is expected to be quadratic and quartic respectively. Furthermore, the cost of adding diffuse functions is much more pronounced in the hybrid case, e.g. going from 6-311G** to 6-311++G** increases the cost of the first SCF step by 30% and 720% for local and hybrid functionals respectively. However, for small basis sets, the difference between hybrid and local calculations is relatively small. This holds in particular if not only the first SCF step is being considered, but the full SCF run. Indeed, the benefit of the in-core scheme can be appreciated by comparing the cost of the first and second SCF step. We note that there is a small difference for local functionals as well, which is unrelated to the in-core procedure, and results from the OT procedure, in which conjugate gradient and line search steps alternate [14]. For this system and for only moderately contracted basis sets, the in-core steps are faster by approximately a factor of 5–7, but the speedup can exceed a factor of a hundred for heavily contracted basis sets. The in-core scheme can thus close somewhat the large gap in efficiency between local and hybrid functionals.

Basis set		1st SCF iteration		2nd SCF iteration	
	N	local	hybrid	local	hybrid
3-21G*	416	1.32	2.07	0.76	0.77
6-31G*	576	1.54	4.89	0.87	1.00
6-31G**	768	1.80	6.10	0.95	1.16
6-311G**	960	2.03	11.72	1.09	2.09
6-311G(2df,2dp)	1856	3.84	44.68	2.05	6.02
6-31++G**	832	2.04	30.57	1.31	3.89
6-311++G**	1152	2.74	97.02	1.95	13.39
6-311++G(2d,2p)	1504	3.39	144.34	2.34	19.47
DZVP	736	1.78	5.95	0.89	1.22
TZV2P	1280	2.48	18.92	1.04	3.23
QZV2P	1472	2.72	34.99	1.07	5.53
QZV3P	1824	3.36	54.07	1.20	8.41

Table 4.1: Shown are representative timings in seconds for a system containing a gas phase cluster of 32 water molecules. In order to illustrate the effect of the in-core scheme, we provide separate timings for the first and the second SCF step. The density functionals employed are PBE and B3LYP as representative local and hybrid functionals respectively. The first five rows represent traditional Gaussian basis sets for all electron calculations, while the three following rows are augmented versions thereof. The last four rows are split valence basis sets for pseudopotential calculations. In the second column, N refers to the total number of spherical basis functions. All calculations have been performed on 64 cores (32 nodes) of a CRAY XT3.

4.4.2 System size

In Fig. 4.1, we show timings for performing total energy calculations on systems of increasing size. Samples of liquid water, containing 32–256 water molecules, have been described using a 6-31G** basis, the PBE and HSE06($\omega = 0.15$) functionals, and periodic boundary conditions. The data shown is the time for a full SCF, minus the time spent in wavefunction optimization ('diagonalization') routines. Wavefunction optimization scales cubically with the system size, but the pre-factor is such that, for the systems studied here, this time accounts for only a small fraction of the total time. As expected, the remaining cost increases perfectly and nearly linearly

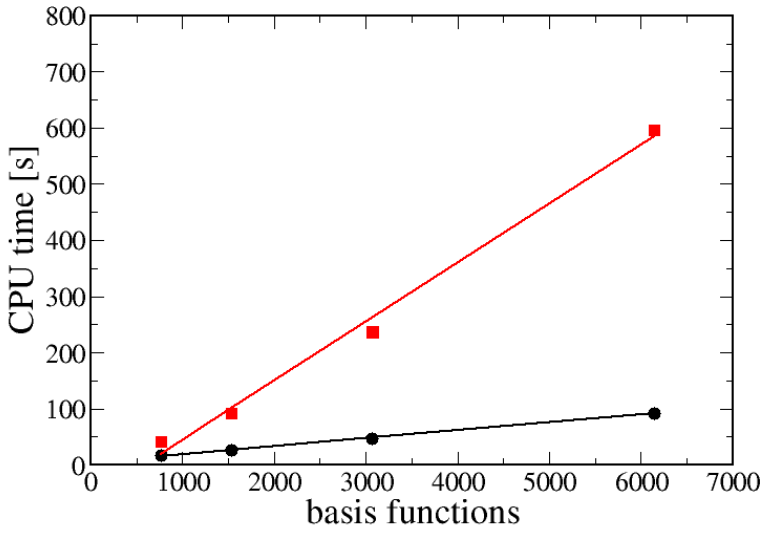

Figure 4.1: Shown is the total elapsed time for a full SCF (typically 10 SCF iterations) minus the time spent in diagonalization routines for liquid samples containing 32, 64, 128 and 256 water molecules and a 6-31G** basis. The plotted quantity is expected to scale linearly with system size. This holds perfectly for the PBE data (lower line, circles), and nearly so for the HSE06 data (upper line, squares). All calculations have been performed on 64 cores (16 nodes) of an Opteron based cluster.

for PBE and HSE06 respectively. The pre-factor for PBE is about 8 times smaller than the pre-factor for HSE06. The small deviation from linearity in the HSE06 case can be attributed to the integral screening, which has not been linearized yet. As shown in Tab. 4.2, the memory used to store the ERIs and the number of computed ERIs scale perfectly linearly with system size.

4.4.3 Parallel efficiency

In Fig. 4.2, the parallel efficiency of the code is illustrated for two systems. The first system is a small water cluster with a small basis set (32 water molecules and 6-31G** basis, 768 basis functions), while the second system is a larger condensed phase system described with a better basis set (64 water molecules and a TZV2P basis, 2560 basis functions). Furthermore,

	$(H_2O)_{32}$	$(H_2O)_{64}$	$(H_2O)_{128}$	$(H_2O)_{256}$
Number of basis functions	768	1536	3072	6144
Number of ERIs [millions]	761	1822	3439	6795
Memory usage for ERIs [MB]	264	536	1062	2130
compression factor	7.92	7.72	7.64	7.66
CPU-time [s]	25	64	174	459

Table 4.2: Shown are timings for the total time spent in Fock-matrix construction (screening, ERI calculation, compression and decompression) throughout a full wavefunction optimization, and the corresponding memory usage for storage of the non-negligible ERIs. The compression factor indicates the efficiency of the compression algorithm. Calculations are based on the HSE06 functional with a 6-31G** basis set, and employ periodic boundary conditions.

for the first system only an energy calculation is performed, while for the second system the time for one MD step (standard Born-Oppenheimer MD, no multiple time step scheme) is measured. The dynamic load balancing described previously is thus only used for the second system. Both systems scale nearly perfectly up to one molecule per CPU and with approximately 80% efficiency till one atom per CPU. For even larger number of CPUs, the communication steps required for distributing/replicating the matrices become significant and reduce the parallel efficiency. It is expected that in the hybrid `MPI/openMP` implementation, which we did not yet benchmark, this step will be more efficient. We also wish to emphasize that we have assumed the parallel efficiency to be 100% for the smallest parallel run that lead to a full in-core evaluation of the energy (8 and 16 CPUs respectively). If we would have referenced with respect to a serial run, for which in-core calculations were not possible, parallel efficiency would be significantly larger than 100% for all runs. On 512 CPUs, one MD step takes 62 seconds for the larger system.

4.4.4 Screening

In Tab. 4.3 we present detailed data in order to demonstrate the effect of the different screening methods and the related thresholds. All calculations have been performed on a 32 water cluster employing a DZVP basis set in conjunction with the HSE06 hybrid functional. Shown are absolute errors arising from different combinations of thresholds as well as the impact of the

	$\epsilon_{Schwarz}$	ϵ_{Box}	$\epsilon_{Storage}$	pGGA	memory [MB]	time [s]	abs. error [a.u]
ref)	10^{-12}	none	none	no	75032 (*)	3788	
	10^{-10}	none	10^{-12}	no	24717	340	$1.1750 \cdot 10^{-10}$
a)	10^{-8}	none	10^{-10}	no	14547	278	$2.2298 \cdot 10^{-8}$
	10^{-6}	none	10^{-8}	no	6731	223	$1.4436 \cdot 10^{-6}$
	10^{-10}	10^{-11}	10^{-12}	no	23659	330	$1.1173 \cdot 10^{-10}$
b)	10^{-8}	10^{-9}	10^{-10}	no	13733	269	$2.2298 \cdot 10^{-8}$
	10^{-6}	10^{-7}	10^{-8}	no	6229	216	$1.4435 \cdot 10^{-6}$
	10^{-10}	10^{-11}	10^{-12}	yes	13415	156	$8.1639 \cdot 10^{-9}$
c)	10^{-8}	10^{-9}	10^{-10}	yes	6228	121	$3.1636 \cdot 10^{-9}$
	10^{-6}	10^{-7}	10^{-8}	yes	1410	80	$5.3650 \cdot 10^{-7}$
	10^{-10}	10^{-11}	10^{-11}	yes	11216	156	$7.8486 \cdot 10^{-9}$
d)	10^{-8}	10^{-9}	10^{-9}	yes	4790	121	$3.6432 \cdot 10^{-8}$
	10^{-6}	**10^{-7}**	**10^{-7}**	**yes**	979	80	$4.7480 \cdot 10^{-6}$
	10^{-10}	10^{-11}	10^{-10}	yes	8993	156	$4.1409 \cdot 10^{-9}$
e)	10^{-8}	10^{-9}	10^{-8}	yes	3358	121	$2.7870 \cdot 10^{-7}$
	10^{-6}	10^{-7}	10^{-6}	yes	555	80	$2.8508 \cdot 10^{-5}$

Table 4.3: Shown are absolute errors of several screening methods with respect to a reference energy for a 32-water cluster HSE06/DZVP. When applied, the post-GGA screening is based on a converged PBE wavefunction. All calculations performed on 64 CPU's. ref) Reference calculation without compression/decompression ((*) theoretical memory usage without compression). a) in-core calculations using different thresholds $\epsilon_{Schwarz}$ ($\epsilon_{Storage} = \frac{1}{100} \cdot \epsilon_{Schwarz}$). b) Introduction of far-field screening ($\epsilon_{Box} = \frac{1}{10} \cdot \epsilon_{Schwarz}$) . c) Post-GGA screening for different thresholds $\epsilon_{Schwarz}$. d) $\epsilon_{Storage} = \frac{1}{10} \cdot \epsilon_{Schwarz}$. e) $\epsilon_{Storage} = \epsilon_{Schwarz}$. Bold thresholds denote our chosen default settings.

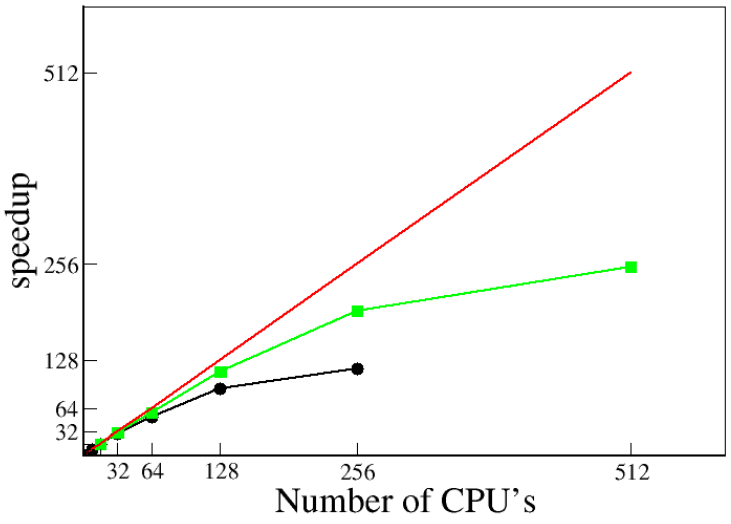

Figure 4.2: Parallel speedup for a 32 water molecule cluster (circles, single-point calculation, 6-31G** basis), and a liquid (PBC) containing 64 water molecules (squares, one MD time step, TZV2P basis) as compared to the ideal speedup (upper line). The speedup is referenced to a run on 8 and 16 CPUs for the small and large system, where these calculations take 740 and 980 seconds, respectively.

several screening procedures on timings and memory consumption. The first calculation in the table (ref) has been done applying Schwarz-screening only with a threshold of $\epsilon_{Schwarz} = 10^{-12}$ and without storing the integrals into memory, i.e. all integrals are recalculated in each SCF step. The resulting converged total energy of this run provides a reference to which we compare all other screening methods.

As to be expected, since the Schwarz-inequality yields an analytic upper bound for the ERIs, the error arising from a finite $\epsilon_{Schwarz}$ can efficiently be controlled by this threshold (a). The same observation holds for the far-field box screening (b), though, due to the moderate size of this system, it does not significantly improve the performance as can be seen from the marginal reduction in memory usage and CPU-time. We find a ten-fold speed-up for in-core calculations. In (c) we present the impact of the post-GGA screening: For this particular system we gain a factor of 2, both in CPU-time and the amount of RAM consumed. For larger systems and basis-sets the gain from the post-GGA screening is typically even more significant. The last

entries in the table (d) and (e) demonstrate the effect of rounding errors in the compression/decompression-scheme. The introduction of $\epsilon_{Storage}$ is indeed necessary, because the accumulation of rounding errors would otherwise introduce errors larger than $\epsilon_{Schwarz}$ in the total energy.

Based on several more tests we decided to chose $\epsilon_{Schwarz} = 10^{-6}$, $\epsilon_{Box} = 10^{-7}$ and $\epsilon_{Storage} = 10^{-7}$ as default thresholds for large scale MD simulations. Using these settings, we reproduce total energies from single-point calculations obtained by other standard quantum chemistry packages to within a few micro-Hartree, and obtain a speed-up of almost 50 in CPU-time and 80 in memory usage as compared to the reference run.

4.4.5 Validation of MTS-scheme

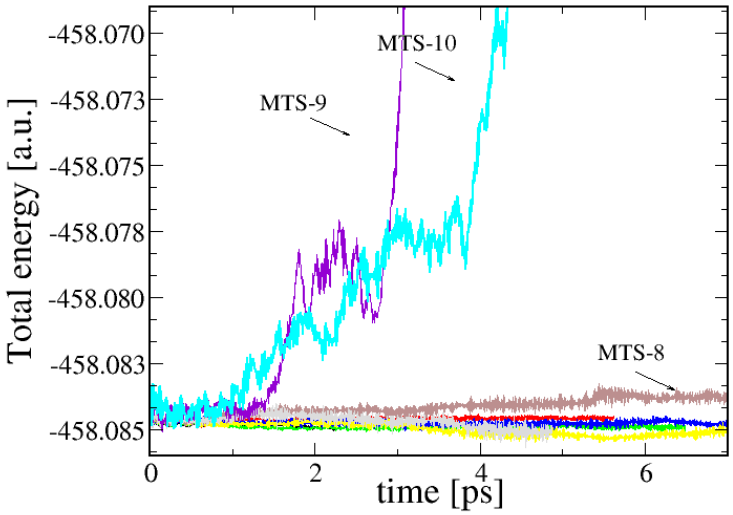

Figure 4.3: Shown is the constant of motion (total energy) for a cluster containing 6 water cluster during MTS MD with various time steps (see text for details). The curves for MTS-2 to MTS-6 lie almost on top of each other, while the MTS-9 and MTS-10 simulations are unstable.

In order to validate the correctness of the MTS-scheme, several MD simulations on a water cluster containing 6 water molecules have been performed. In the inner loop we have employed the PBE functional and a 0.5fs time step, for the outer loop we have employed HSE06, with various time steps. We refer to these as MTS-n, where n refers to the length of the outer loop time

step (n × 0.5fs). Shown in Fig. 4.3 is the constant of motion (total energy) as obtained during a few ps of MTS MD. Stable molecular dynamics is obtained up to n=7 or n=8. The onset of instability corresponds approximately to a time step that equals half the period of the OH stretch. Despite the fact that a time step of 2.5fs is unstable in single time step MD, we consider MTS MD with an outer loop time step of 2.5fs ($n = 5$) a perfectly reasonable choice. Furthermore, we have verified, within the resolution of our simulations (10 – 20 cm^{-1}), that the OH stretching frequency is unaffected by the MTS scheme up to n=7. This is impressive compared to the 200 cm^{-1} shift seen in single time step MD based on a 1.5fs time step.

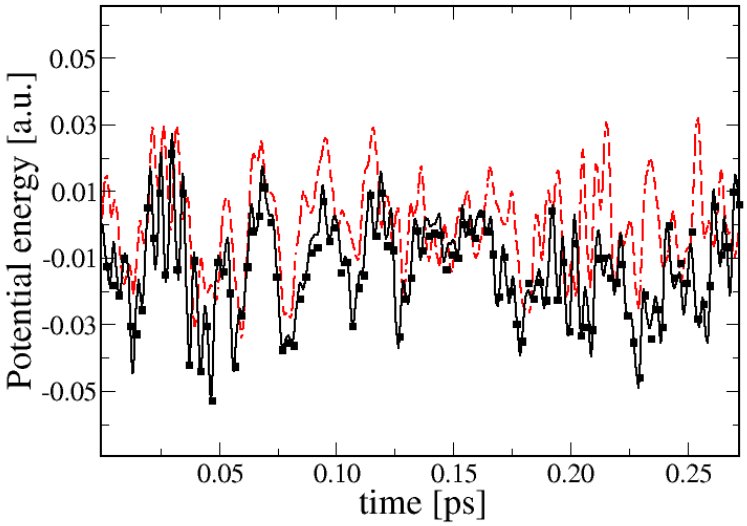

Figure 4.4: Shown are the potential energies for a bulk system of liquid water during MD as obtained with PBE (dashed line), HSE06 (solid line) and HSE06 with the MTS-5 scheme (squares). All simulations were started from the same point in phase-space. To simplify comparison, PBE and HSE06 energies have been aligned at t=0.

Finally, in Fig. 4.4, we compare three MD simulations for bulk liquid water (system details can be found in Sec. 4.6). One simulation uses the MTS-5 scheme, while the two other simulations are traditional single time step (0.5fs) simulations. All three configurations start from the same point in phase space, and the time evolution of the potential energy is monitored. These results show clearly that the MTS-5 run follows closely the HSE06 trajectory, and not the PBE trajectory, despite the fact that the MTS-5 run

only evaluates the HSE06 forces once for every five evaluations of the PBE force. If we compare the timings on 32 CPUs for this system, we observe a 3.6 fold increase in simulation speed when applying the MTS-5 scheme (conventional HSE06 1120s per fs of MD, HSE06 MTS-5 308 s per fs of MD).

4.5 Symmetric radical cation dimers

	He	NH_3	H_2O	HF	Ne	MAE
CCSD(T)	56.04	36.34	40.75	40.22	30.87	0.00
BLYP	83.28	47.40	57.70	67.71	73.23	25.02
B3LYP	77.46	43.14	50.78	58.43	59.12	16.94
HSE06	70.40	42.38	51.02	53.97	54.96	13.70
rCAM-B3LYP	73.95	40.65	46.45	55.02	53.78	13.13
MCY3	73.94	41.66	48.72	55.19	56.55	14.37
SS a = 0.2	54.94	34.61	41.43	46.33	47.95	5.34

Table 4.4: Binding energies in kcal/mol as obtained with several functionals for the radical cations dimers of five small systems and their mean absolute error (MAE). CCSD(T) results are from Ref. [67] and scaled SIC (SS) results from Ref. [68]. Other results have been computed with a 6-311++G(2d,2p) basis.

Hybrid functionals are of particular interest for those systems where local functionals fail dramatically. Small symmetric radical cation dimers (such as e.g. Ne_2^+) are one class of systems for which the self-interaction error (SIE) leads to particularly large errors in binding energies and geometries. In particular, local functionals overbind very strongly, yet predict much too large bond lengths. Using BLYP [23, 24] as an example, Ne_2^+ is overbinding by more than 40 kcal/mol, while the bond is too long by ≈0.2Å. Intuitively, adding HFX exchange reduces the SIE and so hybrid functionals should perform better for these systems. However, the effect is not particularly large. B3LYP, for example, still overbinds Ne_2^+ by 30 kcal/mol. As part of the effort to implement HFX in `CP2K`, we have also implemented two recent hybrid functionals (MCY3 and rCAM-B3LYP) that have been specifically designed to reduce the SIE [41]. Here, we test these and another recent hybrid functionals (HSE06) on five radical cation dimers. We consider the CCSD(T) calculations from Ref. [67] as reference results, and also compare to the results we have obtained with our proposed scaled self-interaction correction

	He	NH_3	H_2O	HF	Ne	MAE
CCSD(T)	1.081	2.173	2.026	1.846	1.724	0.000
BLYP	1.184	2.348	2.310	1.931	1.944	0.173
B3LYP	1.146	2.322	2.088	1.907	1.848	0.092
HSE06	1.133	2.298	2.078	1.897	1.826	0.071
rCAM-B3LYP	1.121	2.147	2.045	1.871	1.756	0.029
MCY3	1.113	2.148	2.047	1.874	1.761	0.029
SS a = 0.2	1.153	2.258	2.123	1.943	1.842	0.093

Table 4.5: Bond length in in Å as obtained with several functionals for the radical cations dimers of five small systems and their mean absolute error (MAE). CCSD(T) results are from Ref. [67] and scaled SIC (SS) results from Ref. [68]. Other results have been computed with a 6-311++G(2d,2p) basis.

(SIC) [68]. The latter scaled SIC (SS) has two empirical parameters, and we refer here to the SS(a=0.2, b=0.0) choice. The advantage of the SS scheme is that it is computationally not more expensive than a local functional. It is currently available only for doublet radicals, and is normally employed within a restricted open shell scheme.

The results are shown in Tab. 4.4 and Tab. 4.5 for binding energies and geometries respectively. It can be seen that all hybrid functionals perform approximately equally poor for the binding energies, with a mean absolute error (MAE) in the range 13–17 kcal/mol, only slightly better than BLYP (MAE 25 kcal/mol). The SS scheme has, with a MAE of 5 kcal/mol, the best performance of all density functionals tested. Given the specific design goal of the the MCY3 and rCAM-B3LYP, we consider it surprising that they do not outperform the other functionals for the energetics of these reactions. However, the geometries of these radical cation dimers suggest that these two functionals represent nevertheless a fundamental improvement over more traditional hybrids. Indeed, the bond lengths obtained with these functionals are in much better agreement with the reference results, and the errors are 2–6 times smaller than those obtained with other hybrid, or local functionals.

4.6 Liquid water

4.6.1 Introduction

There is little need to argue about the importance of water. It is omnipresent in nature and important in technological applications. There is thus a huge interest to understand the structure of the neat liquid, its interactions with solutes, or its reactivity. Experimentally, an atomistic picture of the liquid is most directly obtained from X-ray or neutron diffraction [69, 70], but even the traditional picture of the four-fold coordinated water molecule is still not established firmly [71, 72]. Molecular dynamics simulation of liquid water has started almost four decades ago [73], and the first ab initio simulation of liquid water [74] remains an important milestone for the field. A large number of workers in the field have repeated these ab initio simulations to investigate various aspects of the liquid and the methodology [75, 76, 77, 78, 79, 80, 81, 82, 83, 84, 85, 86, 87, 88, 89, 90]. From these simulations, it becomes clear that DFT, in its various implementations, currently provides a rather reasonable but imperfect model for liquid water. For example, the hydrogen bonding pattern is sound, but the resulting liquid might be over- or understructured depending on the density functional employed [75, 84, 90]. Similarly, it becomes clear that the phase diagram of the model liquid might be different from the experimental one [86] and sensitive to the choice of functional [88]. Furthermore, results can depend on technical details such as the molecular dynamics protocol [81, 82, 87], temperature [84, 83], basis sets [84, 89, 88], and simulation timescales [83, 85]. This sensitivity is ultimately due to the very nature of liquid water, for which, at ambient pressure, the freezing and boiling point are just 100K apart. This implies that very small changes in the energetics, much smaller than the usually quoted chemical accuracy (1 kcal/mol), can have the dramatic effect of being in a different phase. Because of the importance of water, we need to be able to deal with the challenge of simulating this liquid. Not only to understand the neat liquid, but even more importantly, to study, for example, reactive events in solution. From a practical point of view, it might be necessary to just find a computational model that just happens to perform better for this system. However, as improved computational models become accessible, liquid water should be considered a benchmark system that cannot be ignored.

4.6.2 Methods

A total of four simulations of bulk liquid water have been performed. A local functional (PBE) has been employed as a reference, and three simulations based on hybrid functionals (HSE06, 2 × PBE0) have been performed in addition. Three simulations (PBE, HSE06, PBE0) have been started with the same initial positions and velocities. This initial configuration results from a previous simulation [84] based on BLYP (20ps) and further equilibration with PBE (10ps). One run (PBE0(TIP5P)) has been directly started from a configuration generated using MD simulations with a classical force field (TIP5P). [91] All simulations have been performed in the NVE ensemble using samples of 64 water molecules in a cubic box with edges 12.42Å. The simulations have been 11–13 ps in length. The initial part of the trajectory has been discarded, while the last 7.5ps have been used for the analysis. For this period, average temperatures have been 313K, 322K, 325K, and 327K for PBE, HSE06, PBE0 and PBE0(TIP5P) respectively.

Screening thresholds have been $\epsilon_{Schwarz} = 10^{-6}$, $\epsilon_{Box} = 10^{-7}$, $\epsilon_{Storage} = 10^{-7}$, and screening on the initial density matrix has been enabled, leading to in-core simulations. The MTS scheme has been employed, using hybrid functionals with a time step of 2.5fs and the PBE functional with a smaller time step of 0.5fs. The HSE06 simulation employs $\omega = 0.15$, in order to guarantee a sufficiently decayed operator for the MIC scheme, as discussed in Sec. 4.3.6. This value is very similar to the recommended $\omega = 0.11$. The other two hybrid simulations are based on PBE0. However, similar to previous simulations of bulk liquid water [90], we also employ screened exchange in this case, again with $\omega = 0.15$. This functional is thus different from PBE0 as commonly employed, but the energy profiles for the dissociation of a water dimer accurately reproduce those of the original PBE0. During MD, PS extrapolation [14] has been employed to generate the initial density matrix. Wavefunction optimization was based on the OT scheme [52] using 10^{-7} as convergence threshold, leading to energy conserving MD. Pseudopotentials generated with the PBE functional and a TZV2P basis (a total of 2560 basis functions) have been employed in all cases. [14] It has been shown that the TZV2P basis yields converged structural properties at constant density, but might nevertheless not be sufficient to accurately describe the liquid vapor equilibrium [84, 88]. With these settings, trajectories have been produced at a rate of approximately 1ps per day on 256CPUs of a CRAY XT3.

For the analysis, configurations have been stored every time step, a 2.5fs and 0.5fs sampling for hybrid and local functionals respectively. The pair correlation functions have been computed with a bin width of 0.03Å. Diffusion constants have been estimated as the slope of the mean square displace-

ment of the oxygen atoms (averaged over all frames) in the period 2–4ps. The vibrational analysis has been performed using a Fourier transform of the velocity-velocity autocorrelation function in the range -1 – 1 ps. For the electronic analysis, we define the deformation density ($\rho(r)_{\text{deformation}}$) as the difference between the density of the full system and the density of the individual molecules computed in isolation, i.e.

$$\rho(r)_{\text{deformation}} = \rho(r)_{\text{full system}} - \sum_{i=1}^{N} \rho(r)_{\text{molecule}_i}. \tag{4.29}$$

To avoid basis set effects, the individual molecules have been computed in the presence of the basis functions of the full system. The deformation density thus represents the change in the molecular electron density due to interactions with other molecules. In liquid water, this mostly shows the effect of hydrogen bonding. Molecular dipoles in the condensed phase have been computed using the centers of the maximally localized Wannier functions [76]. In the condensed phase, molecular dipoles converge quickly with respect to the basis [92].

4.6.3 Results and discussion

The structure of the liquid is most easily described using pair correlation functions. These results are shown in Fig. 4.5 and Fig. 4.6 for the oxygen-oxygen and oxygen-hydrogen pair correlation functions, respectively. Clearly, within the statistical uncertainty, the curves as obtained with the different functionals superimpose almost perfectly. The height of the first peak in the oxygen-oxygen pair correlation function is approximately 3.4 in all cases, which is significantly above the experimental estimates [69, 70]. The self diffusion constant cannot be obtained with good statistical accuracy from these relatively short simulations, but our estimates all lie in the range 0.013–0.055 Å^2/ps. This is roughly ten times smaller than the experimental number. We must therefore conclude that hybrids do not necessarily improve the agreement with the experimental results. In particular, at the selected density and temperature, the system remains in a glass-like state. With the PBE0 simulation initiated from a liquid-like TIP5P configuration, this glass-like state is also found quickly, implying that this result is independent from the initial configuration used for the simulation.

At first sight, this result is at variance with the conclusions of an earlier simulation of liquid water based on hybrid functionals [90]. In these simulations, hybrids yield consistently softer pair correlation functions than their non-hybrid counterparts, by 0.3–0.5 units. We believe, however, that this

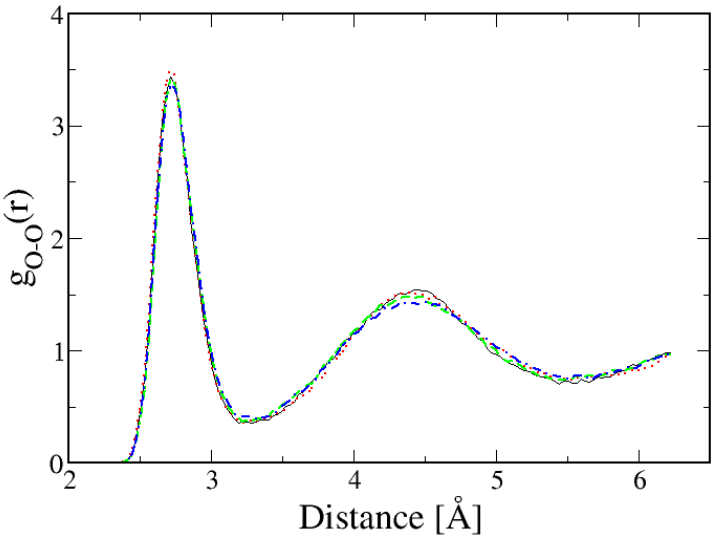

Figure 4.5: Oxygen-Oxygen pair correlation functions as obtained with three different functionals. The local functional employed is PBE (solid line) and the hybrid functionals are HSE06 (dotted line) and PBE0. Two PBE0 simulations have been initiated from either a PBE or a TIP5P initial geometry. The former is shown with a dashed line while the latter is shown with a dashed-dotted line.

could be due to difference in thermodynamic state employed in the simulations. The simulations in Ref. [90] are at higher temperature (350K) and lower density (2.5%), which yields a much more liquid-like system. It could therefore be that in these different phases (glass- or liquid-like) the system reacts differently on the change of functional; an observation which merits further investigation. These results have also a somewhat disappointing practical consequence: for the temperature and density conditions employed here, simulations based on hybrid functionals will face similar difficulties as simulations based on local functionals. In particular, long MD simulations might be required to perform sufficient sampling of solvent configurations around solutes. Nevertheless, since the description of the liquid does not become worse, hybrid functionals will remain the functionals of choice if solutes or properties of solutes need to be described for which local functionals are known to be inaccurate.

Despite the similarity in liquid structure, it is interesting to investigate if

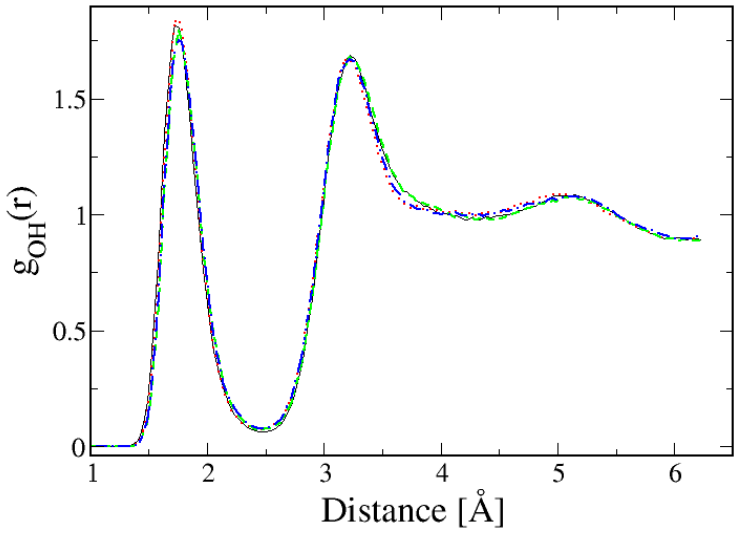

Figure 4.6: The intermolecular Oxygen-Hydrogen pair correlation functions as obtained with three different functionals. Same legend as Fig. 4.5

differences between hybrid and local functionals can be found at the level of the electronic structure. We perform this analysis on a single configuration extracted from an HSE06 simulation. By using a fixed configuration, electronic effects can be disentangled from differences in structure. As explained in Sec. 4.6.2, the deformation density shows the effect of intermolecular interactions on the electron density. The difference in deformation density is shown in Fig. 4.7 for PBE and HSE06. This figure illustrates clearly that a local functional, such as PBE, has a larger charge transfer in the hydrogen bond than the corresponding non-hybrid functional. An alternative and complementary way to investigate this effect is through the molecular dipoles. In Fig. 4.8, a comparison is shown between the molecular dipoles as obtained with PBE and HSE06. It can be seen that the PBE dipoles are almost always larger than the corresponding HSE06 dipoles. This is consistent with the previously mentioned tendency for charge transfer in the hydrogen bond. Furthermore, we see that the effect is larger for molecules having a larger dipole, i.e. for molecules that are likely to be in a more polarizing environment. Indeed, the charge transfer effect we observe in the liquid is present, but less pronounced, in the water dimer system (results not shown). This tendency of local functional to delocalize charges, is to some extend a

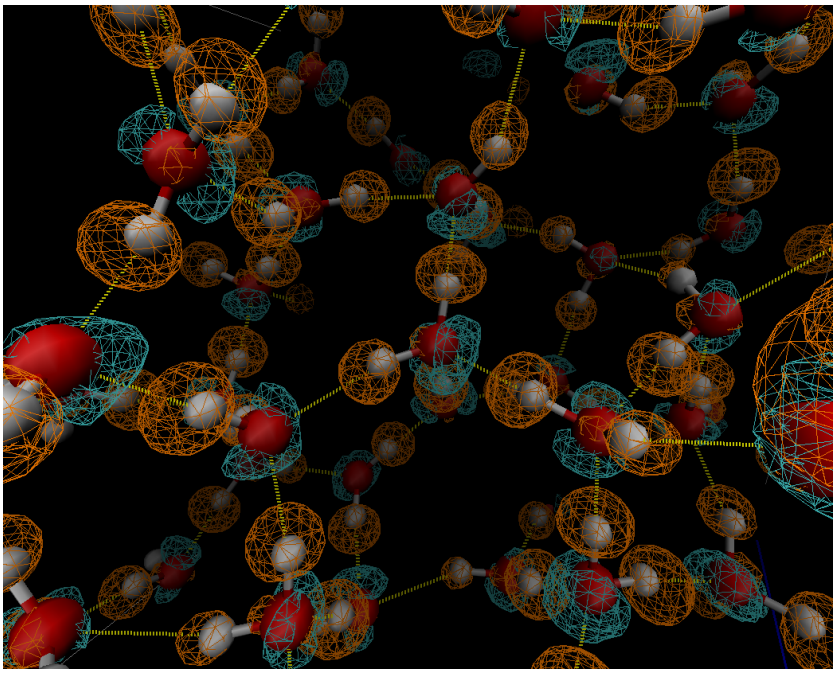

Figure 4.7: Shown is the difference in deformation density (see text for definition) between an HSE06 and a PBE calculation for a selected configuration of liquid water. The contours are shown at +0.0003 a.u. and -0.0003 a.u. The lobes on the hydrogen (orange contours) show regions in space where the PBE calculation results in more density than the HSE06 calculation, while the lobes near the lone pairs of the water (cyan contours) indicate more density in the HSE06 calculation. This result clearly shows a reduced charge transfer in the hydrogen bond for the hybrid functional.

self-interaction problem, and might ultimately be related to the band gap problem [93]. As expected, a hybrid functional opens the gap, and computed HOMO-LUMO gaps for this configuration are 5.0eV and 6.6eV for PBE and HSE06, respectively. Charge delocalization around charged species in solution is an active topic of current research, and it might be interesting to investigate what hybrids functionals predict [94].

Finally, we believe that a signature of the charge transfer effect can be observed through a vibrational analysis of the MD trajectories. In particular, the O–H stretching band should be sensitive to the precise nature of the hydrogen bond. An OH involved in a stronger hydrogen bond should vibrate at a lower frequency than a free OH group. For example, the O–H stretching frequency of liquid water is at about 3400 cm^{-1}, while a free water molecule

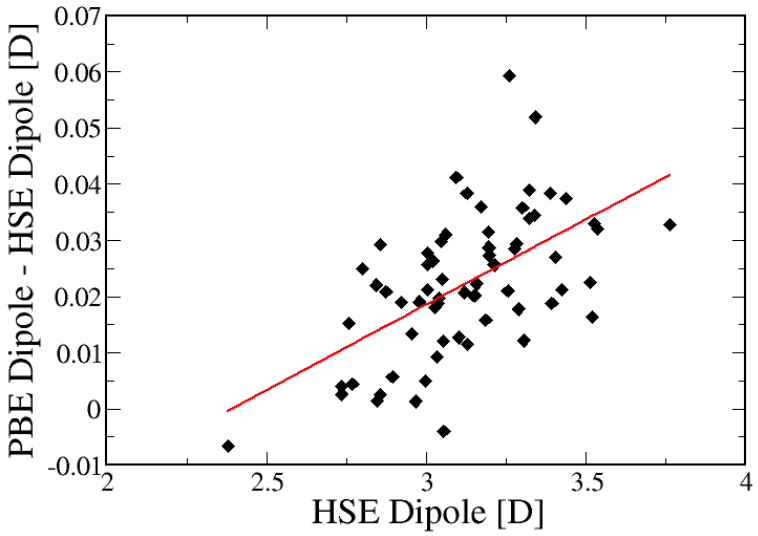

Figure 4.8: Shown is the difference between the molecular dipoles as obtained by HSE06 and PBE calculations for a selected configuration of liquid water. Diamonds represent results for individual molecules, while the solid line is a linear least square fit. Molecular dipoles are generally larger with PBE than with HSE06, and this difference increases as the molecular dipole increases.

and amorphous ice have vibrations at about 350 cm^{-1} higher and 280 cm^{-1} lower frequencies, respectively. In Fig. 4.9, we compare the O–H stretching bands as obtained from the MD simulations through the Fourier transform of the velocity–velocity autocorrelation function. We have shifted the results obtained with the hybrid functionals by 163 cm^{-1} to account for the large difference (163 cm^{-1}) between PBE and PBE0 in the O–H stretching frequency of a single water molecule in the gas phase. In this way, the upper edge of the band, which likely corresponds to free OH groups, is aligned for all functionals. The lower edge of the band nevertheless shows a significantly earlier onset ($\approx$ 70 cm^{-1}) for PBE than for any of the hybrid functionals. This result would suggest a smaller population of strong hydrogen bonds in simulations based on hybrid functionals.

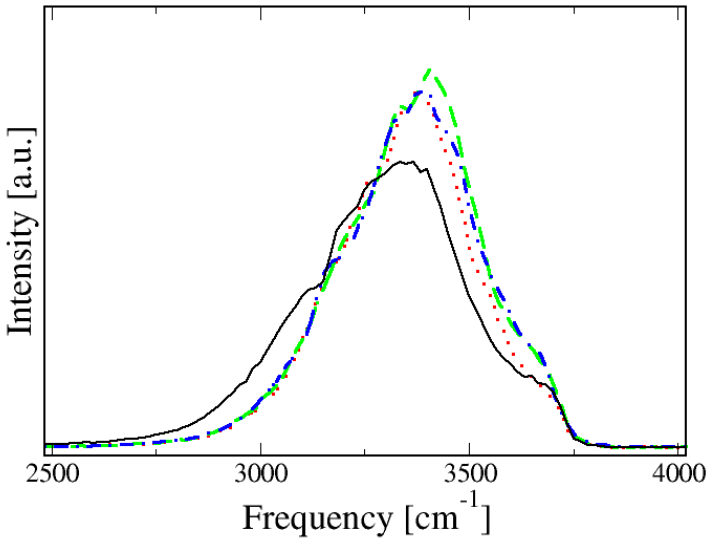

Figure 4.9: Shown is a frequency analysis of the OH-stretching band in liquid water as obtained with local and hybrid functionals. The profiles of the hybrids have been shifted to lower frequencies by 163cm^{-1} (see text for details). Same legend as Fig. 4.5

4.7 Conclusions

In this work, we have presented the implementation of HFX in `CP2K`. Several techniques have been combined to increase the efficiency of hybrid molecular dynamics simulations, while accuracy and robustness is retained. As expected, the cost of simulations based on hybrid functionals exceeds the cost of simulations based on local functionals significantly. Depending on the basis set, system and implementation, one can expect hybrid MD to be up to 100 times more expensive than simulations based on local functionals. This increase in cost is not prohibitive, and we thus expect hybrid functionals to be used to verify results obtained with local functionals, or to study systems where the inclusion of HFX is necessary to obtain qualitative correct results. As a first challenging benchmark for our implementation, we have performed extensive molecular dynamics simulations of liquid water. Several samples of 64 molecules have been simulated for over 10 ps each, with large basis sets and tight SCF convergence, at a rate of 1ps/day. These results have shown negligible differences between a local functional (PBE) and two

closely related hybrids (HSE06, PBE0) for structural properties, even though some small difference have been found on the electronic level that might be reflected in the vibrational spectrum. Overall, the agreement with experiment is not yet fully satisfactory. This suggests that there are still effects, for example van der Waals interactions, nuclear quantum effects, or technical aspects, that are not yet accurately accounted for in the simulation methodology or functionals. Nevertheless, we expect that the real power of hybrid functionals in ab initio molecular dynamics simulation is revealed in more complex systems, where chemical reactivity plays a crucial role. With the tools and simulation protocols presented here, it will be possible to perform ab initio molecular dynamics simulations based on hybrid functionals on a more or less routine basis.

Chapter 5

Robust periodic Hartree-Fock Exchange for large scale simulations using Gaussian basis sets [95]

Hartree-Fock exchange with a truncated Coulomb operator has recently been discussed in the context of periodic plane-waves calculations [J. Spencer, A. Alavi, Phys. Rev. B **77** 193110 (2008)]. In this work, this approach is extended to Gaussian basis sets, leading to a stable and accurate procedure for evaluating Hartree-Fock exchange at the Γ–point. Furthermore, it has been found that standard hybrid functionals can be transformed into short-range functionals without loss of accuracy. The well defined short-range nature of the truncated exchange operator can naturally be exploited in integral screening procedures and makes this approach interesting for both condensed and gas phase systems. The presented Hartree-Fock implementation is massively parallel and scales up to 10'000s of cores. This makes it feasible to perform highly accurate calculations on systems containing 1'000s of atoms or 10'000s of basis functions. The applicability of this scheme is demonstrated by calculating the cohesive energy of a LiH crystal close to the Hartree-Fock basis set limit and by performing an electronic structure calculation of a complete protein (Rubredoxin) in solution with a large and flexible basis set.

5.1 Introduction

The construction of reliable models for the exchange and correlation energy of electrons is an active research field within the density functional theory

(DFT) community. For nearly fifty years, new ideas and new approximations have been proposed that increase the accuracy and are improvements compared to the local density approximation [11, 27] (LDA). Nowadays, most new functionals go beyond the semi-local generalized gradient approximations [23, 24, 96] (GGA's) by incorporating a certain amount of Hartree-Fock exchange (HFX) or similar non-local functionals [97, 31, 32, 98, 99, 100, 101]. Generally, these hybrid functionals are more accurate than their local counterparts. Whereas the use of these hybrid functionals is well established in the quantum chemistry community for the study of molecules, condensed phase systems, such as liquids or solids, are usually treated at a GGA level. Not only is the cost of computing exchange interactions in large condensed phase systems significant, the technical difficulty of obtaining results that are accurate and properly converged can not be underestimated in calculations employing periodic boundary conditions (PBC). In this work, a robust and accurate scheme, suitable for large condensed phase systems is presented.

In recent work, Ref. [35], we have presented a linear scaling implementation of HFX has been presented that makes it feasible to perform large scale molecular dynamics simulations with hybrid functionals in PBC. The focus on large systems has guided several design decisions for the implementation. Atom centered Gaussian basis functions are employed, which makes a linear scaling implementation, based on a screening with the density matrix elements, relatively straightforward [42, 51, 48]. Additionally, large systems can be described without **k**-point sampling, and the approach is thus Γ–point only. All algorithms are massively parallel and focus on in-core operation to allow for thousands of MD steps in a reasonable time. Our initial implementation of periodic HFX at the Γ–point has been based on an approach by Challacombe and co-workers [102]. In this scheme, the minimum image convention (MIC) is applied at the level of primitives while computing the four center integrals. This is efficient and has been shown to accurately converge to reference results as the system size is increased [102]. However, it has been observed that this approximation is generally unstable if extended or flexible Gaussian basis sets are used. The instability is the result of a spurious minimum in the energy functional, yielding an unphysical wavefunction with a total energy that can be several Hartrees beyond the physical solution. This is similar to the behavior observed in traditional HFX calculations that employ a too loose screening threshold. As will be discussed in more detail below, in the MIC there is no screening parameter which can be adjusted to guarantee stability. The new approach presented here does not employ the MIC, only requires the Γ–point, and is stable with large and flexible basis sets. The use of the truncated Coulomb operator [103] is a key ingredient. All algorithms and methods presented are implemented within the frame-

work of the `CP2K/Quickstep` [36, 14] program, a freely avaliable molecular simulation package.

5.2 The truncated Coulomb operator for calculations at the Γ–point using Gaussian basis sets

5.2.1 Periodic Hartree Fock calculations

For finite systems such as molecules, which employ open boundary conditions, the Hartree-Fock exchange energy is computed from its definition

$$E_x^{\text{open}} = -\frac{1}{2}\sum_{i,j}\int\int \psi_i(r_1)\psi_j(r_1)g(|r_1-r_2|)\psi_i(r_2)\psi_j(r_2)\,d^3r_1 d^3r_2. \quad (5.1)$$

The potential $g(|r_1 - r_2|) = \frac{1}{|r_1-r_2|} = \frac{1}{r_{12}}$ in conventional HFX calculations, but is commonly replaced by other operators, such as $\text{erfc}(\omega r_{12})/r_{12}$, $exp(-\omega^2 r^2)$ or $\exp(-\omega r)/r$ in modern electronic structure theory [31, 32, 41, 104]. Computing this energy poses no special problems. In the condensed phase, the HFX energy must take the periodic nature of the system into account, and an integration over **k**–vectors, which reflects translational invariance and the infinite nature of the system, is formally required. In practice, a finite mesh of **k**–points is employed, which usually becomes less dense as the unit cell increases in size. The HFX energy in periodic systems is thus defined as

$$E_x^{\text{PBC}} = -\frac{1}{2N_k}\sum_{i,j}\sum_{\mathbf{k},\mathbf{k}'}\int\int \psi_i^{\mathbf{k}}(r_1)\psi_j^{\mathbf{k}'}(r_1)g(|r_1-r_2|)\psi_i^{\mathbf{k}}(r_2)\psi_j^{\mathbf{k}'}(r_2)\,d^3r_1 d^3r_2 \quad (5.2)$$

Where N_k is the number of **k**–points within the Brillouin zone, and the integrals are over all space. The wave functions are assumed to be normalized over the crystal volume $N_k V$ where V is the volume of the unit cell. This expression, however, is troublesome to compute. The reason for this is the integratable singularity at $\mathbf{k} = \mathbf{k}'$, which is related to the conditionally convergent nature of the integral for that choice of **k**–vectors. Several schemes have been developed to obtain good convergence with respect to the **k**–point sum [39, 105, 106, 107, 108]. Of particular interest here, is the method by Spencer and Alavi [103]. This method is based on the observation that the

truncated Coulomb (TC) operator

$$g_{TC}(r_{12}) = \begin{cases} \frac{1}{r_{12}}, & r_{12} \leq R_c \\ 0, & r_{12} > R_c \end{cases} \tag{5.3}$$

yields an expression for the HFX energy that does not exhibit a singularity at $\mathbf{k} = \mathbf{k}'$, that converges to the exact expression as R_c goes to infinity, and that becomes increasingly easy to converge in **k**-space as R_c becomes smaller. It is intuitive that, contrary to the Hartree energy, the exchange energy converges rapidly with R_c for the TC operator. Since the convergence of the exchange energy is related to the decay of the density matrix, it will be most rapid for systems with a large gap. However, this also means that the minimum R_c which yields a properly converged exchange energy is a system dependent property. As illustrated in Sec. 5.3, the exchange energy computed with g_{TC}, in open systems or with full **k**–point convergence, decreases monotonically to its limiting value for increasing R_c. Clearly, one can define truncated versions of other commonly employed operators. In Ref. [103], it is demonstrated that it is reasonable to take the number of **k**–points as

$$N_k \approx \frac{4\pi}{3} R_c^3 \frac{1}{V} \tag{5.4}$$

(see that work for an in–depth discussion). Once R_c is fixed, Eq. 5.4 shows that the Γ–point alone will be sufficient for large systems, since large systems imply a large V. For a cubic unit cell with edges of length L, Eq. 5.4 suggests that having $R_c < 0.62L$ is sufficient for Γ–point only sampling. If needed, sufficiently large systems can always be obtained by replicating the unit cell in all directions. The Γ–point expression for the exchange energy is given by

$$E_x^{\Gamma} = -\frac{1}{2} \sum_{i,j} \int \int \psi_i^{\mathbf{0}}(r_1) \psi_j^{\mathbf{0}}(r_1) g_{TC}(|r_1 - r_2|) \psi_i^{\mathbf{0}}(r_2) \psi_j^{\mathbf{0}}(r_2)\, d^3r_1 d^3r_2 \tag{5.5}$$

This expression for E_x^{Γ} looks similar to the one for E_x^{open} (Eq. 5.1). However, E_x^{Γ} will diverge for $R_c \to \infty$. It has to be emphasized that only for a finite range of R_c, i.e. sufficiently small to allow for Γ–point only sampling of the integral, E_x^{Γ} as defined by Eq. 5.5 will be a meaningful approximation to the full **k**–space integrated HFX energy. A hand–waving argument for the fact that the Γ–point only expression implies a limit on R_c can also be made as follows: for well localized electrons (i.e. if the maximally localized Wannier functions fit the unit cell), the exchange energy between electrons in different unit cells of the system is small. However, Eq. 5.5 would nevertheless predict a large contribution to the exchange energy for an electron and its 'periodic

image' if R_c is large enough. This spurious 'self-exchange' with the image electron should not be present and R_c needs thus to be chosen accordingly. Based on this reasoning, a somewhat more conservative rule than Eq. 5.4 for determining the maximum R_c can be proposed: R_c should be smaller than or equal to the radius of the largest sphere that fits the unit cell. This guarantees, for localized electrons, that no interactions with image electrons are possible. For cubic unit cells this yields $R_c \leq L/2$, similar to Eq. 5.4, while for orthorhombic or strongly distorted triclinic unit cells this estimate can be significantly different from Eq. 5.4.

The expression for the Hartree-Fock energy at the Γ–point Eq. 5.5 can be computed per unit cell and in an atom centered basis set as

$$E_x^{\Gamma} = -\frac{1}{2} \sum_{\lambda\sigma\mu\nu} P^{\mu\sigma} P^{\nu\lambda} \sum_{\mathbf{abc}} \left(\mu\nu^{\mathbf{a}}|\lambda^{\mathbf{b}}\sigma^{\mathbf{b+c}}\right)_{g_{TC}}, \tag{5.6}$$

with $\mathbf{a}, \mathbf{b}$ and $\mathbf{c}$ denoting translations of the unit cell. This exact result can be obtained easily by introducing in Eq. 5.5 the expression of the periodic wavefunction in an atomic orbital basis

$$\psi_i(r) = \sum_{\mu\mathbf{a}} C^{\mu i} \phi_{\mu}^{\mathbf{a}}(r) \tag{5.7}$$

Here, $C^{\mu i}$ are the wavefunction coefficients, which are complex in the general case, but can be taken real at the Γ–point. $\phi_{\mu}^{\mathbf{a}}(r)$ are the atom centered basis sets, translated by a multiple of the unit cell given by $\mathbf{a}$. The density matrix elements $P^{\mu\nu}$ are obtained from $\sum_i C^{\mu i} C^{\nu i}$. The two electron four center integrals are defined as

$$\left(\mu\nu^{\mathbf{a}}|\lambda^{\mathbf{b}}\sigma^{\mathbf{b+c}}\right)_{g_{TC}} = \int\int \mu(\mathbf{r}_1)\nu^{\mathbf{a}}(\mathbf{r}_1) g_{TC}(r_{12}) \lambda^{\mathbf{b}}(\mathbf{r}_2)\sigma^{\mathbf{b+c}}(\mathbf{r}_2) d\mathbf{r}_1 d\mathbf{r}_2 \tag{5.8}$$

These integrals can be obtained analytically for the TC operator and their numerical treatment will be discussed in detail in Sec. 5.2.3. The triple sum over the lattice vectors in Eq. 5.6 converges quickly in $\mathbf{a}$ and $\mathbf{c}$ because the overlap of the corresponding Gaussian basis functions decays quickly with distance, while the sum over $\mathbf{b}$ is finite by virtue of the short-range nature of the truncated Coulomb operator. In Eq. 5.6, all terms that are larger than a given screening threshold $\epsilon_{\text{screening}}$ should be retained. As discussed in more detail in Sec. 5.5.3, screening based on the traditional Schwarz-inequality combined with a simple distance criterium based on the centers of the product densities $\mu\nu^{\mathbf{a}}$ and $\lambda^{\mathbf{b}}\sigma^{\mathbf{b+c}}$ can be used to eliminate negligible terms.

Basis set	Total energy [a.u.]	
	$\frac{1}{r}$	$\frac{\mathrm{erfc}(\omega r)}{r}$
SZV	-33.531805	-32.552246
DZVP	-33.781652	-32.801068
TZVP	-33.798435	-32.817981
TZV2P	-83.287255	-33.827285
QZV2P	-219.806121	-41.438744

Table 5.1: PBC Hartree-Fock total energies [Hartree] computed with the minimum image convention for two operators, the conventional $\frac{1}{r}$ Coulomb potential and a short-range potential $\frac{\mathrm{erfc}(\omega r)}{r}$ with $\omega = 0.11$. The system consists of two water molecules, described with pseudo potentials, in a cubic unit cell with $L = 12.42$ Å and with a geometry that appears sensitive to the instability. It can be observed that the total energy converges to an unphysical result as soon as the basis set quality reaches TZV2P.

At this point, some differences and similarities between the approach summarized by Eq. 5.6, and the MIC, proposed in Ref. [102] shall be discussed. First, there is the difference in operator $g(r)$, which is the conventional $1/r$ in the MIC and the TC operator (Eq. 5.3) here. Second, in the MIC, one retains only one term from the sum over $\mathbf{b}$, i.e. that particular index $\mathbf{b}'$ which guarantees that the distance between the centers of the product densities $\mu\nu^{\mathbf{a}}$ and $\lambda^{\mathbf{b}'}\sigma^{\mathbf{b}'+\mathbf{c}}$ is as small as possible. This is usually the dominant contribution to the sum, but generally ignores terms larger than a given $\epsilon_{\text{screening}}$. With increasing basis set size and quality, this leads to a spurious minimum in the MIC HFX energy functional. This instability is illustrated in Tab. 5.1 and analyzed in some more detail in App. 5.5.2. Note, that for potentials with shorter range, such as $\mathrm{erfc}(\omega r)/r$, the instability is less pronounced. The new method based on the TC operator and the full sum is stable for all basis sets employed, as shown in Tab. 5.2. The total energy converges rapidly with R_c, reaching, for this simple system, a plateau at $R_c \approx 4$ Å. As expected, for R_c larger than the value suggested by Eq. 5.4, 7.7 Å for this system, Γ–point sampling is not sufficient anymore, and the integral diverges. Also the more conservative choice ($R_c = L/2$ for cubic cells), gives good results. Comparing Tab. 5.1 and Tab. 5.2, it can be seen that the MIC results equal the results of the truncated method with $R_c = L/2$ to micro-Hartree accuracy in the case where the MIC procedure is stable, i.e. the SZV, DZVP and TZVP basis sets. Even though the instability of the MIC procedure is fundamental, this ap-

R_c	SZV	DZVP	TZVP	TZV2P	QZV2P
$R_c = 0.5$	-30.074404	-30.273802	-30.298149	-30.309740	-30.330732
$R_c = 1.0$	-32.693538	-33.024934	-33.052548	-33.061415	-33.064684
$R_c = 2.0$	-33.459119	-33.722827	-33.738480	-33.747451	-33.750486
$R_c = 3.0$	-33.527563	-33.778845	-33.794977	-33.803751	-33.807027
$R_c = 4.0$	-33.531707	-33.781608	-33.798342	-33.807131	-33.810757
$R_c = 5.0$	-33.531804	-33.781651	-33.798433	-33.807222	-33.810894
$\mathbf{R_c = 6.0}$	**-33.531805**	**-33.781652**	**-33.798435**	**-33.807224**	**-33.810898**
$R_c = 7.0$	-33.531805	-33.781652	-33.798435	-33.807224	-33.810898
$R_c = 8.0$	-33.531806	-33.781652	-33.798436	-33.807225	-33.810900
$R_c = 10.0$	-33.533982	-33.783206	-33.800223	-33.809006	-33.812843
$R_c = 12.0$	-33.912427	-34.152952	-34.170470	-34.179272	-34.183189
$R_c = 16.0$	-33.533982	-35.851041	-35.869063	-35.877848	-35.882304

Table 5.2: PBC Hartree-Fock total energies [Hartree] with the scheme for the truncated Coulomb operator outlined in the text, for various choices of R_c [Å]. The system is the same as the one described in Tab. 5.1, but results are stable, independent of the basis set. For large values of R_c, the Γ–point sampling of the exchange energy is not sufficient. As discussed in the text, the choice of $R_c \approx L/2 \approx 6.0$ Å (shown in bold) guarantees that no spurious self exchange parts enter the Γ–point calculation.

proach is, by construction, able to eliminate the spurious self-exchange with image electrons, even if the conventional Coulomb operator is used. Further validation and testing of the truncated Coulomb potential method based on Eq. 5.6 is presented in Sec. 5.3.

5.2.2 A long-range correction to the truncated Coulomb operator

In the limit $R_c \to \infty$ the truncated and the full Coulomb potential become identical. In the context of hybrid density functionals the question arises, whether the missing long-range exchange at finite R_c can be corrected by the long-range part of a local density functional. In a similar fashion this has been done for the HSE06 [31, 32] hybrid functional that uses the short-range $\mathrm{erfc}(\omega r)/r$ potential. The basic concept behind this range separation relies on the fact that the exchange energy can be written in terms of the

spherically averaged exchange hole $\rho_{\mathrm{xc}}^{\mathrm{SA}}(\mathbf{r}, s)$

$$E_{\mathrm{x}}^{\mathrm{DFT}}[\rho] = \frac{1}{2}\int \rho(\mathbf{r})d\mathbf{r}\int_0^\infty 4\pi u\rho_{\mathrm{xc}}^{\mathrm{SA}}(\mathbf{r}, u)du, \tag{5.9}$$

where u denotes the electron-electron interaction distance. The long-range part for a system that interacts via a truncated Coulomb potential is then simply given by

$$E_{\mathrm{x}}^{\mathrm{DFT,LRC}}[\rho] = \frac{1}{2}\int \rho(\mathbf{r})d\mathbf{r}\int_{R_c}^\infty 4\pi u\rho_{\mathrm{x}}^{\mathrm{SA}}(\mathbf{r}, u)du. \tag{5.10}$$

Within this range-separation *ansatz*, the exchange energy can be written as

$$E_{\mathrm{x}} = E_x^{\mathrm{HF,TC}} + E_{\mathrm{x}}^{\mathrm{DFT,LRC}}. \tag{5.11}$$

For convenience, a model with an analytical expression of the spherically averaged exchange hole has been chosen. Similar to the range-separated hybrid functional of Heyd et al., the starting point for the long-range correction is the exchange hole formulation of the PBE functional by Ernzerhof and Perdew [109].

The PBE exchange energy is defined via an integral over the exchange energy density $\epsilon_x^{\mathrm{PBE}}$

$$E_x^{\mathrm{PBE}} = \int \rho(\mathbf{r})\epsilon_x^{\mathrm{PBE}}(\rho, \nabla\rho)d\mathbf{r}. \tag{5.12}$$

$\epsilon_x^{\mathrm{PBE}}$ is a function of the electron density $\rho(\mathbf{r})$ and its gradient $\nabla\rho(\mathbf{r})$ and is defined as the product of the LDA exchange energy density and an enhancement factor F_x^{PBE} that additionally depends on the gradient of the electronic density

$$\epsilon_x^{\mathrm{PBE}}(\rho, \nabla\rho) = \epsilon_x^{\mathrm{LDA}}(\rho) \cdot F_x^{\mathrm{PBE}}(\rho, \nabla\rho). \tag{5.13}$$

The PBE exchange hole model J_x^{PBE} enters into the definition of the enhancement factor, defining the latter to be an integral of the following kind

$$F_x^{\mathrm{PBE}}(s) = -\frac{8}{9}\int_0^\infty y J_x^{\mathrm{PBE}}(s, y)dy \tag{5.14}$$

with $s = \frac{|\nabla\rho|}{2\pi k_F\rho}$ the reduced gradient, k_F being the local Fermi vector and $y = k_F u$ the scaled interaction coordinate. For the analytic expression of

J_x^{PBE} the following parametrized form

$$\begin{aligned} J_x^{\mathrm{PBE}}(s,y) &= \Bigg[-\frac{A}{y^2}\frac{1}{1+(4/9)Ay^2} \\ &+ \left(\frac{A}{y^2} + B + C\left[1+s^2F(s)\right]y^2\right. \\ &+ \left. E[1+s^2G(s)]y^4\right)\exp(-Dy^2)\Bigg] \\ &\times \exp(-s^2H(s)y^2), \end{aligned} \tag{5.15}$$

with parameters $A-E$ being constants and F, G, and H functions of the reduced gradient, has been found by Ernzerhof et al. (see Ref. [109] for details). For the current purpose, the long-range enhancement factor is given by

$$F_x^{\mathrm{PBE,LRC}}(s) = -\frac{8}{9}\int_{R_c'}^{\infty} y J_x^{\mathrm{PBE}}(s,y)dy \tag{5.16}$$

with $R_c' = R_c k_F$. This integration can be carried out analytically (see App. 5.5.1) yielding an expression for the long-range correction of the exchange energy.
The final form of the range separated exchange energy reads now

$$E_x = E_x^{\mathrm{HF,TC}}(R_c) + E_x^{\mathrm{PBE,LRC}}(R_c), \tag{5.17}$$

both parts depending on the cutoff radius R_c.
Using these results one can define three different hybrid functionals:

$$\text{PBE0} \quad : \quad E_{\mathrm{xc}}^{\mathrm{PBE0}} = aE_x^{\mathrm{HF}} + (1-a)E_x^{\mathrm{PBE}} + E_c^{\mathrm{PBE}} \tag{5.18}$$

$$\text{PBE0-TC} \quad : \quad E_{\mathrm{xc}}^{\mathrm{PBE0\text{-}TC}} = aE_x^{\mathrm{HF,TC}} + (1-a)E_x^{\mathrm{PBE}} + E_c^{\mathrm{PBE}} \tag{5.19}$$

$$\begin{aligned} \text{PBE0-TC-LRC} \quad &: \quad E_{\mathrm{xc}}^{\mathrm{PBE0\text{-}TC\text{-}LRC}} = aE_x^{\mathrm{HF,TC}} + aE_x^{\mathrm{PBE,LRC}} \\ &+ \quad (1-a)E_x^{\mathrm{PBE}} + E_c^{\mathrm{PBE}}. \end{aligned} \tag{5.20}$$

PBE0 is, for $a = 0.25$, the standard PBE hybrid functional [28, 29, 30]. PBE0-TC denotes the original functional of PBE0 in which the standard Hartree-Fock exchange energy is replaced by the truncated Coulomb (TC) expression with cutoff radius R_c, and PBE0-TC-LRC the PBE0-TC functional with the long-range correction (LRC) based on the PBE exchange hole. Of course, similar variants can be defined for other hybrid functionals. It is demonstrated in Sec. 5.3.2 that the use of a LRC allows for a very small R_c (≈ 2 Å), without negatively impacting the performance of the functional

for typical thermochemical quantities. Hartree-Fock exchange with such a short range can be evaluated very efficiently. Note, that in the limit of R_c going to zero the PBE functional is recovered, but based in part on the spherically averaged PBE exchange hole.

5.2.3 Efficient calculation of two electron integrals for general $g(r)$

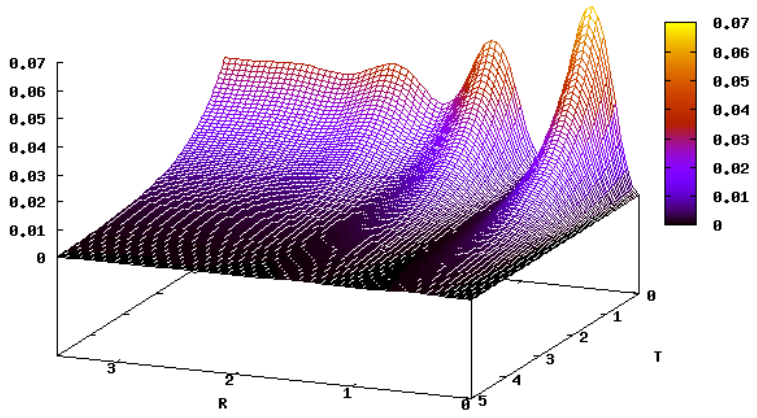

Figure 5.1: The figure shows $G_{14}(R'_c, T)$ as defined by Eq. 5.21 and Eq. 5.23 for the truncated Coulomb operator.

Two electron four center integrals are commonly calculated analytically using recurrences [33, 3, 50]. `CP2K` employs the `LIBINT` [34] library for this. These algorithms start from the lowest angular momentum interaction, i.e. $(ss|ss)_g$, for a given interaction potential $g(r_{12})$ and then recursively calculate higher order contributions from that. In order to calculate integrals with a total angular momentum n, these routines have to be provided with $n+1$ initial values, the starting vector. With the notation used by Ahlrichs [50],

this reads as

$$G_n(\rho, T) = \left(-\frac{\partial}{\partial T}\right)^n G_0(\rho, T) \tag{5.21}$$

$$G_0(\rho, T) = \frac{2\pi}{\rho^{\frac{3}{2}}\sqrt{T}} \int_0^\infty g\left(\frac{y}{\sqrt{\rho}}\right) y e^{-y^2-T} \sinh(2y\sqrt{T}) dy, \tag{5.22}$$

where T and ρ are parameters determined by the geometry and the involved Gaussian basis functions. For several commonly used operators, there exist efficient recursive formulae to calculate the higher order derivatives. In the case of the full range Coulomb potential the whole procedure reduces to an evaluation of the Γ–function at various parameters T. For the truncated Coulomb potential one arrives at

$$G_0(\rho, T, R_c') = \frac{\pi^{\frac{3}{2}}}{2\rho} \frac{2\mathrm{erf}(\sqrt{T}) + \mathrm{erf}(R_c' - \sqrt{T}) - \mathrm{erf}(R_c' + \sqrt{T})}{\sqrt{T}}, \tag{5.23}$$

which depends on the parameter T and the cutoff radius $R_c' = R_c\sqrt{\rho}$. Unfortunately, there is no obvious recurrence to compute higher order derivatives, but (lengthy) explicit formulae are readily derived. Nevertheless, since the explicit dependence on ρ is trivial, it is sufficient to be able to evaluate the bivariate function (R_c' and T) and its derivatives with respect to T to be able to evaluate the required four center integrals. An example higher order derivative is shown in 5.1. Here, a largely automatic approach is presented that yields an accurate and efficient procedure to evaluate representations of these bivariate functions. This approach can be used with general operators $g(r)$, even if no explicit recurrences are known or if the numerical evaluation is troublesome. For example, the procedure has also been tested on the Yukawa potential, for which Ten-no [104] skillfully derived a sequence of suitable expressions. Therefore, this technique might be useful for investigating density functionals that are based on a more flexible form of g(r).

In a first step, computer code for the explicit calculation of the function and all required derivatives is generated by a computer algebra system. This can be either an explicit expression, as obtained for the truncated Coulomb operator, a symbolic Taylor series [50], or any other convenient representation. Neither efficiency nor stability of the generated expression are a particular concern at this point. On a potentially large set of reference points, to be discussed below, this code is evaluated with arbitrary precision using a multi precision floating point library (`mpfr` [110, 111]). By doubling the number of digits employed in this evaluation until the result is accurate, a good numerical quality of the reference data is guaranteed. In order to evaluate accurately the higher derivatives of the TC operator, hundreds of

digits are essential for the intermediate expressions. Finally, an automatic piecewise bivariate interpolation of these reference points using Chebyshev polynomials is performed. This bivariate interpolation is constructed using the algorithm of Caliari et al. [112]. In this scheme, the full two dimensional parameter space has first to be mapped on the square $[-1,1]^2$, which is the natural domain for the interpolation. The function must also be defined on the boundary of the domain. In this square, the Padua2D points of order n are a special set of optimal nodes used for the polynomial interpolation,

$$\xi = (\xi_1, \xi_2) = \left\{ \gamma\left(\frac{k\pi}{n(n+1)}\right), \quad k = 0, ..., n(n+1) \right\}, \tag{5.24}$$

with the generating curve

$$\gamma(t) = \Big(-\cos((n+1)t), -\cos(nt) \Big), \quad t \in [0, \pi]. \tag{5.25}$$

The usage of these points guarantees an almost optimal convergence with increasing degree of the Chebyshev basis functions. The polynomial interpolation of a two dimensional function $f(x_1, x_2)$ is then given by

$$f(x_1, x_2) \approx \sum_{k=0}^{n} \sum_{j=0}^{k} c_{j,k-j} \hat{T}_j(x_1) \hat{T}_{k-j}(x_2) - \frac{c_{n,0}}{2} \hat{T}_n(x_1) \hat{T}_0(x_2), \tag{5.26}$$

where the coefficients

$$c_{j,k-j} = \sum_{\xi \in [1,1]^2} f(\xi) w_\xi \hat{T}(\xi_1) \hat{T}_{k-j}(\xi_2), \quad 0 \leq j \leq k \leq n \tag{5.27}$$

with weights w_ξ and Chebyshev polynomials $\hat{T}_m$ of order m can be computed once and for all and thus be stored in a table. Using the multi–precision enabled code, these coefficients are computed and stored in a standard 64–bit floating point representation. Function values of a bivariate function are then evaluated based on Eq. 5.26, and thanks to the favorable properties of the Chebyshev expansion, will be accurate to nearly machine precision, provided the expansion is of sufficient order. This also holds for the G_n functions required for the truncated Coulomb operator.

However, since the target function typically shows different behavior in terms of smoothness and continuity at different argument ranges, it is not beneficial to perform a global interpolation, as this requires a high order, and thus expensive, interpolation. Instead, an adaptive scheme has been devised, that, given a specified low order of the expansion, automatically bisects the full domain (e.g. using alternate directions), until the accuracy

of the interpolation is accurate to a given threshold (e.g. 10^{-12} or machine precision). This procedure is facilitated by the fact that the Padua2D interpolation procedure provides an automatic estimate of the accuracy [112]. As the procedure bisects the domain, computer code is generated such that the proper interpolation coefficients can be found efficiently in a table of patch–wise interpolating functions. In this way, evaluations of the interpolation can be performed orders of magnitude more efficiently than with the global interpolation. For the case of the truncated Coulomb operator, an interpolation order of 13 has been employed. The down-side is of course that the interpolation is only piece–wise contiguous, but nevertheless accurate to the chosen threshold everywhere. Note, that the interpolation is constructed for all derivatives simultaneously, i.e. Eq. 5.26 is never explicitely derived. In terms of efficiency, it can be concluded that calculating the starting vector G_n for the truncated potential is approximately twice as expensive as computing with an optimized implementation of the Γ–function the starting vector for the full Coulomb potential. The code for evaluating G_n for the truncated potential is available, as is the code for constructing the adaptive interpolation [113].

5.3 Assessment and validation of the method

5.3.1 Illustration on gas and condensed phase systems

In this section, the convergence behavior of the truncated operator for increasing cutoff radius R_c is investigated. As model systems, chains of polyethylene and poly-acetylene with a length of about 38 Å (30 Carbon atoms) have been chosen. For both systems, self consistent total energies have been calculated within the Hartree-Fock/pc-2 [114, 115, 116] level of theory applying the standard Coulomb operator, which serves as a reference, and with the truncated operator for different cutoff radii in the range of 0.1 to 15 Å. In order to illustrate the effect of the long-range correction, the same calculations have been performed again including the correction based on the PBE exchange hole. In addition, similar data for a two dimensional hexagonal boron-nitride mesh in periodic boundary conditions are presented. The latter system consists of 128 atoms in total, has a dimension of 20.1 x 17.4 Å and was computed with a pc-1 basis set [114, 115, 116]. The reference value has been obtained from an exponential extrapolation of the last three data points.

All findings are summarized in Fig. 5.2. In the case of the uncorrected TC operator, one observes that the total energy of all three systems decreases

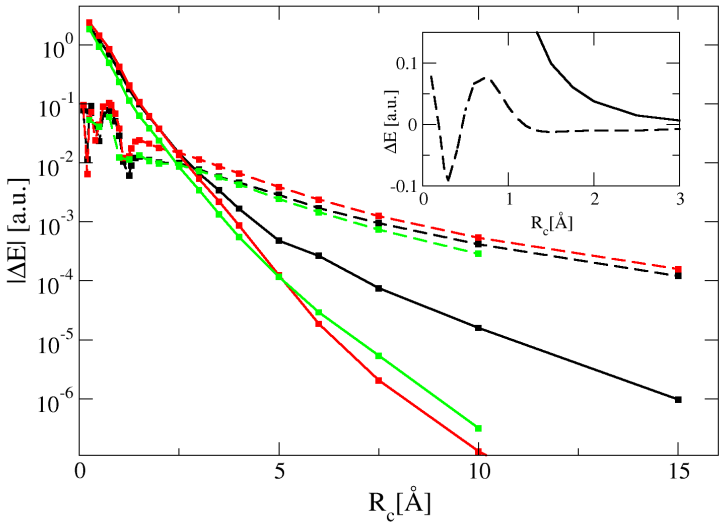

Figure 5.2: Shown are absolute errors in total energies with respect to the limiting case $R_c \to \infty$. Results for non-periodic poly-ethylene and poly-acetylene are drawn in red and black respectively while results for periodic hexagonal boron-nitride are displayed in green. Solid and dotted lines represent data obtained without and with the long-range correction. All errors are scaled by the number of non-hydrogen atoms in each system. As shown in the inset for poly-acetylene, the correction over- and underestimates the total energy at different ranges, which is the cause of the spikes in the logarithmic plot.

monotonically to the limiting value for increasing cutoff radius R_c. Furthermore, the logarithmic plot shows that all calculations converge approximately exponentially to the correct value. The faster convergence for poly-ethylene relative to poly-acetylene can directly be attributed to its larger band gap. The computed HF band gaps are 13.67 eV, 7.34 eV and 13.95 eV for poly-ethylene, poly-acetylene and the hexagonal boron-nitride mesh respectively. The long-range correction improves upon the uncorrected total energies in the short-range (0-2.5 Å) but overestimates the correction to the total energy in the long-range part. It is not so surprising that the LRC does not capture the tail of the exchange hole very well, since the underlying model is essentially derived to capture the short range behavior of the exchange hole. It appears that this model does not decay sufficiently fast. Very accurate

Hartree-Fock energies are thus obtained more easily without correction.

This analysis suggests that Hartree Fock exchange calculations with a truncated Coulomb potential could serve as an interesting tool for investigating the behavior of the exchange hole at different ranges, and could support the development of new density based exchange hole models.

5.3.2 Barrier heights and reaction energies for gas phase reactions

In order to analyze the accuracy of calculations based on the truncated Coulomb potential, the method has been benchmarked against a database established by Truhlar et al. [117]. This database consists of 22 reactions involving 47 molecules in gas phase, and provides geometries of reactants, products and saddle points. This database has been selected because reaction energies are particularly sensitive to the precise treatment of exchange, and because saddle point geometries usually involve somewhat de-localized electronic states. The dependence of the reaction energies and barriers heights on the choice of R_c for both the PBE0-TC and the PBE0-TC-LRC functionals has been investigated. In order to provide a reference, a comparison of these results to the established PBE [96], PBE0 [28, 29, 30], HSE06 [31, 32] and MCY3 [41] functionals are presented. In addition, all benchmark runs have been performed twice, once with an all–electron representation, and once applying pseudo–potentials. All–electron calculations employ the Gaussian and augmented plane waves (GAPW) method [15] and the MG3S basis[118], while pseudo–potential calculations use the Gaussian and plane waves (GPW) method [13], PBE optimized pseudo–potentials [119], and molecularly optimized TZV2P basis sets [92]. All results are summarized in Tab. 5.3. The first observation is that, as expected, the results of the standard PBE0 calculations are recovered as $R_c \to \infty$. Based on these results, the replacement of the standard HFX expression with its truncated counterpart seems to be possible without loss of accuracy if $R_c > 6.0$Å. As emphasized before, this is system dependent, but appears to hold for the (small) molecules in this test set. Interestingly, already for $R_c = 4.0$ Å, results obtained with either PBE0-TC and PBE0-TC-LRC are basically converged. If some small influence on the final results can be tolerated, a choice of R_c =4.0–6.0 Å appears appropriate, which can bring noticeable saving in computer time for large systems. PBE0-TC and PBE0-TC-LRC appear only significantly different at short-range $R_c \leq 2.5$ Å.

For the very short-range calculations ($R_c = 0.5$ Å), where only the PBE0-TC-LRC functional is meaningful, the calculations yield, as expected, ap-

	GAPW				GPW			
	barriers		energies		barriers		energies	
PBE	9.9		3.3		9.1		2.3	
PBE0	4.6		1.7		4.3		2.0	
HSE06	4.6		1.7		4.4		2.1	
MCY3	2.9		1.7		3.0		1.3	
R_c [Å]	TC	TC-LRC	TC	TC-LRC	TC	TC-LRC	TC	TC-LRC
∞	4.6	4.6	1.7	1.7	4.3	4.3	2.0	2.0
8.0	4.6	4.6	1.7	1.7	4.3	4.3	2.0	2.0
6.0	4.6	4.6	1.7	1.7	4.3	4.3	2.0	2.0
4.0	4.4	4.5	1.7	1.7	4.2	4.2	2.0	2.0
3.5	4.2	4.2	1.7	1.7	4.0	4.0	2.0	2.0
3.0	3.8	3.8	1.7	1.7	3.5	3.6	2.0	2.0
2.5	3.2	3.2	1.5	1.6	3.0	3.0	1.9	1.9
2.0	**2.7**	**2.6**	**1.4**	**1.4**	**2.5**	**2.5**	**2.0**	**1.9**
1.5	3.4	3.3	1.5	1.5	3.1	3.1	2.1	2.1
1.0	5.0	5.0	3.1	2.0	4.5	4.7	2.5	2.0
0.5	7.6	8.8	2.6	2.1	7.4	8.5	2.3	2.7

Table 5.3: The table shows mean square errors in kcal/mol of classical barrier heights and classical reaction energies with respect to experimental values. The data is shown for standard functionals PBE, PBE0, HSE06 and MCY3, and for the truncated Coulomb PBE0-TC and long-range corrected PBE0-TC-LRC functionals. For the latter two functionals, truncation radii (R_c) ranging from 0.5 Å to 8.0 Å have been employed. Calculations have been performed using an all–electron approach (GAPW) using a MG3S basis and pseudo-potentials (GPW) using a molecularly optimized TZV2P basis. Relative to experiment, the best results are obtained for $R_c = 2.0$Å, shown in bold.

proximately PBE results. It can be observed that in the intermediate range, around $R_c = 2.0$ the best estimates are obtained for the reaction barriers, similar in quality to MCY3. This suggests that the use of very short-range exchange functionals, such as PBE0-TC-LRC at $R_c = 2.0$ Å is meaningful, and that even more accurate functionals that explicitly limit the action of exact exchange to such a short distance can be developed.

5.3.3 Parallel performance

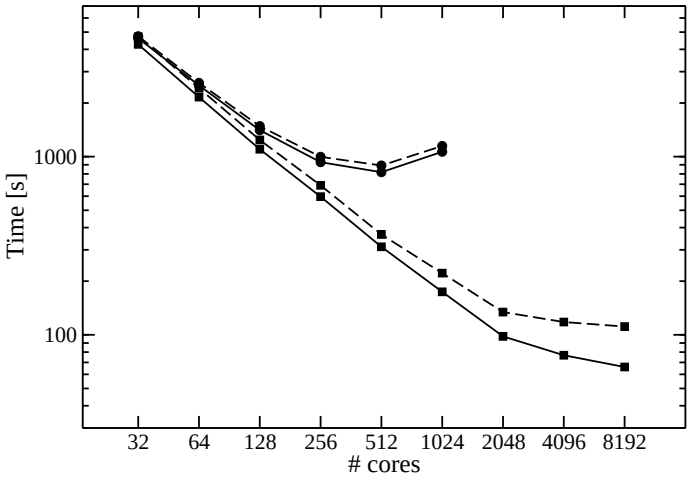

Figure 5.3: A comparison of the scaling of the current (diamonds) and previous (circles, Ref. [35]) implementation of periodic HFX. The benchmark is 10 steps of ab initio molecular dynamics of 64 water molecules in PBC using a TZV2P basis and pseudo potentials. The solid lines represent the time spent in the HFX routines, the dashed time is total run time. Using 2048 cores, successive Born-Oppenheimer MD steps take approximately 9s. All timings on a Cray XT5 with 8 cores per node.

Given the computational cost of simulations including exact exchange, an efficient and scalable implementation is essential if exact exchange is to be a successful ingredient for simulations of large and complex systems. The initial implementation presented in Ref. [35] scaled to a few hundreds of cores for a condensed phase system containing 64 water molecules, described with a TZV2P basis for both oxygen and hydrogen (2560 basis functions). Combined with the in-core compression scheme and a multiple-timestep approach, this was sufficient to compute 13 ps of MD trajectory. As shown in Fig. 5.3, the new implementation, using the PBE0-TC-LRC(R_c = 2.0) functional, allows the same system to scale up to a few thousands of cores, effectively allowing simulations to proceed ten times faster. Currently, 10 ps of simulation can be obtained in two days, even without a multiple-timestep scheme. As will be illustrated in Sec. 5.3.4, for systems that are computationally more demanding than 64 water molecules, scalability to 10'000s of cores

can be reached, effectively enabling CP2K [36] to obtain good performance on the largest supercomputers currently available.

The basic parallelization strategy has remained unchanged from the initial implementation, i.e. replicated density and Kohn-Sham matrices are made available on all MPI processes. Based on a load balancing step, the work of each process is decided in advance, and computation proceeds in a communication–free way until all local contributions to the Kohn-Sham matrix have been computed, and the matrix can be redistributed and summed. One key advantage of this approach is that full integral symmetry can be exploited. Furthermore, there are only communication steps in the beginning and in the end, and these can be performed efficiently in a ring topology. The disadvantage of this approach is that neither the communication nor the memory decreases as the number of processes increases. The memory bottleneck limits the size of the systems that can be studied, while the communication bottleneck ultimately limits scalability, provided load balance can be maintained throughout. However, the current implementation reduces the impact of the matrix replication by employing a mixed MPI/openMP scheme, where density and Kohn-Sham matrix are shared between the threads (one per core) on a node. In this way, the communication needed for the replication is reduced, and, depending on the available RAM, much larger systems (30000 basis functions and more for 16 Gigabytes per node) can fit in memory. A further benefit of the MPI/openMP scheme is that load balancing between threads can easily be performed. Such a dynamic load balancing is helpful for inhomogeneous systems that are difficult to load-balance before the calculations starts. Nevertheless, the importance of a good initial distribution of work can not be underestimated, and a carefully constructed load balancing algorithm is essential. The full description of this part of the algorithm is beyond the scope of the current paper. The basic ingredient is a binning procedure that collects batches of four center integrals of approximately equal estimated computational cost. These bins, typically 64 per core, are the basic unit of work and are distributed such that the computational load is balanced.

5.3.4 The cohesive energy of LiH at Hartree-Fock basis set limit

Recent HF and post-HF results on crystalline LiH [120, 121, 122, 123, 124] have received much interest in the solid state community. The availability of accurate reference numbers has made this system a challenging benchmark to judge the accuracy of various theoretical methods applied to condensed

phase systems. This work contributes to this ongoing research by computing the HF cohesive energy of LiH near the basis set limit. These results have been published in part in Ref. [123], where a comparison for the total energy of the LiH crystal obtained directly using the truncated method with results by Scuseria and co-workers based on extrapolation of screened exchange has been presented. Here, these results are summarized and some more details of these calculations are presented.

In a first step, an optimized basis set for an accurate HF calculation on bulk LiH, similar in composition to the polarization consistent (pc-3) basis sets derived by Jensen [114, 115, 116] has been constructed. The composition of this basis set is 8s3p2d1f/6s3p2d1f and 13s6p2d1f/11s5p2d1f for Hydrogen and Lithium (see Ref. [123] for details). The accuracy of the optimized basis has been estimated to be within 0.001 a.u. of the basis set limit for the total energy, while the basis set error on the cohesive energy is likely smaller than 0.1 %. All calculations, summarized in Tab. 5.4, have been performed on the experimental cubic unit cell with linear dimension $L = 4.084$ Å, which contains 4 Li and 4 H atoms, using truncated HF without the long-range correction. Total energies have been computed for systems of increasing system size by explicitely repeating this unit cell periodically in three dimensions. The largest system employed, a 5x5x5 repetition, consists of exactly 1000 atoms and uses 37500 Gaussian basis functions. With increasing system size the range of the truncated Coulomb operator has been increased as well. The results have been found to converge exponentially with system size, and an accurate estimate for the total energy per unit cell of approximately -32.258179 a.u. could be obtained directly from a calculation of the largest system. This number is in excellent agreement with the Padé-extrapolated SR-HFX results of Ref. [123], -32.258171 a.u.. By calculating the HF energy of the H atom and the Li atom in periodic boundary conditions and retaining the basis functions of all other (ghost) atoms in the unit cell, a consistent number for the cohesive energy could be obtained. However, due to the fact that unrestricted calculations are needed for the atoms, these calculations are more demanding (memory-wise) than the bulk and are therefore only performed for the 4x4x4 repetition of the basis cell. The 4x4x4 crystal required 11 Terabytes of memory for the integral storage. The best estimate of the cohesive energy obtained in this way is -131.949 mE_h. This result is derived in an extrapolation–free way, and is based on just three calculations (bulk LiH, and the atoms Li and H). It is in very good agreement with the best estimate reported by Gillan et al. [120], -131.95 mE_h. In order to investigate quantitatively the convergence of the energies with respect to R_c, systematic calculations of the HFX energies for the 5x5x5 unit cell, using a smaller basis set (adjusted pc-2 basis 4s2p1d/4s2p1d and 9s3p1d/9s3p1d

	R_c[Å]	E(HF)[a.u.]	H[a.u.](a)	Li[a.u.](b)	ϵ_{HF}^{coh}[a.u.]
2x2x2	4.0	-32.244609	-0.499957	-7.428493	-0.132702
3x3x3	6.0	-32.256844	-0.499974	-7.432137	-0.132100
4x4x4	8.0	-32.258022	-0.499974	-7.432582	-0.131949
5x5x5	10.0	-32.258179	N/A	N/A	N/A

Table 5.4: Results obtained with the truncated Coulomb operator and a large and flexible basis for unit cells that are a multiple of the basic cubic unit cell (4.084 Å). The columns show the size of the unit cell, the range of the truncated Coulomb operator (R_c), the Hartree-Fock energy per unit cell, the H atom energy, the Li atom energy, and the cohesive energy respectively (ϵ_{HF}^{coh}).

for hydrogen and lithium respectively, 19000 basis functions in total) have been performed. These results are presented in Tab. 5.5 and show that the cohesive energy is obtained with milli–Hartree accuracy for $R_c = 6$ Å, and micro–Hartree accuracy for $R_c = 10$ Å.

This system has also been used to measure the parallel efficiency of the implementation. Using the 3x3x3 repetition of the basic unit cell, consisting of 216 atoms and 8100 basis functions, calculations taking advantage of the hybrid `MPI/openMP` approach discussed above have been performed. The results for this setup, summarized in Fig. 5.4, show that this approach scales beyond 32'768 cores. The scaling is super-linear up to approximately 2048 cores, because the increasing amount of memory (2Gb/core) is used to store four center integrals, and successive SCF steps benefit from the in-core storage. The total amount of storage used for integrals exceeds 3 Terabytes in this case. For the runs on more than 16'384 cores, the impact of the communication becomes significant, and ultimately limits scalability. For this system, the load balance remains excellent and the local construction of the Fock matrix itself scales perfectly even at 65'536 cores.

5.3.5 The electronic structure of Rubredoxin

In order to demonstrate the ability of the truncated Coulomb method to compute large, inhomogeneous condensed phase systems with high quality basis sets, the electronic structure of a fully solvated Iron-Sulfur protein, Rubredoxin, in periodic boundary conditions, with a polarized triple zeta valence basis set [125] for all atoms, including hydrogen has been computed. In this setup, the system is described with 31247 basis functions, contains 2825

R_c[Å]	E(HF)[a.u.]	H[a.u.](a)	Li[a.u.](b)	ϵ_{HF}^{coh}[a.u.]
3	-32.231006	-0.498769	-7.405766	-0.153216
4	-32.242905	-0.499298	-7.423518	-0.137911
5	-32.246980	-0.499325	-7.429613	-0.132807
6	-32.247893	-0.499326	-7.431395	-0.131252
7	-32.248177	-0.499326	-7.431845	-0.130873
8	-32.248275	-0.499326	-7.431944	-0.130798
9	-32.248308	-0.499326	-7.431964	-0.130787
10	-32.248321	-0.499326	-7.431967	-0.130787

Table 5.5: HF results obtained with the truncated Coulomb operator for various values of R_c, without long-range correction. The 5x5x5 repetition of the basic cubic unit cell (4.084 Å) has been employed, together with a smaller basis set. The columns show the range of the truncated Coulomb operator (R_c), the Hartree-Fock energy per unit cell, the H atom energy, the Li atom energy, and the cohesive energy respectively (ϵ_{HF}^{coh}).

atoms and the unit cell has edges 31.136 x 28.095 x 30.502 Å^3. Due to the Iron-Sulfur active site, the multiplicity of the system is 6. The same system has been employed in earlier work with semi-local functionals to demonstrate the ability to compute ab initio free energy differences [126] and total energies near the basis set limit [92] for systems containing nearly 3000 atoms. A single point wavefunction optimization takes less than two hours, with about two thirds of the time spent in the Hartree-Fock exchange routines using 8196 cores of a CRAY XT5. The storage needed for the integrals is approximately 2.5 Terabytes, using a threshold of 10^{-8} for Schwarz screening and the in-core compression scheme described in Ref. [35] With this calculation, the difference in spin density distribution for the active site between a hybrid functional (B3LYP [26, 24, 27, 127]) with the TC operator ($R_c = 6.0$Å) and a semi-local functional (BLYP [23, 24]) has been investigated. The result of the calculation is illustrated in Fig. 5.5 where the difference in spin density between the GGA and the hybrid calculation are shown. Not unexpectedly, a more localized spin density is found with the hybrid functionals.

5.4 Conclusions

A new approach for Hartree-Fock calculations at the Γ–point using Gaussian basis functions has been presented. This approach is based on the trun-

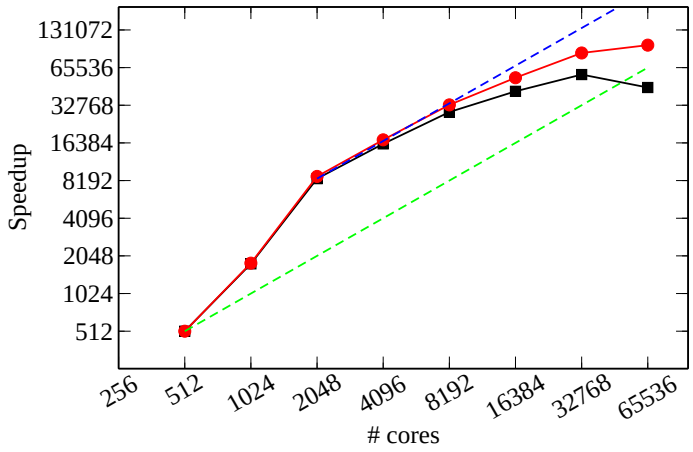

Figure 5.4: Shown is the speedup obtained from a computation of the 3x3x3 repetition of the basic unit cell of LiH (8100 basis functions). Black and red curves depict the observed speedups for the full calculation and for the Hartree-Fock part respectively. Dotted lines correspond to theoretical speedups assuming either an infinite amount of memory per node (blue) or the actually 16 Gb per node (green). All calculations have been performed using 8 threads per `MPI` process on a 8 core node (CRAY XT5).

cated Coulomb operator, and is demonstrated to be robust. With increasing truncation radius, results converge exponentially to the limiting Hartree-Fock values. Furthermore, a density functional based long-range correction to the truncated Coulomb operator has been derived. With this correction, very short-range exchange ($R_c = 2.0$ Å) yields excellent results for reaction energies and barrier heights. The finite range of the operator allows for efficient screening and can be exploited in a linear scaling implementation of exchange. The current implementation is massively parallel and allows for calculations on systems containing thousands of atoms and ten thousands of basis functions. These developments will enable simulations based on hybrid functionals that probe the rich chemistry and physics of large and complex condensed phase systems.

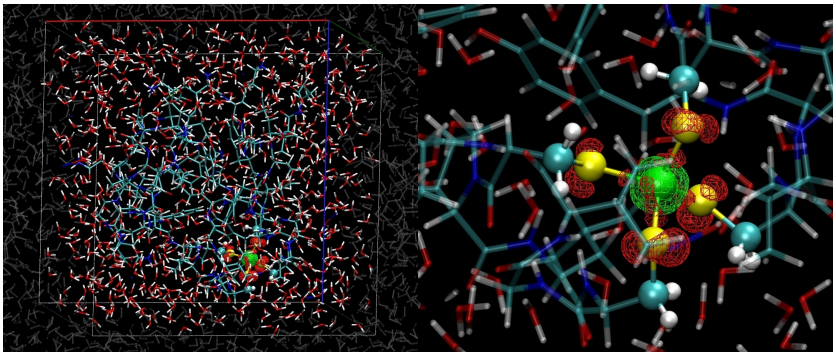

Figure 5.5: The left panel shows the unit cell of the solvated protein Rubredoxin, while the right panel focuses on its Iron-Sulfur active site. The contour shows the difference in spin density distribution between calculations performed with BLYP and B3LYP with the TC operator. Red indicates an excess in spin density with the local functional, while green indicates an excess with the hybrid functional. Clearly, the use of a hybrid functional favors localization of the spin density.

5.5 Appendix

5.5.1 Long-range correction

In this section, analytical expressions for the long-range part of the PBE exchange hole enhancement factor are presented in closed form for any given cutoff radius R_c. Indeed, based on $J_x^{\mathrm{PBE}}(s,y)$ as defined by Eq. 5.15 (see Ref. [109] for details, including definition of the quantities A–H), one finds that

$$F_x^{\mathrm{PBE,LRC}}(s) = -\frac{8}{9}\int_{R_c'}^{\infty} y J_x^{\mathrm{PBE}}(s,y)dy = -\frac{8}{9}\left(I_1 - I_2 + I_3 + I_4\right), \qquad (5.28)$$

where

$$I_1 = -\frac{A}{2}\exp\left(\frac{9}{4}\frac{s^2H}{A}\right)\mathrm{Ei}\left(-\frac{9}{4}\frac{s^2H}{A} - s^2HR_c'^2\right) \qquad (5.29)$$

$$I_2 = -\frac{A}{2}\mathrm{Ei}\left(-s^2HR_c'^2\right) \qquad (5.30)$$

$$I_3 = -\frac{A}{2}\mathrm{Ei}\left(-(D+s^2H)R_c'^2\right) \qquad (5.31)$$

$$I_4 = \alpha\left(\alpha_0 + \alpha_2R_c'^2 + \alpha_4R_c'^4\right)\exp\left(-R_c'^2\left(D + Hs^2\right)\right), \qquad (5.32)$$

with

$$\alpha = \frac{1}{2}\frac{1}{(D+s^2H)^3} \tag{5.33}$$

$$\begin{aligned}\alpha_0 &= 2E + DC + D^2B + s^2(HC + 2DHB + 2EG + DCF) \\ &+ s^4(H^2B + HCF)\end{aligned} \tag{5.34}$$

$$\begin{aligned}\alpha_2 &= D^2C + 2DE + s^2(2EH + 2DEG + 2DHC + D^2CF) \\ &+ s^4(2EGH + 2DHCF + CH^2) + s^6CFH^2\end{aligned} \tag{5.35}$$

$$\begin{aligned}\alpha_4 &= D^2E + s^2(D^2EG + 2DHE) \\ &+ s^4(2DHEG + EH^2) + s^6EGH^2\end{aligned} \tag{5.36}$$

and

$$R_c' = R_c k_F \tag{5.37}$$

k_F denoting the local Fermi vector. $\mathrm{Ei}(x)$ is the exponential integral and defined as

$$\mathrm{Ei}(x) = \int_{-\infty}^{x} \frac{e^t}{t} dt. \tag{5.38}$$

5.5.2 Stability criterion

In this section, the effect of thresholding and of the MIC on the stability of the SCF is analyzed. Starting from the exchange energy for a system containing N basis functions

$$E_x^{\mathrm{HF}} = -\frac{1}{2}\sum_{\mu\nu\lambda\sigma} P^{\mu\sigma}P^{\nu\lambda}\left(\mu\nu|\lambda\sigma\right)_g, \tag{5.39}$$

which can be rewritten in terms of matrix–vector products as the quadratic form

$$E_x^{\mathrm{HF}} = \mathbf{P}^T\mathbf{v}_{\mathrm{exact}}\mathbf{P}, \tag{5.40}$$

where $\mathbf{v}_{\mathrm{exact}}$ is a $N^2 \times N^2$ matrix containing all four center integrals and $\mathbf{P}$ is a vector of size N^2 with the density matrix elements. If screening is applied to the four center integrals using a given threshold ϵ, the above equation can be written as

$$E_x^{HF} = \mathbf{P}^T\mathbf{v}_{\mathrm{screened}}\mathbf{P} + \mathbf{P}^T\mathbf{v}_\epsilon\mathbf{P}, \tag{5.41}$$

where $\mathbf{v}_{\mathrm{screened}}$ collects all integrals that pass the screening, i.e. contributions that are larger than the threshold, and $\mathbf{v}_\epsilon$ is a matrix of error terms of order $\mathcal{O}(\epsilon)$ that are ignored throughout the calculation. For a reliable and stable optimization procedure, the maximum error introduced by ignoring $\mathbf{P}^T\mathbf{v}_\epsilon\mathbf{P}$ should be small.

In order to get an estimate for the maximum magnitude of the error, it is sufficient to obtain an estimate of the maximum eigenvalue of the $\mathbf{P}$ matrix, because

$$\mathbf{P}^T \mathbf{v}_\epsilon \mathbf{P} \leq \lambda^2_{\max}(\mathbf{P}) \mathcal{O}(\epsilon). \tag{5.42}$$

The above formula can be derived under the assumption that the largest eigenvalue of $\mathbf{v}_\epsilon$ is $\mathcal{O}(\epsilon)$. In the worst case, this eigenvalue could be $N^2\epsilon$, but is usually smaller ($\sim N\epsilon$).
Since $\mathbf{C^T S C} = \mathbf{1}$ with $\mathbf{C}$ being the matrix of the molecular orbitals and $\mathbf{S}$ the overlap matrix of the basis functions, the following upper bound for the norm of $\mathbf{C}$ can be obtained:

$$||\mathbf{C}|| \leq \frac{1}{\sqrt{\lambda_{\min}(\mathbf{S})}}. \tag{5.43}$$

Writing the density matrix $\mathbf{P}$ in terms of molecular orbitals, $\mathbf{P} = \mathbf{C C^T}$, one finds that

$$\lambda^2_{\max}(\mathbf{P}) \leq \frac{1}{\lambda^2_{\min}(\mathbf{S})}. \tag{5.44}$$

Finally, the above expression can be related to the condition number of the overlap matrix

$$\kappa(\mathbf{S}) = \frac{\lambda_{\max}(\mathbf{S})}{\lambda_{\min}(\mathbf{S})} \approx \frac{1}{\lambda_{\min}(\mathbf{S})}, \tag{5.45}$$

where the largest eigenvalue of $\mathbf{S}$ is assumed to be of order one. Based on these estimates one can conclude that the SCF calculations will be stable as long as

$$\epsilon \leq \mathcal{O}\left(\frac{1}{\kappa^2(\mathbf{S})}\right). \tag{5.46}$$

This stability estimate is usually too conservative but it does represent a worst–case scenario. On the other hand, as long as the SCF is stable, it is usually observed that $\lambda_{\max}(\mathbf{P}) \approx \mathcal{O}(1)$, which confirms that the error due to screening is typically ϵ per electron.

Finally, an analysis of the instability observed with the MIC algorithm is presented. Essentially, the MIC can be interpreted as a calculation with a truncated Coulomb potential using $R_c = L/2$, but with two sources of error in the computed four center integrals. The first source of error is due to the fact that only one term in the sum over $\mathbf{b}$ is retained, while the second source of error is due to the fact that these integrals are computed with the $1/r$ operator. These errors add an additional term $\mathbf{v}_{\text{MIC}}$ to the expression

$$E_x^{HF} = \mathbf{P}^T \mathbf{v}_{\text{screening}} \mathbf{P} + \mathbf{P}^T \mathbf{v}_\epsilon \mathbf{P} + \mathbf{P}^T \mathbf{v}_{\text{MIC}} \mathbf{P}, \tag{5.47}$$

which can not be controlled by the threshold ϵ. As before, the error related to $\mathbf{P}^T\mathbf{v}_{\mathrm{MIC}}\mathbf{P}$ might grow quickly as the condition number of the basis set becomes worse, explaining the stability of the algorithm with small and well conditioned basis sets, and its instability with large and flexible basis sets.

5.5.3 Efficient near- and far-field screening

Determining in advance which four center integrals are smaller than a given threshold, and can thus be ignored in the calculation, is important in an implementation of HFX that targets large systems. Indeed, screening reduces the number of integrals that need to be computed from $\mathcal{O}(N^4)$ to $\mathcal{O}(N)$. Two kinds of screening are commonly employed for the four center integrals, namely near- and far-field screening. Near–field screening [42] relies on the Schwarz-inequality and reduces the number of terms to $\mathcal{O}(N^2)$ also for calculations employing the $1/r$ operator, far–field screening only becomes really efficient [51] for operators $g(r)$ that decay faster than $1/r$, and reduces the number of required four center integrals to $\mathcal{O}(N)$. For systems with decaying density matrix (i.e. systems with an electronic gap), combining near–field screening with screening on the density matrix elements [48] also reduces the effort to $\mathcal{O}(N)$. A brute force implementation of the screening, as implemented in `CP2K` [36], is $\mathcal{O}(N^2)$. It is therefore important to reduce the pre-factor of this term as much as possible, and to have an efficient screening algorithm. An approach which is sufficiently efficient to deal with systems containing thousands of atoms without significant screening overhead is presented below.

For the near-field screening one can rely on the Cauchy-Schwarz inequality,

$$|(\mu\nu^{\mathbf{a}}|\lambda^{\mathbf{b}}\sigma^{\mathbf{b+c}})| \leq |(\mu\nu^{\mathbf{a}}|(\mu\nu^{\mathbf{a}})|^{\frac{1}{2}} \cdot |(\lambda\sigma^{\mathbf{c}}|\lambda\sigma^{\mathbf{c}})|^{\frac{1}{2}} \tag{5.48}$$

which only requires two center integrals. However, instead of storing or computing these two center integrals, it is very efficient to instead parametrize screening functions that are an upper bound to these integrals. These screening functions only depend parametrically on the interatomic distance $R_{\mu\nu}$ but are different for each type of Gaussian basis function (atom kind, shell, sets). These fits can be easily performed once one observes (see Fig. 5.6) that the logarithm of the integral is similar to a quadratic function at larger distance:

$$\log\Big((\mu\nu|\mu\nu)(R_{\mu\nu})\Big) \approx a_2 R_{\mu\nu}^2 + a_0. \tag{5.49}$$

This choice leads to the useful properties that the estimate decays monotonically with increasing distance, and that the expression only requires the square distance between the centers. The coefficients a_0 and a_2 are calculated

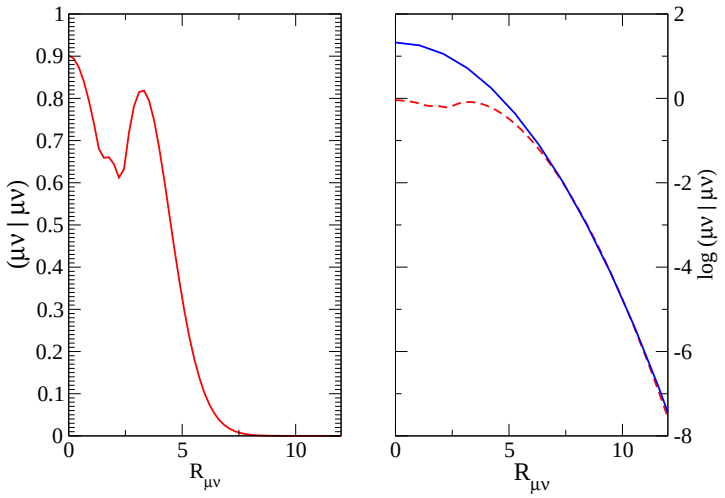

Figure 5.6: Shown are plots for $(\mu\nu|\mu\nu)$ as a function of the interatomic distance $R_{\mu\nu}$ for a lithium p-function and a hydrogen d function. The left panel shows the calculated values and on the right panel the logarithm of this data (dotted line) together with the fitting function (blue) is shown.

once and for all at the beginning of a calculation, minimizing an asymmetric penalty function

$$\sum_i k(\Delta_i)\Delta_i^2 \tag{5.50}$$

over a grid of suitably chosen values $R^i_{\mu\nu}$, with $\Delta_i = \log\Big((\mu\nu|\mu\nu)(R_{\mu\nu})\Big) - (a_2 R^2_{\mu\nu} + a_0)$, and $k(\Delta_i) = 1$ if $\Delta_i < 0$ and $k(\Delta_i) = 10000$ otherwise. This choice of k guarantees that $a_2 R^2_{\mu\nu} + a_0$ will be approximately an upper bound, and not merely a least square fit. Clearly, once the coefficients are determined, obtaining a Schwarz estimate of the integral is particularly fast.

The far–field screening is currently based on a rather crude estimate, which only flags if the integral will be smaller than a given threshold. For the truncated Coulomb operator this estimate can be obtained easily. It is based on the radii of the product densities of $R^\rho_{\mu\nu}$ for $\mu\nu^{\mathbf{a}}$ and $R^\rho_{\lambda\sigma}$ for $\lambda^{\mathbf{b}}\sigma^{\mathbf{b+c}}$, and cycles as soon as $R^\rho_{\mu\nu} + R^\rho_{\lambda\sigma} + R_c < |P - Q|$, where P and Q are the centers of the product densities. The radii $R^\rho_{\mu\nu}$ and $R^\rho_{\lambda\sigma}$ are similarly obtained from a two–parameter fit to precomputed values.

Chapter 6

Accurate Hartree-Fock energy of extended systems using large Gaussian basis sets [123]

Calculating highly accurate thermochemical properties of condensed matter via wave function-based approaches (such as *e.g.* Hartree-Fock or hybrid functionals) has recently attracted much interest. We here present two strategies providing accurate Hartree-Fock energies for solid LiH in a large Gaussian basis set and applying periodic boundary conditions. The total energies were obtained using two different approaches, namely a supercell evaluation of Hartree-Fock exchange using a truncated Coulomb operator and an extrapolation toward the full-range Hartree-Fock limit of a Padé fit to a series of short-range screened Hartree-Fock calculations. These two techniques agreed to significant precision. We also present the Hartree-Fock cohesive energy of LiH (converged to within sub-meV) at the experimental equilibrium volume as well as the Hartree-Fock equilibrium lattice constant and bulk modulus.

6.1 Introduction

The high accuracy/cost ratio of Kohn-Sham density functional theory [12, 128] (KS-DFT) has been exhaustively demonstrated in the literature. In its early days, KS-DFT using the local density approximation [12] was almost exclusively applied by the solid state community. However, the advent of generalized gradient approximations (GGAs, see *e.g.* Refs. [129, 130, 96]) to the exchange-correlation (XC) functional and the introduction of nonlocal Hartree-Fock (HF) exchange in hybrid functionals [131, 38] paved the way for reasonably accurate applications to molecules as well.

Within the framework of KS-DFT it is relatively easy to achieve basis set convergence, and atomic forces can be calculated at little extra computational cost. This is of paramount importance in the calculation of high-temperature dynamical and thermodynamic properties by molecular dynamics simulations. In particular, DFT statistical mechanics for both bulk materials and for surface processes is routinely feasible (see *e.g.* Ref. [132], and references therein). The principle limitation of KS-DFT lies in the accuracy of the applied XC functional.

Discussing examples for some shortcomings of KS-DFT, it is well known that standard local and semilocal approximations to the XC functional do not yield accurate results for quasiparticle band-gaps of semiconductors and insulators. Generally, they do not predict the correct adsorption sites and adsorption energies of molecules on metallic surfaces (for details see *e.g.* Ref. [133], and references therein). Today's DFT practitioner is confronted with these shortcomings when choosing an XC functional for a specific application. Each contemporary density functional has its relative merits but at the same time drawbacks, which might impede finding an appropriate XC functional. Different density functionals have different merits and demerits, an unsatisfactory situation. These inadequacies of semilocal KS-DFT have stimulated some DFT groups to use wave function-based methods to benchmark or correct DFT results. Note that other researchers are directly applying wave function-based techniques to materials science problems (see *e.g.* Ref. [134]) using the `CRYSTAL` code, but comparable assessments of the therein implemented HF method close to the basis set limit is still an open issue.

Dramatic improvements for many properties of molecules as well as solids can be achieved by mixing a fraction of nonlocal HF exchange (HFX) to the remaining part of semilocal DFT exchange. Since these functionals do not only depend on the electron density alone, but also on the KS single particle wave functions, *i.e.* the orbitals, they are called *hybrid* functionals. Therefore, these hybrid functionals can be seen as "mixed" wave function-based and semilocal DFT methods. We refer the reader to a recent review [135] of so-called screened hybrid functionals, as *e.g.* the Heyd-Scuseria-Ernzerhof [31, 32] (HSE) functional, which was proposed to extend the successes of hybrid functionals into condensed matter, by avoiding the problematic effects of long-range HFX (see Ref. [135], and references therein).

Besides the successes of screened HFX applied to condensed matter, the numerous methodological and algorithmic developments in the quantum-chemistry community and the steady increase of computers' efficiency induced a drive to conceive and implement even more involved wave function-based techniques, as *e.g.* local second-order Møller-Plesset perturbation theory (MP2) [136, 137, 138], (resolution of the identity) atomic orbital Laplace

transformed MP2 [139, 140, 141] and canonical MP2 [142, 122] for (infinitely) extended systems of various dimensionality and applied basis functions. Furthermore, recent reports in the literature on *ab initio* molecular dynamics on condensed matter [35] employing the HSE screened hybrid functional illustrate that, depending on implementation details, basis set and system, wave function-based techniques are also applicable to statistical mechanics calculations. These successful applications of wave function methods to large systems show that they are able to tackle materials science problems with possibly much better accuracy than conventional density functionals.

Recently published HF and post-HF calculations on crystalline LiH have attracted much interest in the solid state community [121, 120, 124]. These calculations represent a benchmark in terms of eliminating as many inaccuracies as possible while attempting to converge toward the so-called HF limit. The approach in question employs calculations on a hierarchical series of cluster models [121, 124], exploiting strengths and weaknesses of plane wave pseudopotentials as well as local Gaussian basis sets. Accurate evaluation of the total HF energy, as well as cohesive energy in the HF approximation employing exclusively Gaussian basis sets is desirable to bypass errors incurred by the pseudopotential approximation. Admittedly, creating an all-electron Gaussian basis set, which describes the crystal as well as the isolated atoms equally well, is challenging. Referring to the arguments of Gillan *et al.*, [120] it is in general difficult to provide rigorous estimates how far the applied basis set is from the HF limit. However, it is reasonable to question the need for reaching the HF limit for particular materials properties, which is substantiated in the present work.

We compare total HF energies of solid LiH using two different codes employing Gaussian basis functions: (i) the Gaussian and augmented-plane wave (GAPW) [13] code `CP2K/Quickstep` [14, 36] and (ii) a developmental version of the `GAUSSIAN` suite of programs [143]. We show that the cohesive energy of the crystal is converged to within sub-meV accuracy in our given large Gaussian basis set (see Tab. 6.1). Computational and methodological details are presented in Sec. 6.2. Results for cohesive energies, theoretical lattice constant as well as bulk modulus are in Sec. 6.3. Conclusions are drawn in Sec. 6.4.

6.2 Computational details

In the following sections, we describe important computational details, such as the Gaussian basis set, the evaluation of full-range HFX based on the short-range (SR) HFX implementation [51] in the `GAUSSIAN` suite of pro-

grams as well as the method applied for the extrapolation of the SR-HFX energy to the full range limit based on Padé approximants. Furthermore, implementation details on the direct evaluation of HFX via the `CP2K/Quickstep` code are presented.

6.2.1 Basis set

The basis set used for this calculation has been specifically constructed for the current purpose, which is an accurate but computationally feasible HF calculation on bulk LiH. The basis constructed here is similar to the polarization consistent (pc) basis sets derived by Jensen [114, 115, 116]. Jensen introduced a sequence of quasi-optimal basis sets (pc-[0-4]) that rapidly converge to the HF and DFT basis set limit. The pc-3 basis set gives atomization energies with a mean error smaller than 1 kJ/mol. For H and Li the pc-3 basis set has a composition 9s4p2d1f/5s4p2d1f and 14s6p2d1f/6s3p2d1f respectively, while we adopt 8s3p2d1f/6s3p2d1f and 13s6p2d1f/11s5p2d1f. However, the primitives of the basis employed here are non-standard and optimized for the present calculations.

In a first step, we have removed primitive Gaussians with exponents smaller than 0.15 bohr^{-2}, since diffuse basis functions are technically troublesome. Diffuse functions, which are needed to describe density tails in atoms or molecules, are not needed in the bulk of densely-packed solids with large band gaps as the case of LiH. Indeed, we exploit the fact that the basis functions on the lattice sites are available for the expansion of any orbitals, be it the crystal orbitals in the bulk or the atomic orbitals of the isolated atoms. This basis is thus only suited for atomic or surface calculations if ghost basis functions are left in the regular lattice positions to appropriately describe the aforementioned tails of the electron density.

In a second step, all but the core exponents have been optimized by minimizing the energy of bulk LiH subject to a restraint on the condition number of the overlap matrix. This procedure is similar to the one employed for the molecularly optimized basis sets described in Ref. [92]. In `CP2K`, density functionals that do not include Hartree-Fock exchange can be computed in a highly efficient manner, and in order to make this procedure computationally efficient, such a semilocal density functional (B88 [23]) has been employed in the optimization process. The resulting basis is well conditioned, the condition number of the overlap matrix is 2.8×10^4 for bulk LiH. We have estimated the accuracy of the optimized basis by comparing to pc-4-like basis sets, which for this system are only feasible with local DFT, and estimate the total energy of bulk LiH (per unit of LiH) to be well within 0.001 a.u. of the basis set limit, while the basis set error on the cohesive energy is likely

smaller than 0.1% (0.0001 a.u.). The details of this optimized basis set are summarized in Tab. 6.1.

species	l	exponent	coefficient	species	l	exponent	coefficient
H	s	0.27463675e02	1.00000000	Li	s	0.13360341e04	1.00000000
	s	0.68559258e01	1.00000000		s	0.44429982e03	1.00000000
	s	0.17679972e01	1.00000000		s	0.14779702e03	1.00000000
	s	0.51181842e00	1.00000000		s	0.49209451e02	1.00000000
	s	0.20167548e00	1.00000000		s	0.16428957e02	1.00000000
	s	0.30797000e04	0.00023473		s	0.55293994e01	1.00000000
		0.46152000e03	0.00182450		s	0.19052824e01	1.00000000
		0.10506000e03	0.00959330		s	0.70025874e00	1.00000000
	p	0.21240865e01	1.00000000		s	0.29958682e00	1.00000000
	p	0.10736812e01	1.00000000		s	0.16636288e00	1.00000000
	p	0.56838662e00	1.00000000		s	0.70681000e05	0.00000544
	d	0.92833840e00	1.00000000			0.13594000e05	0.00003328
	d	0.49583000e00	1.00000000			0.31004000e04	0.00019175
	f	0.12073480e01	1.00000000		p	0.15709110e01	1.00000000
					p	0.74875864e00	1.00000000
					p	0.38614089e00	1.00000000
					p	0.22620503e00	1.00000000
					p	0.28500000e02	0.00036754
						0.66400000e01	0.00322359
					d	0.77920820e00	1.00000000
					d	0.40789925e00	1.00000000
					f	0.73706300e00	1.00000000

Table 6.1: Details for the adopted basis sets for the compositions 8s3p2d1f/6s3p2d1f and 13s6p2d1f/11s5p2d1f of Hydrogen and Lithium respectively. Shown are angular momentum, Gaussian exponent and corresponding contraction coefficients.

6.2.2 Extrapolation of SR-HFX to full range (GAUSSIAN)

All Gaussian calculations presented in this work are based on a very efficient implementation of the SR-HFX energy exploiting a distance based screening protocol [51]. Using local basis functions it is convenient to express the HFX

energy for closed-shell as

$$E_x^{\mathrm{HF}} = -\frac{1}{2}\sum_{\mu\nu\lambda\sigma} P_{\mu\lambda}P_{\nu\sigma}(\mu\nu|\lambda\sigma)_g, \tag{6.1}$$

where $P_{\mu\nu}$ are density matrix elements and

$$(\mu\nu|\lambda\sigma)_g = \int \mu(\mathbf{r}_1)\nu(\mathbf{r}_1)g(r_{12})\lambda(\mathbf{r}_2)\sigma(\mathbf{r}_2)\, d\mathbf{r}_1 d\mathbf{r}_2 \tag{6.2}$$

are the four-center electron repulsion integrals (ERIs), represented in an atomic orbital basis. The applied interaction potential $g(r_{12})$ is usually equal to the Coulomb kernel $\frac{1}{r_{12}}$.

For large gap systems, it has been shown that local single particle wave functions as well as the corresponding density matrix decay like $e^{-h|\mathbf{r}_1-\mathbf{r}_2|}$ for large $|\mathbf{r}_1-\mathbf{r}_2|$, where h is proportional to $\sqrt{\mathrm{E}_{\mathrm{gap}}}$, the square-root of the band gap of the system of question [144, 145, 43, 44]. This is the basic motivation behind SR-HF as *e.g.* used in the successful HSE hybrid functional [31, 32]. HSE is based on a screened Coulomb interaction $g(r_{12})$ splitting the conventional Coulomb kernel, $\frac{1}{r_{12}}$, into

$$\frac{1}{r_{12}} = \underbrace{\frac{\mathrm{erfc}(\omega\, r_{12})}{r_{12}}}_{\mathrm{SR}} + \underbrace{\frac{\mathrm{erf}(\omega\, r_{12})}{r_{12}}}_{\mathrm{LR}}, \tag{6.3}$$

where the long-range (LR) and short-range (SR) parts of the interaction are described by the computationally convenient error function and its complement, respectively. The parameter ω in Eq. 6.3 determines the extent of the range separation of the Coulomb interaction.

In view of the relatively large HF band gap of LiH (10.8 eV) [146] and the fast decay of the density matrix, we will calculate the total HF energy by doing a series of SR-HF calculations at different ω, and extrapolating to $\omega \to 0$. As corroborated by numerical results shown in Sec. 6.3, such an extrapolation of the screened HF energies of the crystal to the full-range HF limit in the specified basis set is numerically robust and reliable.

All calculations are based on a locally modified development version of the `GAUSSIAN` electronic structure program [143]. Hence, the total energies presented in Sec. 6.3 do not include any DFT contributions. Only Hartree and screened HFX energies are evaluated. The RMS convergence criterion for the density matrix in the self-consistent-field (SCF) iteration was set to 10^{-7} a.u., which implies an energy convergence no worse than at least 10^{-8} a.u. (`GAUSSIAN` keyword: SCF=Tight). Furthermore, a $24 \times 24 \times 24$

mesh of k points was used, which is equivalent to 6912 k points and thus all calculations are sufficiently converged with respect to k points. The large band gap of LiH in the HF approximation (see above) substantially helps converging the k-point integration.

Following ideas found in the literature [147, 148], we apply Padé approximants of various orders to the obtained series of screened HF energies. The actual form of the Padé approximants are the rational polynomials

$$\frac{p(x)}{q(x)} = \frac{\sum_{i=0}^{n} p_i \, x^i}{\sum_{j=0}^{m} q_j \, x^j}. \tag{6.4}$$

Eq. 6.4 represents the general expression of a Padé approximant of order $[n/m]$. Throughout this work only *diagonal* rational polynomials are applied [147, 149], which means that the order of the polynomial in the numerator equals the order of the polynomial in the denominator. Note that the number of parameters to be fitted is $2n + 1$ in the case of diagonal polynomials. This is the minimum number of data points, which must be included in the least-squares fit.

For all extrapolations employed in the present work, ω has been chosen to lie in the interval $[0.04\,;\,1.0]$. In order to put a higher weight to the area near to full-range HF we decided to increment ω by 0.005 up to 0.1 and increment ω by 0.01 up to a value that amounts to 0.2. For the remaining interval of larger ω values, the screening parameter was incremented by 0.1. As a consequence, each fit is based on 31 data points, representing pairs of the screening parameter ω and the corresponding SR-HF energy.

The HF equilibrium lattice constant and bulk modulus have been obtained by fitting the volume dependence of the static lattice energy to the Murnaghan equation of state [150]. The points were chosen in order to cover a range of $\pm 3\%$ around the supposed equilibrium lattice constant of 4.108 Å (seven-points-fit).

6.2.3 HFX and periodic boundary conditions using Gaussian basis functions

In hybrid functionals, which incorporate a fraction of nonlocal HFX (Eq. 6.1), the decay of the Hamiltonian matrix elements (see Sec. II of Ref. [16]) with distance is determined by two factors: (i) the decay behavior of the density matrix, $P_{\mu\nu}$, and (ii) the decay behavior of the ERIs. For metallic as well as insulating systems, a screened Coulomb interaction accelerates the convergence of the ERIs in real-space drastically, *i.e.*, the number of replica cells needed for convergence is substantially decreased (see Refs. [151] and [152]).

Fock exchange calculations involving the long-range tail of the Coulomb interaction (*e.g.* in the $\omega \to 0$ limit, see Eq. 6.3, in long-range corrected hybrids or in global hybrids), both the density matrix and the ERIs influence the convergence of the HFX energy.

It is a matter of fact, that due to the algebraic structure of Eq. 6.1, contributions to the HFX energy can be significant even far from the central cell, precluding an early truncation of the lattice sum (see Eq. 2.4 in Ref. [16]). Small exponent basis functions involved in the calculation of the density matrix become important factors determining the computational workload. Calculations under periodic boundary conditions (PBC) involving SR-HFX with a reasonably large value for the screening parameter ω (Eq. 6.3) are tractable for moderately diffuse Gaussian basis functions, *i.e.* minimal exponent equals $\approx$0.2. Conventional HF or long-range HF calculations are likely to be computationally prohibitive except for high-exponent Gaussian basis sets. The relatively large and diffuse basis set used in this work (see Tab. 6.1) prevents calculating the HFX at or close to $\omega = 0$, *i.e.* the long-range limit for this particular system in the given basis. As shown by the results presented in Sec. 6.3, a numerically stable fit to a sufficiently large series of SR-HFX calculations is practicable to calculate an accurate estimate for the HF energy of extended (insulating) systems using large Gaussian basis sets. In summary, $\omega = 0$ is not practical whereas a 31 point ω extrapolation works very well.

6.2.4 Direct calculation of HFX (`CP2K`)

The focus of `CP2K` is the simulation of complex systems, with a variety of methods. Recently, the capability to perform first principles molecular dynamics simulation with density functionals including a fraction of Hartree-Fock exchange has been implemented and demonstrated for condensed phase systems containing a few hundred atoms [35]. With this goal in mind, the implementation is massively parallel, focuses on in-core calculations, uses the Γ point only, and does not exploit molecular or crystal symmetries. The implementation was based on a minimum image (MI) convention [102] and employed a standard 1/r Coulomb operator. The current implementation, which will be described in detail elsewhere [95], goes beyond the minimum image convention, and instead employs a truncated Coulomb operator which is defined as

$$g(r_{12}) = \begin{cases} \frac{1}{r_{12}}, & r_{12} \leq R_c \\ 0, & r_{12} > R_c. \end{cases} \tag{6.5}$$

This operator was suggested by Spencer and Alavi [103] to obtain rapid convergence for the Hartree-Fock energy with respect to the k-point sampling of the exchange energy in periodic systems. Note that the use of the truncated Coulomb operator implies that the exchange energy is unconditionally convergent for all k points. Furthermore, since exchange in insulators is effective on shorter range compared to the electrostatic interaction, results converge exponentially to the Hartree-Fock limit as R_c is increased. In line with the results presented in Ref. [103], we find that for a cubic cell with edge L and $R_c = L/2$, converged results of the exchange energy can be obtained using the Γ point only. Of course, this requires that the computational cell is sufficiently large so that the Γ-point approximation is acceptable, which in turn requires that the extent of the maximally localized Wannier functions is smaller than $L/2$. Consequently, the exchange energy computed in `CP2K` is defined as

$$-\frac{1}{2}\sum_{i,j}\int\int \psi_i(r)\psi_j(r)g(|r-r'|)\psi_i(r')\psi_j(r')\,d^3r d^3r', \tag{6.6}$$

where ψ_i are the wave functions at the Γ point. In the Gaussian basis set employed, the exchange energy per cell is thus obtained from

$$-\frac{1}{2}\sum_{\mu\nu\gamma\delta}\sum_{\mathbf{abc}} P^{\mu\gamma}P^{\nu\delta}(\mu\nu^{\mathbf{a}}|\gamma^{\mathbf{b}}\delta^{\mathbf{b+c}})_g, \tag{6.7}$$

where μ,ν,γ,δ are the indices of the basis functions in the central cell, and $\mathbf{a},\mathbf{b},\mathbf{c}$ run over all image cells. Due to the rapid decay of the basis functions, sums over image cells $\mathbf{a}$ and $\mathbf{c}$ converge quickly. The sum over $\mathbf{b}$ converges quickly and unconditionally for our choice of $g(r_{12})$. Further technical details, including how to compute efficiently and accurately the required four center integrals $(\mu\nu^{\mathbf{a}}|\gamma^{\mathbf{b}}\delta^{\mathbf{b+c}})_g$ will be presented elsewhere [95].

6.3 Results

6.3.1 HF energy of LiH at experimental volume using Padé approximants

Fig. 6.1 depicts the obtained series of 31 data points of screened HF energies for various values of $\omega \in [0.040\,;\,1.0]$ (see Sec. 6.2) calculated at the experimental lattice parameter. The series of calculated energies clearly converges to a certain limit with decreasing ω. At this point we remind the reader that for the limit $\omega \to 0$ the SR Coulomb kernel given in Eq. 6.3

approaches the full-range $1/r$ operator. As shown in Fig. 6.1 and outlined in Sec. 6.2, the density of data points increases significantly toward the $\omega \to 0$ limit. Tab. 6.2 presents results for several least-squares fits obtained using rational polynomials up to order seven. In addition, correlation coefficient r, root-mean-square-deviation (RMSD) as well as relative RMSD, which is normalized to the range of observed data, *i.e.* calculated energies, are shown. Since r is very close to 1, we decided to present in Tab. 6.2 $(1 - r)$, where a value of zero means perfect agreement between calculated data points and fit.

Apparently, the RMSD as well as relative RMSD values decrease with increasing order of the rational polynomial applied to the fit. Rational polynomials of order eight or beyond (not shown in Tab. 6.2) lead to unstable fits and the goodness of the fit deteriorates. According to Tab. 6.2 the optimal order of the Padé approximant is [7/7], which was used for all extrapolations employed in this work.

Fit	(1-r)[a]	RMSD[b]	RMSD%[c]	E(HF) [a.u.]
[1/1]	6.7e-05	0.0185955	0.3654035	-32.3526129
[2/2]	5.7e-08	0.0005666	0.0111347	-32.2472782
[3/3]	5.5e-07	0.0018244	0.0358500	-32.2521383
[4/4]	2.0e-10	0.0000364	0.0007156	-32.2585728
[5/5]	7.9e-10	0.0000759	0.0014909	-32.2588628
[6/6]	1.5e-09	0.0001109	0.0021803	-32.2576031
[7/7]	6.2e-15	0.0000002	0.0000046	-32.2581712

[a] r: correlation coefficient (see text for details).
[b] RMSD: root mean square deviation.
[c] RMSD%: normalized root mean square deviation.

Table 6.2: Results for the Padé fits to the 31 SR-HF energies [a.u.] of LiH at experimental lattice constant (4.084 Å) for a cell containing four LiH ion pairs. The first column shows the order of the Padé polynomials representing them by the order of the polynomial of the numerator and denominator, respectively (in squared brackets). The extrapolated total HF energy for the cell is given in Hartree atomic units.

As a next step we had to validate the [7/7] polynomial, since it is well known, that algorithms for interpolation are straightforward, whereas for extrapolation care must be taken. A plausible strategy is simply the prediction of energies for a certain value of ω not included in the fit. Table 6.3 shows a

#dp	ω	E^{SR-HF} [a.u.]	E^{fit} [a.u.]	Error	%-Error
24	0.070	-31.630779	-31.630965	-0.0001817	0.000574
25	0.065	-31.675185	-31.675183	0.0000010	-0.000003
26	0.060	-31.719533	-31.719533	0.0000003	-0.000001
27	0.055	-31.763998	-31.763998	0.0000003	-0.000001
28	0.050	-31.808571	-31.808571	0.0000003	-0.000001
29	0.045	-31.853244	-31.853244	0.0000003	-0.000001
30	0.040	-31.898007	-31.898007	0.0000004	-0.000001

Table 6.3: Validation of the [7/7] Padé fit. The first column gives the number of data points (*i.e.* SR-HF energies) included for a [7/7] Padé fit in order to predict the SR-HF energy corresponding to the ω value given in the second column. Deviations between calculated and fitted SR-HF energies are given in the fifth and sixth column, respectively.

series of predictions for screened HF energies for a series of ω's starting from $\omega = 0.070$ a.u.$^{-1}$. The corresponding screened HF energy has been estimated based on a [7/7] fit using 24 data points, where $\omega \in [0.075\,;\,1.0]$. As can be seen from Tab. 6.3, it is remarkable that the resulting error is only one order of magnitude larger than the applied SCF convergence criterion (see Sec. 6.2). The error for the predicted energies is practically converged after inclusion of only one further data point and amounts to 3×10^{-7} a.u.. Hence, the error incurred by the fit to the Padé approximant is much lower than the convergence threshold in the SCF procedure. By virtue of the aforementioned validations it is safe to give the total HF energy for a unit cell containing four LiH ion pairs at experimental lattice constant (4.084 Å) with a precision of five decimals in Hartree atomic units, which amounts to -32.25817 a.u.. The total HF energy per formula unit at experimental lattice constant is given in Tab. 6.4 and compared with the HF energy obtained using `CP2K`. Both values agree excellently to significant precision.

6.3.2 HF lattice constant and bulk modulus with `GAUSSIAN`

Fig. 6.2 shows the seven-points-fit of the obtained Padé extrapolated HF energies to the Murnaghan equation of state as outlined in Sec. 6.2.2. The RMSD value of this fit amounts to 1.4×10^{-4}. The resulting HF equilibrium lattice constant of LiH equals 4.105 Å and is in excellent agreement with

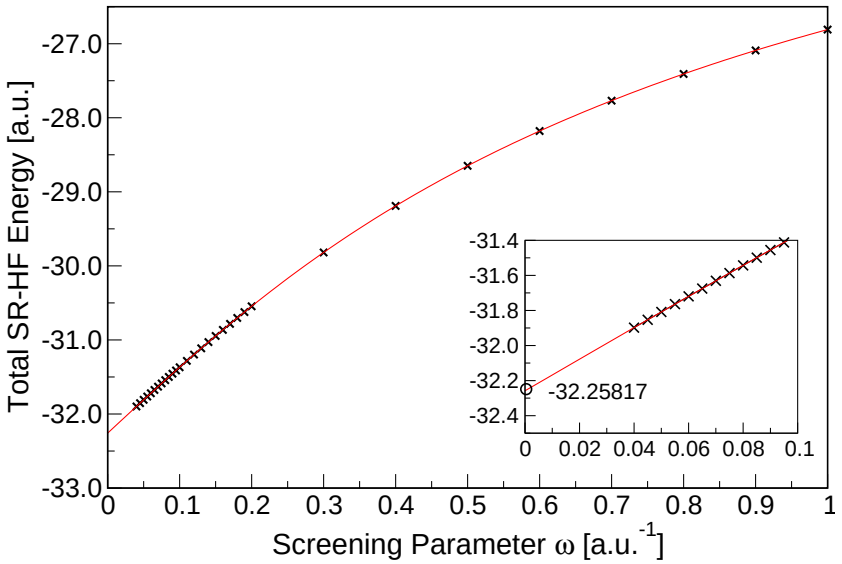

Figure 6.1: (Color online) Convergence of the SR-HF energy [a.u.] of a LiH unit cell containing four LiH ion pairs at experimental lattice constant (4.084 Å) with decreasing screening parameter ω involved in the short-range Coulomb interaction. Gaussian results for each ω are represented by crosses. The line shows the [7/7] Padé fit to the numerical data (see text for details). The inset gives SR-HF energies for $\omega \in [0\,;0.1]$ a.u.$^{-1}$ as well as the extrapolated value for $\omega = 0$ in Hartree atomic units.

the result obtained by Gillan *et al.* (see Tab. 6.4). The corresponding bulk modulus of LiH amounts to 32.34 GPa, which is again in very good agreement (0.9% deviation) with the results obtained by aforementioned workers. Note that bulk moduli are quite sensitive to the equilibrium volume at which they are evaluated and overall good indicators for the quality of the underlying energies at the various volumes.

6.3.3 Total and cohesive energy at experimental volume with `CP2K`

Total energies have been computed for systems of increasing system size by explicitly repeating the cubic unit cell periodically in three dimensions. The largest cell employed is a $5 \times 5 \times 5$ repetition of the basic cubic cell, and contains exactly 1000 atoms. For this system, 37500 Gaussian basis functions are used for the expansion of the molecular orbitals, which makes this a computationally demanding simulation. With increasing system size, we also

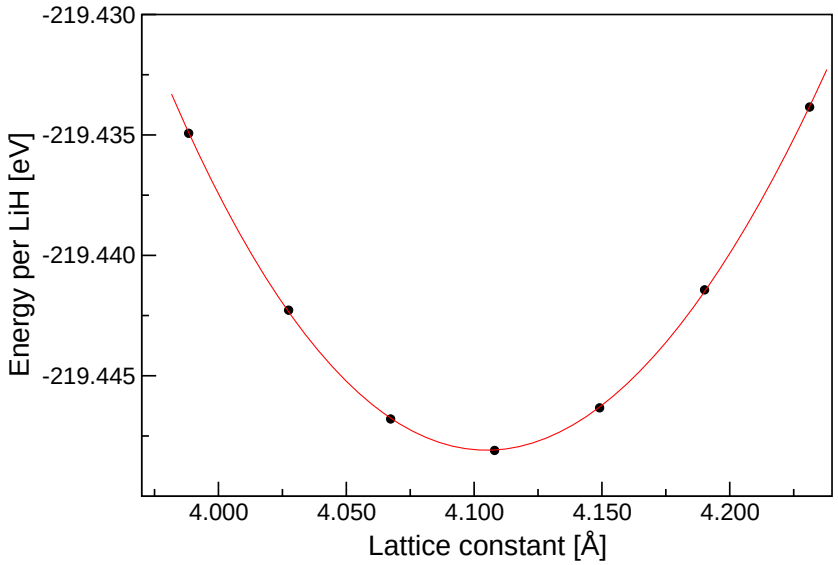

Figure 6.2: (Color online) Murnaghan equation of state (red/gray line) for LiH obtained using the HF approximation. Each of the seven points corresponds to the extrapolated least-squares fit of 31 screened HF energies to a Padé approximant of order [7/7] (see text for details).

increase the range of the truncated Coulomb operator, in steps of 2 Å up to a maximum of 10 Å (see Tab. 6.5). The Γ-point approximation therefore converges quickly (exponentially) to the HF limit of this system. We thus obtain from a direct calculation, without extrapolation, an accurate estimate of the total energy per unit cell of approximately -32.258179 a.u.. The finite size error on this result is estimated to be smaller than 50 μE_h. Furthermore, this number is in excellent agreement with the Padé-extrapolated SR-HF results (-32.258171 a.u., Tab. 6.2), and thus provides numerical evidence for the quality of both approaches. Calculating the HF energy of the H atom and the Li atom with the current basis set, in periodic boundary conditions and retaining the basis functions of all other atoms in the unit cell, we can obtain a consistent estimate of the cohesive energy. In our approach, due to the fact that unrestricted calculations are needed for the atoms, these calculations are even more demanding than the bulk, and have only been performed up to a $4 \times 4 \times 4$ repetition of the basis unit cell. Our best estimate for the cohesive energy, obtained from just three calculations (bulk LiH, and the atoms Li, H) without extrapolation, is -131.949 mE_h. Also here, the finite size error is estimated to be smaller than 50 μE_h. This number is in excellent agreement with the best estimate obtained by Gillan et al. [120] -131.95 mE_h.

	E(HF) [E_h]	$\varepsilon_{\mathrm{HF}}^{\mathrm{coh}}$ [mE_h]	a_0 [Å]	B [GPa]
GAUSSIAN	-8.064543[a]		4.105	32.34
CP2K	-8.064545[a]	-131.949[a]		
CRYSTAL[b]		-129.14	4.121	28.3
CRYSTAL[c]		-130.16		
VASP[d]		-131.7[a]		
Gillan *et al.*[e]		-131.95[a]		
Gillan *et al.*[e]		-131.99	4.108	32.05

[a] calculated at experimental lattice constant (4.084 Å).
[b] Ref. [138]. [c] Ref. [153]. [d] Ref. [122]. [e] Ref. [120].

Table 6.4: Summary of total HF energies per formula unit, HF cohesive energies, equilibrium lattice constants and bulk moduli of LiH obtained using GAUSSIAN and CP2K. For comparison purpose, results found in the literature are included.

It is noteworthy to comment on the calculated HF cohesive energies of LiH obtained using the CRYSTAL code (see Tab. 6.4). As already mentioned in the introduction, an assessment of the HF method implemented in CRYSTAL close to the basis set limit has not been published yet. However, in view of the fact that all cohesive energies of LiH obtained using CRYSTAL are above the correct value, it appears that the Gaussian basis sets used for the cohesive energy calculations in Refs. [153] and [138] are too restricted to obtain a comparable high level of accuracy to the one pursued in the present work. A comment in Sec. 3.1 of Ref. [138] makes it appear unlikely that calculations close to the HF limit will be feasible using the current CRYSTAL code.

6.4 Conclusions

The Hartree-Fock energy of solid LiH has been calculated using large Gaussian basis sets. Two different approaches, extrapolation of a Padé fit to a series of SR-HFX calculations and direct calculation using a truncated Coulomb operator, have been found to yield total energies that agree to better than 0.1 mE_h. Calculations of the cohesive energy, the equilibrium lattice constant and the bulk modulus agree with the best estimates available in literature. These results show that robust and accurate calculations with nearly converged Gaussian basis sets have now become possible in the condensed phase at least for large band gap systems. However, we reiterate

	R_c[Å]	E(HF)[a.u.]	H[a.u.][(a)]	Li[a.u.][(b)]	$\varepsilon_{\mathrm{HF}}^{\mathrm{coh}}$ [a.u.]
2×2×2	4.0	-32.244609	-0.499957	-7.428493	-0.132702
3×3×3	6.0	-32.256844	-0.499974	-7.432137	-0.132100
4×4×4	8.0	-32.258022	-0.499974	-7.432582	-0.131949
5×5×5	10.0	-32.258179	N/A	N/A	N/A

[(a)] basis set limit -0.500000
[(b)] basis set limit -7.432727

Table 6.5: Results obtained with `CP2K` and the truncated Coulomb operator for unit cells that are a multiple of the cubic unit cell (4.084 Å). The columns show the size of the unit cell, the range of the truncated Coulomb operator (R_c), the Hartree-Fock energy per four LiH ion pairs, the H atom energy, the Li atom energy, and the cohesive energy (ε_{HF}^{coh}), respectively.

that the computational workload for both methods introduced in the present work is strongly dependent on the decay properties of the density matrix. Thus, for *e.g.* small gap semiconductors it is very likely that extrapolation of SR-HFX energies to full range would become difficult whereas the truncated Coulomb operator approach will still be robust enough to enable small gap materials being treated on the HF level using large Gaussian basis sets. Certainly, high accuracy results ask for tailoring high quality basis sets, as the one introduced in this work. Clearly, finding the optimal Gaussian basis set is certainly nontrivial and the degree of complexity in this task increases with the complexity of the material of interest. Finally, we stress that these results will contribute to the growing usefulness of hybrid density functionals for condensed phase applications and opens, for these systems, the way to accurate calculations based on post-Hartree-Fock methods.

Chapter 7

Auxiliary Density Matrix Methods (ADMM) for Exact Exchange calculations [154]

The calculation of Hartree-Fock exchange (HFX) is computationally demanding for large systems described with high quality basis sets. In this work, we show that excellent performance and good accuracy can nevertheless be obtained if an auxiliary density matrix is employed for the HFX calculation. Several schemes to derive an auxiliary density matrix from a high quality density matrix are discussed. Key to the accuracy of the auxiliary density matrix methods (ADMM) is the use of a correction based on standard generalized gradient approximations for HFX. ADMM integrates seamlessly in existing HFX codes, and in particular can be employed in linear scaling implementations. Demonstrating the performance of the method, the effect of HFX on the structure of liquid water is investigated in detail using Born-Oppenheimer molecular dynamics simulations (300 ps) of a system of 64 molecules. Representative for large systems are calculations on a solvated protein (Rubredoxin), for which ADMM outperforms the corresponding standard HFX implementation by approximately a factor 20.

7.1 Introduction

The success of density functional theory (DFT) can be attributed to the fact that it can provide an accurate description of the electronic structure at a moderate computational cost. DFT has become a unique tool to describe systems containing hundreds to thousands of atoms. Not only is it possible to describe molecules in the gas phase, properties of condensed phase systems

such as liquids and solids can also be computed. For these systems, using contemporary computer resources, it has become possible to go beyond a static description of matter, and finite temperature effects can be included directly through ab initio molecular dynamics (MD) simulations. Large scale, condensed phase and dynamical simulations have mostly adopted a relatively simple form for the exchange and correlation functional, namely the semi-local generalized gradient approximation (GGA). However, it becomes increasingly clear that an improved description of the electronic structure, and thus more accurate results, can only be obtained by functionals that go beyond the GGA form, and incorporate a non-local term such as Hartree-Fock exchange (HFX). The computational cost of these non-local terms is typically much larger than that of the local terms. Consequently, there is significant interest in finding efficient approaches to deal with these non-local forms.

The efficiency of a HFX calculation depends strongly on the algorithm employed. A straightforward implementation based on localized basis sets scales with the fourth power of the system size. However, integral screening [42] reduces the scaling with system size to quadratic, and for short range operators, such as screened [51] or truncated exchange [95, 103, 155, 156], to linear scaling. Non-metallic systems furthermore allow for a screening on the density matrix [48], which leads to linear scaling also for long-range operators. Using these techniques, HFX can be evaluated also for condensed phase systems containing a few thousand atoms [95], and can be used to perform ab initio molecular dynamics simulations [35]. Despite the favorable scaling with system size, HFX calculations scale very poorly with basis set quality. This is an important issue, since high quality results not only require accurate functionals, but also good basis sets. There are several reasons why the cost of HFX depends very strongly on the basis employed. Indeed, even in a linear scaling code, the cost increases with the fourth power of the number of (primitive) basis functions per atom. Basis sets with a high l-quantum number (polarization functions) are therefore costly, as the number of basis functions per atom grows quadratically with l. Heavily contracted basis functions, such as the molecularly optimized basis sets proposed in Ref. [92] , are expensive since for each quartet of basis functions a very larger number of primitive integrals needs to be considered. Very flexible basis sets, or basis sets with diffuse primitives are costly for several reasons. First, diffuse primitives are non-zero in a larger part of space, and thus screening becomes less efficient. This is particularly important in condensed phase systems, where periodic boundary conditions provide a potentially unlimited number of interacting atomic sites. Second, uncontracted diffuse primitives influence the condition number of the overlap matrix (S) strongly, and a poor condition number in turn implies that a tighter screening threshold has to be employed [95] to

obtain a stable self consistent calculation. Third, the sparsity of the matrix representation of the density matrix (P) also depends strongly on the condition number of S, making density matrix screening less efficient for poorly conditioned basis sets. Tab. 7.1 illustrates this problem by providing costs and maximal thresholds needed in order to get converged results for a water cluster containing 20 water molecules. Clearly, a technique which reduces the

basis	$\kappa(S)$	threshold	cost [ERIs]	cost [s]
3-21G*	4.9E+01	1.0E-04	2.3E+07	0.06
6-31G**	2.1E+02	1.0E-05	5.2E+08	0.35
6-311G++G**	1.2E+05	1.0E-07	1.1E+10	11.71
pc-0	5.2E+01	1.0E-04	1.7E+07	0.07
pc-1	4.5E+03	1.0E-05	4.4E+08	0.50
pc-2	5.7E+05	1.0E-07	2.0E+10	11.21
aug-pc-1	1.4E+06	1.0E-08	5.0E+10	53.23
aug-pc-2	3.9E+08	1.0E-09	1.5E+12	766.92
def2-QZVP	7.1E+04	1.0E-08	3.2E+11	127.16
aug-def2-QZVP	8.5E+05	1.0E-08	6.2E+11	331.61

Table 7.1: Impact of the basis set quality for the wavefunction optimization of a 20 water cluster. The condition number $\kappa(S)$ of the overlap matrix determines the maximal possible screening threshold. The latter needs to be chosen more tightly, if $\kappa(S)$ gets large. This is reflected in the cost of a calculation, which is given once by the number of Cartesian four-center electron repulsion integrals (ERIs) that need to be evaluated and the time in seconds that is spent in building the Fock matrix in the first self consistent field (SCF) step. 3-21G*, 6-31G**, 6-311G++G** refer to basis sets by Pople and co-workers [157, 158, 159, 160], the polarization consistent (pc) basis sets have been developed by Jenssen [114, 115, 116], the def2-QZVP basis by Ahlrichs and co-workers [161]. Timings are obtained on 128 cores of a CRAY-XT5.

impact of the basis set on the computational cost is a significant progress. During the last decade, much effort has been invested into solving this problem and many different techniques have been proposed. Among them are methods that apply an approximate resolution of identity, for example RI [162] or Cholesky decomposition [163]. These schemes rely on the introduction of auxiliary basis functions in terms of which the four center integrals can be approximated by corresponding two- and three-center terms. In order

to improve efficiency, Sodt. et al. [164] developed a local variant of RI, atomic resolution of identity (ARI). A slightly different post-Hartree-Fock approach in a dual basis was introduced in Ref. [165] where a reference calculation in a small basis set is perturbatively corrected to a large basis set. A different approximation for the two-electron integrals has been proposed by Friesner and co-workers [166] and has been termed pseudo-spectralmethod. Recently, Neese et al. [167] presented an algorithm called COSX that is a combination of semi-numerical methods and RI. Furthermore, there exist several schemes to achieve linear scaling in the context of plane wave basis sets such as the multiwavelet based ansatz of Harrison et al. [168] or FFT based algorithms as presented in Refs. [39, 90, 107].
In this work, we propose to employ an auxiliary density matrix to evaluate the expensive non-local part of the functional, while all other energy components are computed with the primary (original) density matrix. The auxiliary density matrix will be constructed in a way that allows for a rapid evaluation of the HFX energy, using any algorithm, including traditional or linear scaling approaches. In order to ensure that the quality of the calculation is influenced as little as possible by the quality of the auxiliary density matrix, a correction term is added to the exchange and correlation functional. Based on a GGA for exchange, this correction takes the difference between auxiliary and primary density matrix into account. All terms of the resulting density functional are straightforward to compute, but there is considerable freedom in how to obtain from a given primary density matrix a suitable auxiliary density matrix. In this paper, various procedures are discussed and tested. Tests are presented in Sec. 7.3 and include gas phase thermochemistry, basis set superposition error, electronic structure including band gaps, large systems, and liquid water. The theory is introduced in the following section, but for mathematical derivations and technical details we refer to the appendices.

7.2 Theory

7.2.1 Basic Concepts

In Kohn-Sham DFT, the total energy of a system consisting of N_e electrons can be written in terms of the electron density

$$\rho(\mathbf{r}) = \sum_{i=1}^{N_\mathrm{e}} |\psi_i(\mathbf{r})|^2, \tag{7.1}$$

where ψ_i denote the single particle wavefunctions, which are assumed to be real valued. The total energy is then expressed in terms of a functional of

the electron density as

$$E[\rho] = T_s[\rho] + J[\rho] + E_{\mathrm{xc}}[\rho] + \int v(\mathbf{r})\rho(\mathbf{r})d\mathbf{r}, \tag{7.2}$$

with the standard abbreviations for kinetic, Hartree and exchange-correlation energy and the part due to the external potential. In hybrid DFT, the exchange-correlation functional is augmented by a certain fraction of Hartree-Fock exchange based on the wavefunctions $\{\psi_i\}$

$$E_{\mathrm{xc}}[\rho] = \alpha E_x^{\mathrm{HFX}}[\{\psi_i\}] + (1-\alpha)E_x^{\mathrm{DFT}}[\rho] + E_c^{\mathrm{DFT}}[\rho], \tag{7.3}$$

where α denotes the fraction of HFX and E_x and E_c are the density functionals for exchange and correlation, respectively. In the presence of an atomic centered basis set $\{\phi_\mu(\mathbf{r})\}$

$$\psi_i(\mathbf{r}) = \sum_\mu C^{\mu i}\phi_\mu(\mathbf{r}), \tag{7.4}$$

the Hartree-Fock exchange energy can be expressed in terms of a density matrix and two-electron integrals (ERIs)

$$E_x^{\mathrm{HFX}}[P] = -\frac{1}{2}\sum_{\lambda\sigma\mu\nu} P^{\mu\sigma}P^{\nu\lambda}\,(\mu\nu|\lambda\sigma)\,, \tag{7.5}$$

where the density matrix elements $P^{\mu\nu}$ are obtained from the molecular (MO) coefficients as

$$P^{\mu\nu} = \sum_i C^{\mu i}C^{\nu i} \Leftrightarrow P = CC^T \tag{7.6}$$

and the ERIs are defined as

$$(\mu\nu|\lambda\sigma) = \int\int \phi_\mu(\mathbf{r}_1)\phi_\nu(\mathbf{r}_1)g(|\mathbf{r}_2-\mathbf{r}_1|)\phi_\lambda(\mathbf{r}_2)\phi_\sigma(\mathbf{r}_2)d\mathbf{r}_1\mathbf{r}_2, \tag{7.7}$$

with the interaction potential $g(r)$ that is Coulombic $(1/r)$ in standard Hartree-Fock theory. The fourth order scaling of HFX with basis set size can be directly inferred from Eq. 7.5.
By introducing an auxiliary density matrix $\hat{P} \approx P$ that is either smaller in size or more rapidly decaying than the original one, the evaluation of HFX can be sped up significantly. The HFX energy can be written as

$$\begin{aligned} E_x^{\mathrm{HFX}}[P] &= E_x^{\mathrm{HFX}}[\hat{P}] + \left(E_x^{\mathrm{HFX}}[P] - E_x^{\mathrm{HFX}}[\hat{P}]\right) \\ &\approx E_x^{\mathrm{HFX}}[\hat{P}] + \left(E_x^{\mathrm{DFT}}[P] - E_x^{\mathrm{DFT}}[\hat{P}]\right). \end{aligned} \tag{7.8}$$

The assumption behind this approximation is that *the difference* in the exchange energy between primary and auxiliary density matrix is well captured by a GGA, even in those cases where GGA exchange and HFX might be qualitatively different. Eq. 7.8 amounts to computing the HFX energy with an auxiliary density matrix, while a GGA correction is introduced which takes the difference between auxiliary and primary density matrix into account. As shown in Sec. 7.3, applying this correction indeed improves upon uncorrected results. Clearly, our approach yields the original HFX energy as either the quality of the auxiliary density matrix or of the correcting functional improves. In this work, we have based the GGA correction on PBE exchange [96, 109], and have not explored other parameterizations or other functionals. The introduction of Eq. 7.8 in hybrid density functionals is natural and straightforward, and usually, because only a fraction of exchange is needed, will introduce a smaller error. If hybrid functionals employ a non-Coulombic operator the exchange functional needs to be chosen consistently with the shape of the interaction potential ($g(r)$) in the ERI calculation. Currently, the GGA correction for the standard Coulomb potential, the short range (erfc) and the truncated Coulomb potential have been implemented and tested.

7.2.2 Auxiliary density matrices

The performance and accuracy of the ADMM scheme depends on how the auxiliary density matrix is constructed, and various approaches seem possible. In this section, we present methods that either rely on the use of an auxiliary basis set, or directly manipulate the sparsity of the density matrix.

The size of P obtained from a high quality primary basis set (PBS) $\{\phi_\mu(\mathbf{r})\}$ can be reduced by introducing an auxiliary basis set (ABS) $\{\hat{\phi}_\mu(\mathbf{r})\}$ for the description of the underlying wavefunction

$$\hat{\psi}_i(\mathbf{r}) = \sum_\mu \hat{C}^{\mu i}\hat{\phi}_\mu(\mathbf{r}), \tag{7.9}$$

i.e.

$$\hat{P}^{\mu\nu} = \sum_i \hat{C}^{\mu i}\hat{C}^{\nu i} \Leftrightarrow \hat{C}\hat{C}^T. \tag{7.10}$$

An optimal value for the MO coefficients can be obtained by requiring that the square difference for the occupied wavefunctions in ABS and PBS representation is minimized

$$\min_{\hat{C}} \sum_j \int \left(\psi_j(\mathbf{r}) - \hat{\psi}_j(\mathbf{r})\right)^2 d\mathbf{r}. \tag{7.11}$$

This yields the following expression for the auxiliary MO coefficients

$$\hat{C} = AC, \tag{7.12}$$

where A is defined as the projector between the two basis sets

$$A = \hat{S}^{-1}Q \tag{7.13}$$

with the overlap matrices

$$\hat{S}_{nn'} = \int \hat{\phi}_n(\mathbf{r})\hat{\phi}_{n'}(\mathbf{r})d\mathbf{r} \quad \text{and} \quad Q_{nm} = \int \hat{\phi}_n(\mathbf{r})\phi_m(\mathbf{r})d\mathbf{r}. \tag{7.14}$$

A slightly more complicated formula is obtained when the auxiliary wavefunctions are required to minimize Eq. 7.11 subject to the constraint that they remain orthonormal. This constraint can be enforced introducing Lagrangian multipliers (Λ_{kl}) in Eq. 7.11 as

$$\min_{\tilde{C}} \left[\sum_j \int \left(\psi_j(\mathbf{r}) - \tilde{\psi}_j(\mathbf{r}) \right)^2 d\mathbf{r} + \sum_{k,l} \Lambda_{kl} \left(\int \tilde{\psi}_k(\mathbf{r})\tilde{\psi}_l(\mathbf{r})d\mathbf{r} - \delta_{kl} \right) \right]. \tag{7.15}$$

The coefficients $\tilde{C}$ that minimize this expression can be obtained as

$$\tilde{C} = \hat{C}\Lambda^{-1/2} \quad \text{with} \quad \Lambda = \hat{C}^T\hat{S}\hat{C}. \tag{7.16}$$

where $\hat{C}$ is defined by Eq. 7.12.

Of course, there is significant freedom in selecting the auxiliary basis set, and the choice need not to be homogenous in space. For example, for large systems with a chemically active region, such as enzymes, it is natural to retain the high quality primary basis where exchange matters most, while a lower quality auxiliary basis can be used for the bulk. Furthermore, note that the explicit shape of the basis functions (Gaussian functions, Slater functions, ...) is not important, and indeed need not to be the same in the auxiliary and primary basis sets. The method thus provides an interesting approach for computing exchange contributions in programs that do not employ Gaussian basis functions and for which the calculation of exchange is relatively difficult.

The two different sets of MO coefficients, $\hat{C}$ and $\tilde{C}$ correspond two different density matrices:

$$\tilde{P} = \tilde{C}\tilde{C}^T = \hat{C}\Lambda^{-1}\hat{C}^T, \tag{7.17}$$

and

$$\hat{P} = \hat{C}\hat{C}^T = APA^T \tag{7.18}$$

that can be used as an auxiliary density matrix. We will refer to the first as purified wavefunction fitting or ADMM1 and to the second as non-purified wavefunction fitting or ADMM2 (see Sec. 7.2.3 for explanation of nomenclature).

A strategy directly aimed at obtaining a sparse auxiliary density matrix relies on a blocking of the primary density matrix. This strategy is applicable if the system of interest can be divided into subsystems that have no important exchange interactions beyond what is captured with a GGA. In this case, the non-relevant blocks in the auxiliary density matrix can just be zeroed, and to some extend this method can be considered a subsystem based neglect of diatomic differential overlap (NDDO) If all inter-subsystem blocks are zeroed the approximate density matrix will be positive definite, however, we employ the slightly generalized form of the auxiliary density matrix as

$$\hat{P} = P \otimes B \tag{7.19}$$

where B is a blocking matrix with $B_{ij} \in \{1, 0\}$ and $\otimes$ denotes the Hadamard product of two matrices. In this case, B can reflect the molecular topology, and allow for connections between subsystems. In the general case, the resulting $\hat{P}$ need not to be positive definite. This method of obtaining an auxiliary density matrix will be referred to as blocking or ADMM3 in the following.

7.2.3 Density matrix purification

As already mentioned, an approximate density matrix might not fulfill the properties of a pure density matrix:

$$P = P^T, \tag{7.20}$$
$$PSPS = PS, \tag{7.21}$$
$$\mathrm{tr}(PS) = N_e, \tag{7.22}$$

i.e. symmetry, idem-potency and particle conservation. For the three approximations mentioned in the previous section, all three conditions are only fulfilled by ADMM1, i.e. the purified wavefunction fitting scheme. ADMM2 and the block diagonal version of ADMM3 fulfill a property of ensemble averaged (finite temperature) density matrices i.e. that the eigenvalues of $\hat{P}$ are bounded by 0 and 1, which is a relaxed version of the idempotency condition. In order to compute a GGA correction for exchange, it is essential that the approximate density matrix is at least positive semi-definite. Fortunately, there exist purification algorithms that can restore the idempotency of an approximate density matrix.

Well known is the McWeeny purification algorithm [169] which, in the presence of an overlap matrix, is defined as follows

$$\bar{P}_{n+1} = f(\bar{P}_n) = 3\bar{P}_n S\bar{P}_n - 2\bar{P}_n S\bar{P}_n S\bar{P}_n \tag{7.23}$$

for an initial guess $\bar{P}_0 = \hat{P}$. The pure density matrix is than given as

$$\tilde{P} = \lim_{n\to\infty} \bar{P}_n. \tag{7.24}$$

An interesting property of this algorithm is that it can be implemented in a linear scaling fashion [170, 171]. In the current context, we prefer an extension of the McWeeny procedure based on a Cauchy integral representation [172]

$$\tilde{P} = S^{-1}\left[\frac{1}{2\pi i}\oint \frac{\Theta(z-0.5)}{S^{-1}z - \hat{P}}dz\right] S^{-1}, \tag{7.25}$$

where $\Theta(z)$ denotes the Heaviside function. This scheme yields a pure density matrix for all input matrices, is non-iterative, but is not easily incorporated in a linear scaling procedure. Through Eq. 7.25 a purified $\tilde{P}$ can be interpreted as a matrix functional of a non-pure $\hat{P}$. This is an important property, which will be used to derive an expression for the Kohn-Sham matrix in the following section. Eq. 7.25 can be easily computed using basic linear algebra techniques as

$$\tilde{P} = S^{-1}RLR^T S^{-1}, \tag{7.26}$$

where R is the matrix of eigenvectors of the generalized eigenvalue problem

$$\hat{P}R = S^{-1}R\lambda \tag{7.27}$$

and L is the diagonal matrix $L_{ii} = \Theta(\lambda_i - 0.5)$ with the corresponding eigenvalues λ_i. At this point, and as shown in the appendix, we remark that purification by Eq. 7.25 of the density matrix obtained from non-purified wavefunction fitting (ADMM2) exactly yields the density matrix derived from the purified wavefunction fitting (ADMM1).

7.2.4 Kohn-Sham matrix and the SCF procedure

In a standard SCF procedure, an improved density matrix is obtained from a diagonalization of the Kohn-Sham matrix. The Kohn-Sham matrix itself is obtained as the derivative of the total energy with respect to the density matrix. In ADMM, the total energy can be considered to consist of two parts, one part depending explicitly on the primary density matrix ($E[P]$), and one part depending explicitly on the auxiliary matrix ($\tilde{E}[\tilde{P}]$):

$$E_{\text{total}} = E[P] + \tilde{E}[\tilde{P}]. \tag{7.28}$$

The Kohn-Sham matrix associated with this expression

$$K_{\text{total}} = \frac{dE[P]}{dP} + \frac{d\tilde{E}[\tilde{P}]}{dP} = K + \frac{d\tilde{E}[\tilde{P}]}{dP}, \tag{7.29}$$

contains one non-trivial term

$$\frac{d\tilde{E}[\tilde{P}]}{dP} = \frac{d\tilde{E}}{dP} = \frac{d\tilde{E}}{d\tilde{P}}\frac{d\tilde{P}}{d\hat{P}}\frac{d\hat{P}}{dP} = \tilde{K}\frac{d\tilde{P}}{d\hat{P}}\frac{d\hat{P}}{dP}, \tag{7.30}$$

where $\tilde{K}$ is the Kohn-Sham matrix constructed from the purified density matrix. $\frac{d\hat{P}}{dP}$ is readily evaluated for wavefunction fitting and blocking, while $\frac{d\tilde{P}}{d\tilde{P}}$ can be obtained through the Cauchy integral Eq. 7.25. We obtain in the case of purified wavefunction fitting (for details see App. 7.5.2)

$$\frac{d\tilde{E}}{dP} = A^T R \left[\left(R^T \tilde{S}^{-1} \tilde{K} \tilde{S}^{-1} R \right) \otimes M \right] R^T A, \tag{7.31}$$

with R as defined above, and

$$M_{kj} = \begin{cases} \frac{\Theta(\lambda_k - 0.5) - \Theta(\lambda_j - 0.5)}{\lambda_k - \lambda_j}, & k \neq j \\ \delta(\lambda_k - 0.5), & k = j \end{cases}. \tag{7.32}$$

In the appendix, computationally more efficient expressions are presented for optimization schemes that only require the derivative of the energy with respect to the MO coefficients ($\frac{dE}{dC}$) or that exploit the special structure of $\hat{P}$.

At this point, it is important to point out that the eigenvalues of the Kohn-Sham matrix in ADMM might be very different from the eigenvalues of the Kohn-Sham matrix in the primary basis. This is not an indication of the inaccuracy of the scheme, nor is it a problem for the SCF procedure, but is related to the fact that purification as part of the energy functional partially accounts for the orthonormality constraint of the wavefunction (see also App. 7.5.7). In order to use the eigenvalues of the ADMM Kohn-Sham matrix directly as orbital energies, e.g. to calculate the band gaps of a system, an ADMM scheme without purification needs to be employed. For the non-purified wavefunction fitting (ADMM2), the corresponding Kohn-Sham matrix is given by

$$K_{\text{total}} = K[P] + A^T \hat{K} A, \tag{7.33}$$

where $\hat{K}$ is build from $\hat{P}$. This simple expression suggests an expression for use with purified wavefunction fitting (ADMM1), i.e. orbital energies can be obtained from eigenvalues of

$$K_{\text{total}} = K[P] + A^T \tilde{K} A, \tag{7.34}$$

where $\tilde{K}$ is constructed from $\tilde{P}$. We will show in Sec. 7.3.6 that this expression can be accurate.

7.3 Assessment and validation of the method

7.3.1 Computational details

All algorithms have been implemented in `CP2K` [36], a freely available molecular simulation package. `CP2K` is well suited for these calculations as the density functional module `Quickstep` [14], implements a linear scaling and fast scheme for calculations based on local functionals. Indeed, the Gaussian and plane waves (GPW) scheme [13] and its augmented (GAPW) variant [15] provide an efficient method to evaluate the Coulomb energy for pseudopotential and all-electron calculations, respectively. These approaches use Fourier transform based techniques, i.e. a plane wave auxiliary basis, and scale favorably with basis set size. Recently, an efficient, massively parallel and linear scaling implementation of Hartree-Fock exchange has been incorporated into the `CP2K` code [35, 95]. Despite this efficiency, calculations including HFX and employing high quality basis sets, are at least one order of magnitude more expensive than calculations based on GGAs. ADMM aims at resolving this issue. Currently, the GGA correction term required for ADMM has only been implemented for use with the GPW method, and consequently all calculations are based on Goedecker, Teter, Hutter (GTH) pseudopotentials [173]. pseudopotentials[119] constructed for the PBE functional have been used throughout. This is an approximation that poorly describes core-valence exchange and that is known to introduce errors in excess of 0.1eV in the computation of band gaps[174, 175], but appears to give reasonable results for ground state properties (see e.g. 7.3.2). In this work, both ADMM and the standard HFX implementation employ the same pseudopotential approximation, so that a meaningful comparison can be made. The all-electron implementation of ADMM and the development of pseudopotentials for hybrid functionals are beyond the scope of the current work.

Calculations based on pseudopotentials use split valence Gaussian basis sets as discussed in Ref. [14], the fully contracted molecularly optimized (MOLOPT) basis sets discussed in Ref. [92], or a reference basis (GTH-def2-QZVP), which combines the pseudo-atomic orbitals of the MOLOPT basis, with uncontracted valence, and polarization exponents of the Ahlrichs quadruple-ζ (aug-)def2-QZVP [161] basis set. The latter basis can be considered close to the basis set limit. The choice of auxiliary basis for the ADMM method will in general be dictated by accuracy and performance requirements

basis	$\kappa(S)$	threshold	cost [ERIs]	cost [s]
cFIT3	1.3E+02	1.0E-04	1.8E+07	0.08
FIT3	1.5E+02	1.0E-04	1.6E+07	0.10
cpFIT3	1.7E+02	1.0E-04	1.0E+08	0.13
pFIT3	2.3E+02	1.0E-04	9.0E+07	0.15
aug-cFIT3	5.5E+04	1.0E-07	1.1E+09	3.38
aug-FIT3	6.1E+04	1.0E-07	1.1E+09	4.14
aug-cpFIT3	5.9E+04	1.0E-07	3.2E+09	6.09
aug-pFIT3	6.4E+04	1.0E-07	3.0E+09	6.78

Table 7.2: Cost for using the FIT3 basis sets on a cluster of 20 water molecules. For comparison and details, see Tab. 7.1.

of a particular calculation. Indeed, the gain in performance for the hybrid part of the calculation might allow for better primary basis sets, or large systems can be simulated by more aggressively using a smaller auxiliary basis. Here, we are interested in exploring the accuracy of relatively small auxiliary basis sets, of which a library of eight different basis sets per atom have been constructed. This basis employs three Gaussian exponents for the valence orbitals, optimized in atomic calculations. We will refer to this uncontracted basis, without polarization functions, as FIT3, while a contraction of this basis (to double zeta quality) is referred to as cFIT3. In order to improve accuracy, polarization functions from the standard 6-31G** basis sets have been added yielding pFIT3 and cpFIT3 basis sets. Finally, an augmented version has been constructed by adding a 'diffuse' function (typical exponents are 0.03 for hydrogen and 0.09 for oxygen), yielding aug-FIT3, aug-cFIT3, aug-pFIT3, aug-cpFIT3.

7.3.2 GMTKN24 database

The GMTKN24 database is a compilation of 24 different chemically relevant benchmarks collected and established by L. Goerigk and S. Grimme [176, 177]. It is based on 1049 atomic and molecular single point energies that are combined to yield 731 relative energies. These energies can be compared to available benchmark data, derived from either theory or experiment. In order to judge the quality of a computational method using a single number, the authors defined a weighted total mean absolute deviation (WTMAD) that combines all mean absolute deviations (MADs). This convenient measure is adopted here to judge the quality of the wavefunction fitting meth-

Method	PBS	ABS	WTMAD	$\text{WTMAD}_{\text{ref}}$
STD	GTH-def2-QZVP	-	5.0	0.0
	FIT3	-	15.3	10.8
	pFIT3	-	7.1	4.2
ADMM1	GTH-def2-QZVP	cFIT3	5.3	1.0
	GTH-def2-QZVP	FIT3	5.3 (6.1)	0.7 (1.8)
	GTH-def2-QZVP	cpFIT3	5.0	0.7
	GTH-def2-QZVP	pFIT3	4.9 (5.5)	0.5 (1.2)
ADMM2	GTH-def2-QZVP	cFIT3	5.3	1.1
	GTH-def2-QZVP	FIT3	5.3	0.8
	GTH-def2-QZVP	cpFIT3	4.9	0.7
	GTH-def2-QZVP	pFIT3	4.9	0.5

Table 7.3: Shown are WTMAD and $\text{WTMAD}_{\text{ref}}$ in kcal/mol for the GMTKN24 database and the PBE0 functional. Whereas WTMAD refers to the weighted mean absolute deviation with respect to experimental and theoretical benchmark results, $\text{WTMAD}_{\text{ref}}$ refers to deviations with respect to PBE0 reference results obtained using a standard HFX implementation and the high quality GTH-def2-QZVP basis. Standard (STD) HFX calculations with the GTH-def2-QZVP, FIT3, and pFIT3 basis sets are employed to establish the quality of these basis sets as a primary basis set (PBS). Wavefunction fitting results with purification (ADMM1) and without purification (ADMM2) are provided using four different auxiliary basis sets (ABS), while the GTH-def2-QZVP has been employed as a primary basis in all these cases. The results in parenthesis have been obtained using ADMM, but ignoring the GGA correction.

ods ADMM1 and ADMM2 for various basis sets. Results, summarized in Tab. 7.3, are based on the hybrid PBE0 functional [28, 29, 30] without empirical dispersion correction [178]. In a first step, reference results using a standard HFX implementation have been generated for the GTH-def2-QZVP basis. As in Ref. [176], an augmented basis set has been used for two of the subsets. ADMM results can be directly compared to these reference results, and deviations with respect to this data is referred to as $\mathrm{WTMAD}_{\mathrm{ref}}$. WTMAD without subscript is used to refer to the deviations with respect to the experimental and theoretical benchmark results. Secondly, to quantify the expected poor quality of the FIT3 family as a primary basis, these basis sets have been used with a standard HFX implementation. These calculations yield a $\mathrm{WTMAD}_{\mathrm{ref}}$ in the range 4–11 kcal/mol, and WTMADs in the range 7–15kcal/mol, far worse than the typical performance of local functionals, with a good basis set, on this database [176]. Thirdly, ADMM calculations have been performed using the FIT3 family as auxiliary basis sets. Whenever the primary basis is augmented, an augmented auxiliary basis has been used as well. The results obtained with ADMM are in very close agreement with the reference calculations. In particular, both ADMM1 and ADMM2 using the better auxiliary basis set (pFIT3 or cpFIT3) are basically indistinguishable in terms of error with respect to the benchmark data (WTMAD), and have an error of less than 1 kcal/mol compared to the reference run ($\mathrm{WTMAD}_{\mathrm{ref}}$). In the case of FIT3, ADMM results improve by 10 kcal/mol as compared to standard HFX calculations with the same basis. In Tab. 7.3 it is also shown that including the GGA correction term in ADMM more than halves the $\mathrm{WTMAD}_{\mathrm{ref}}$, thus emphasizing the benefit of the correction term. Finally, we observe that ADMM1 and ADMM2 perform equally well, suggesting that in this case the purification is not essential. In the cases we have verified, $\hat{P}$ had eigenvalues close to 0 and 1, even for the small cFIT3 basis. This data shows that results of def2-QZVP quality can be obtained at a cost similar to 6-31G**. The relatively modest cost of computing the full database with ADMM has been exploited to benchmark the quality of the the PBE0-TC-LRC functional proposed in Ref. [95]. This functional uses a truncated operator for the calculation of exchange, but, like HSE [31, 32], corrects for the long range part using a density functional. As shown in Ref. [95], the PBE0-TC-LRC is useful in the condensed phase, but can also reduce the computational cost for (large) molecules. In Tab. 7.4 the effect of varying the range of exchange has been studied systematically, using ADMM1 with the pFIT3 basis, for PBE0-TC-LRC functionals including 20% and 25% of non-local exchange.

These WTMADs clearly show that the range of the truncated operator can be reduced to 2Å without affecting the quality of the results. The lowest

α	0.50	0.75	1.00	1.25	1.50	1.75	2.00	2.25	2.50	3.00	4.50	6.00	∞
0.20	5.5	5.3	5.6	5.6	5.3	5.0	4.9	4.8	4.7	4.7	4.8	4.8	N/A
0.25	5.5	5.5	6.1	6.3	5.9	5.4	5.2	5.0	4.9	4.9	4.9	4.9	5.0

Table 7.4: Shown are WTMADs in kcal/mol for the GMTKN2424 database and the PBE0_TC_LRC functional for several different cutoff radii in the range of 0.5 to 6.0 Å. The column denoted with ∞ refers to the standard PBE0 hybrid functional. All calculations have been performed twice for different fractions of Hartree-Fock exchange $\alpha = 0.2$ and $\alpha = 0.25$.

WTMAD, slightly smaller than the WTMAD for PBE0, is found for 20% non-local exchange and a range of 2.5Å.

7.3.3 Basis Set Superposition Error

In this section, the impact of ADMM on the basis set superposition error (BSSE) for the water dimer is investigated. Indeed, the BSSE is a concern as soon as small, lower quality basis sets are employed. Here, it is shown that small auxiliary basis sets introduce only a moderate BSSE, especially if compared to the BSSE in standard HFX calculations with the same basis. In order to quantify the BSSE, the counterpoise correction [179] has been computed for a water dimer at fixed equilibrium geometry, for various methods. These results are summarized in Tab. 7.5. As expected, using the non-augmented FIT3 basis sets as primary basis leads to errors of approximately 3 kcal/mol. This error is large when compared to a basis using diffuse primitives, such as the TZV2P-MOLOPT basis, which has a BSSE of only 0.1 kcal/mol. However, within the ADMM scheme, the error reduces to 0.8 kcal/mol, approximately a four-fold reduction. Using the augmented auxiliary basis sets reduces the error to approximately 0.3 kcal/mol, similar to, but not quite as good as, the quality of the primary basis set. Note that, since an auxiliary basis set method is not necessarily variational in the auxiliary basis, the counterpoise corrections can be of both signs. This can lead to an error cancellation, which is presumably the reason why ADMM2 performs surprisingly well with the lower quality auxiliary basis sets. It can thus be concluded that both wavefunction fitting methods do not suffer from the large BSSE associated with the inferior quality of the auxiliary basis even though the BSSE does not reduce to the extent of the primary basis in all cases.

Basis set	STD	ADMM1	ADMM2
cFIT3	-3.112	0.771	0.223
FIT3	-3.128	0.520	-0.006
cpFIT3	-3.468	0.882	0.248
pFIT3	-3.448	0.604	0.004
aug-cFIT3	-1.889	-0.193	-0.346
aug-FIT3	-1.744	-0.095	-0.253
aug-cpFIT3	-1.023	-0.246	-0.325
aug-pFIT3	-1.005	-0.162	-0.247
TZV2P-MOLOPT	-0.123	-0.123	-0.123

Table 7.5: Shown are counterpoise corrections in kcal/mol to the PBE0 binding energy of a water dimer. STD refers to traditional hybrid calculations, using the shown basis set as primary basis set. ADMM1 and ADMM2 refer to the wavefunction fitting methods, using the TZV2P-MOLOPT basis set as primary basis and the shown basis as auxiliary basis set.

7.3.4 H_2^+ dissociation curve

ADMM calculations that are GGA corrected might be biased from deficiencies of the underlying GGA functional. In order to investigate this effect, dissociation curves for H_2^+ at different levels of theory have been calculated. As is well known, GGA functionals, such as PBE exchange, describe the dissociation of this system incorrectly [180]. Fig. 7.1 compares results obtained from a Hartree-Fock reference calculation, which is exact for this system, with results obtained from ADMM1. The primary basis was chosen to be the same as in the reference calculation (TZV2P-MOLOPT) while several different ABS have been applied. The results clearly show, that the wavefunction fitting is not biased by the GGA correction. Furthermore, as shown in the inset, better quality ABS consistently improve the description of the potential around the minimum. It can thus be concluded that the qualitatively important effects of HFX are properly retained and that the GGA correction does not introduce artefacts of the underlying functionals.

7.3.5 The cationic hole in liquid water

In order to probe the effect of the dual basis set approach on the electronic structure directly, the spin density distribution of the cationic hole in bulk liquid water has been computed. The poor performance of local functionals

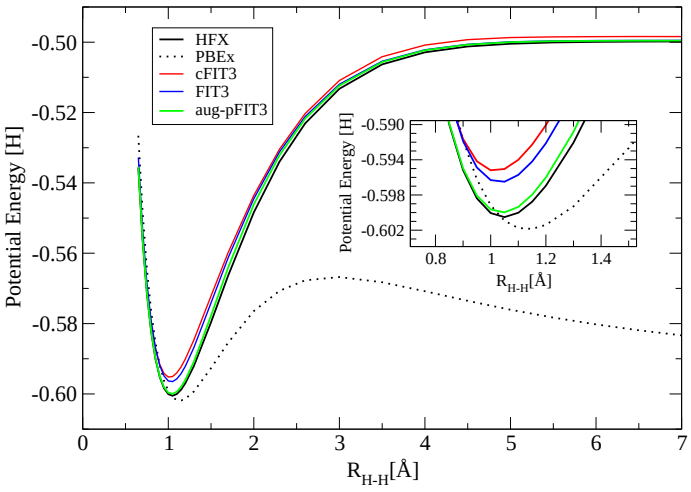

Figure 7.1: Shown are dissociation curves for H_2^+ obtained from different calculations. The black solid line depicts the reference Hartree–Fock run with the TZV2P-MOLOPT basis set. Red, blue and green lines represent results for ADMM1 for auxiliary basis sets of increasing quality, cFIT3, FIT3 and aug-pFIT3 respectively. The dotted black line shows the dissociation curve obtained from a pure GGA exchange calculation (PBEx). In the inset, a magnification of the potential energy around the minimum is presented.

for the radical cation water dimer was discussed in detail by Sodupe et al. in Ref. [181] and attributed to the self interaction error, which favors configurations with a delocalized spin density distribution. Hybrid functionals with a relatively large fraction of exchange, for example BH&HLYP [25, 24], perform significantly better. In Ref. [182], ionization of bulk liquid water has been probed, and the difficulty of DFT to properly describe the electronic structure has been discussed. In particular, it has been found that the electron hole, or similarly the spin density, is delocalized over the full simulation cell with local functionals, whereas it localizes on a single water molecule with Hartree-Fock exchange. Hybrid functionals with varying amounts of exchange yield intermediate degrees of localization. This is illustrated in Fig. 7.2 for a bulk sample of liquid water (64 molecules), where the localization of the spin density is shown as a function of the amount of HFX in the PBE0 functional.

As quantitative measure, the maximum value of the Mulliken spin population is reported, ranging from approximately 0.1 in the local functional,

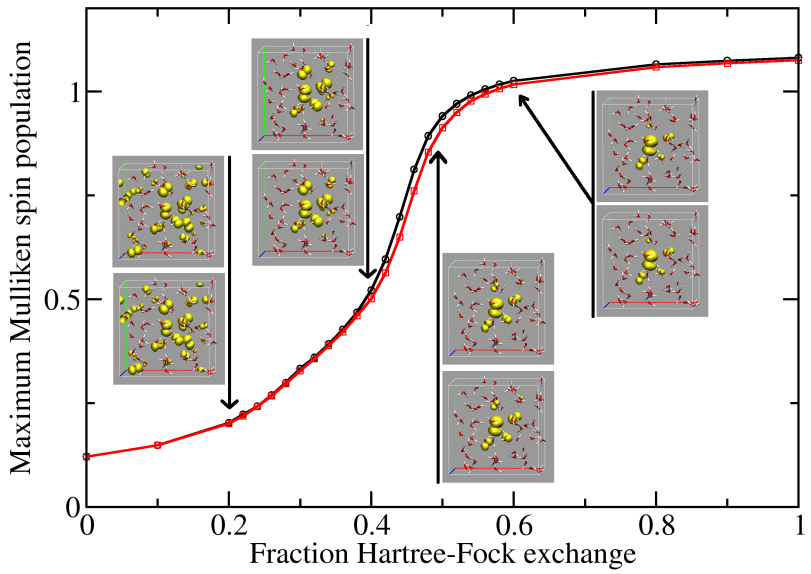

Figure 7.2: Shown is the localization of the spin density distribution after ionization of bulk liquid water as a function of the fraction of Hartree-Fock exchange employed in the density functional. The Mulliken spin populations of the oxygen atom on which the hole localizes is shown with a solid line, while the insets show a contour plot at 0.001 a.u. of the spin density for selected fractions (0.2, 0.4, 0.5, and 0.6) of exchange. Results obtained with the auxiliary FIT3 basis (black line, and upper panels of the inserts) are almost indistinguishable from the results obtained with the primary basis only, despite the pronounced sensitivity of this system towards the use of Hartree-Fock exchange.

to more than 1.0 in a functional containing 100% HFX. Contour plots of the spin density distribution emphasize this radical change in the electronic structure. Given this very strong dependence on the amount of Hartree-Fock exchange, this is a very stringent test for the auxiliary basis method presented in this work. Furthermore, this calculation has been performed with the relatively small FIT3 basis, i.e. without polarization functions. The results shown in Fig. 7.2 are therefore very reassuring, since the spin distribution obtained with the auxiliary basis set approach essentially reproduces the reference density in all details for all fractions of exchange.

method	number of integrals	gap [eV]
PBE (PBS)	-	4.17
PBE (ABS)	-	4.37
PBE0 (PBS)	40'787'850'778'591	6.07
PBE0 (ABS)	23'561'509'497	6.25
PBE0 ADMM1	24'816'897'009	6.03
PBE0 ADMM2	24'795'460'638	6.02

Table 7.6: Shown are band gaps of diamond as obtained from different methods. All calculations have been performed using the 3 x 3 x 3 repetition of the basic unit cell in Γ–point approximation. For the hybrid PBE0 calculations, also the number of Cartesian integrals is shown. See text for details on the primary and auxiliary basis set ((PBS) and (ABS)). ADMM1 is purified wavefunction fitting and ADMM2 is non-purified wavefunction fitting.

7.3.6 Diamond band gap

Both wavefunction fitting methods (ADMM1 and ADMM2) have been benchmarked with respect to their capability of predicting the band gap in diamond. The basic cubic unit cell with lattice parameter $a = 3.576$ Å containing eight carbon atoms has been extended to a large super-cell in order to apply the Γ–point approximation. In a first step, PBE band gaps for super-cell sizes ranging from 1 x 1 x 1 to 6 x 6 x 6 repetitions of the basic unit cell have been determined with a high quality basis set. The band gap calculation was found to be converged for the 3 x 3 x 3 repetition, yielding a band gap of 4.17 eV in agreement with literature [175]. This super-cell has than been used to calculate the PBE0 reference band gap of this system applying the same high quality basis set. Since the condition number of the overlap matrix with the FIT3 basis is unfavorable in the case of bulk C ($1.7 \cdot 10^5$), an optimized FIT3 (optFIT3) basis has been constructed that served as ABS for the two wavefunction fitting methods. optFIT3 was obtained by minimization of the total energy of the PBE 2 x 2 x 2 super-cell with respect to the constraint of a well behaved overlap matrix (the final condition number is of order 10^2). This allows for rather loose screening thresholds (10^{-6}) and thus significantly reduces the amount of work in the Fock matrix construction. Results are summarized in Tab. 7.6. Both wavefunction fitting methods are in good agreement the reference band gaps of the PBE0 run in the high quality basis. In order to illustrate the cost savings, the total number of Cartesian integrals that needs to be calculated has been added to the table.

The ADMM calculations are by 3 orders of magnitude more efficient than the reference PBE0 run. Both methods give very similar results, suggesting that the approximate Kohn-Sham matrix Eq. 7.34 is a valid approximation.

7.3.7 Performance and embedding for large systems

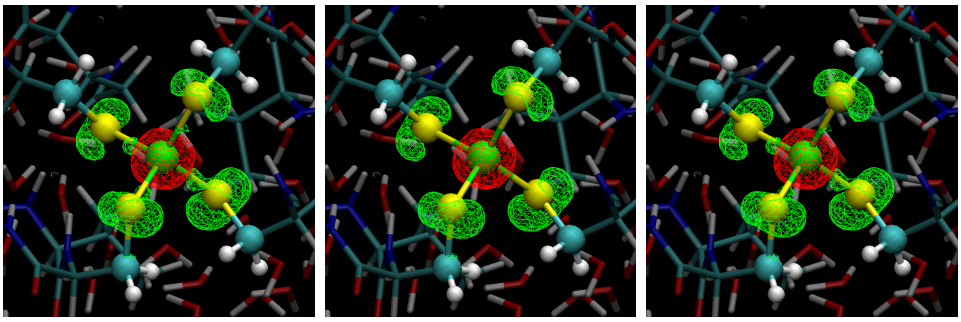

Figure 7.3: Shown are isosurfaces at +-0.001 a.u. of the difference between the spin density as computed with BLYP and B3LYP for the iron-sulfur protein Rubredoxin. Left panel: Traditional calculation using only a primary basis, middle panel: ADMM1 calculation using the cFIT3 auxiliary basis right panel: ADMM1 calculations using an embedding-like strategy, where the bulk of the system is described using the cFIT3 basis, but Fe and S use the primary basis as auxiliary basis. Both ADMM calculations clearly capture the effect of Hartree-Fock exchange, a reduced delocalization of the spin density, at a small fraction of the cost of the traditional approach. The embedding strategy faithfully reproduces all details, including the change in spin density along the Fe-S bonds.

In order to illustrate the impact of ADMM for large systems, the electronic structure of Rubredoxin has been computed. Rubredoxin is a relatively small iron-sulfur protein that is an excellent benchmark system for electronic structure calculations, since it features an interesting active site. A realistic model including solvent and using periodic boundary conditions comprises of only 2825 atoms and fits in a unit cell with edges 31.1 x 28.1 x 30.5 $Å^3$. This system has been used extensively in our earlier work. In Ref. [126], ab initio simulations of the full system have been combined with statistical sampling to quantify the effect of mutations on the redox potential of the active site. In Ref. [92], the feasibility of computing the electronic structure with accurate, molecularly optimized, basis sets has been demonstrated. In Ref. [95], hybrid density functional calculations using an all-electron description and a polarized triple zeta valence basis set [125] have been performed.

Molecularly optimized basis sets [92] have been employed as a primary basis for hybrid calculations (B3LYP [38, 24, 27]) of the same system, and the performance and accuracy of the ADMM scheme evaluated. Using a traditional HFX implementation with the MOLOPT basis set requires significant computational effort, despite the fact that the DZVP-MOLOPT-SR-GTH basis has been employed (22910 basis functions), which has fewer and less diffuse primitives than the basis sets originally presented in Ref. [92]. Indeed, the reference calculation has been run using 48000 cores on a Cray XT5. The first SCF step required 45 minutes to compute $3.7 \cdot 10^{14}$ primitive Cartesian integrals after screening with a threshold of 10^{-6}. Successive SCF steps spent only 25 seconds in the Hartree-Fock routines, since these calculations could be run in-core using integral compression [35] and 6.8Tb of RAM. Due to the contracted and diffuse nature of the basis sets, this calculation is significantly more expensive than the calculations performed in Ref. [95]. The difference in spin density between the B3LYP and a BLYP calculation is shown in the left panel of Fig. 7.3. ADMM1 calculations using the cFIT3 basis (12311 basis functions) require far fewer resources, and have been run on 1152 cores only. The Hartree-Fock routines used 75 seconds and 25 seconds in the first and successive SCF steps respectively, and in-core operation only required 5.2 Gb of RAM. The time spent in dense linear algebra for the wavefunction fitting (15s, Eq. 7.16) and corresponding derivative calculation (15s, Eq. 7.101) is similar to the time spent in the HFX, suggesting that this system might benefit from linear scaling techniques for this part of the calculation. For this system, ADMM thus improves the efficiency of the calculation by a factor 20 to 1000, depending on the measure. As shown in Fig. 7.3, the obtained spin density reproduces the reference calculation very well, even though some small differences near the Fe-S bond can be observed. To improve the accuracy, we have employed the simple embedding strategy in which the auxiliary basis for the five central atoms (Fe and S) was set equal to the primary basis. These calculations can be performed without any significant increase in computational cost, and the right panel of Fig. 7.3 shows that full quantitative agreement can be obtained in this way.

7.3.8 The effect of Hartree-Fock exchange on the structure of liquid water

In this section, ADMM is employed to study the effect of changing the fraction of Hartree-Fock exchange in the PBE0 functional on the structure of liquid water. Firstly, the accuracy of ADMM for describing bulk water is investigated. Secondly, we perform ab initio molecular dynamics simula-

tions based on ADMM for various values of the fraction of exchange. The model system is a sample of 64 water molecules in a cubic box with edges 12.42 Å that has previously been equilibrated using PBE0 [35]. The primary basis is in all cases a TZV2P basis (2560 basis functions in total). In order to investigate the accuracy of ADMM, the following procedure has been adopted. In a first step, a reference molecular dynamics trajectory of 2 ps starting from an equilibrated configuration has been produced. In a second step, 400 equipartitioned configurations have been chosen and for all of these single point ADMM calculations have been performed. The error has been quantified by computing the distribution of the difference between the reference energy and the ADMM energy. The important quantity is the variance of this difference, i.e. the energy fluctuations between the two potential energy surfaces. ADMM1 and ADMM2 have been benchmarked for various basis sets. ADMM3, which starts from a blocked density matrix, has been employed with blocked purification (Eq. 7.70) or full purification (Eq. 7.69). Non-purified ADMM3 was found to be unstable. The subsystems have been defined as containing exactly one water molecule per block, i.e. the whole system consists of 64 diagonal sub-blocks. As shown in Fig. 7.4, the fluctuations have approximately a Gaussian distribution. For ADMM1 and ADMM2, the associated variance gets consistently smaller when improving the quality of the auxiliary basis set. The variance for the purified wavefunction fitting (ADMM1) is slightly lower than the variance from non-purified wavefunction fitting (ADMM2). The variance of the energy fluctuations per water molecule is below 30 micro-Hartree for all auxiliary basis sets. This variance is significantly below the variance obtained applying the same procedure with a the pure density functional PBE, i.e. the difference between PBE0 and PBE is captured correctly with the ADMM1 and ADMM2 procedure. ADMM3 shows a relatively large variance, similar to direct use of the PBE functional, and its accuracy is not competitive.

With the aim of studying the effect of the fraction of exchange on the structure of the liquid, simulations employing the following functionals have been performed: PBE0 with various amounts of Hartree-Fock exchange ($\alpha \in \{0.12, 0.25, 0.37, 0.5, 0.62, 0.75, 1.00\}$), PBE, pure Hartree-Fock, PBE exchange (PBEx) and a revised parametrization [183] of PBEx (revPBEx). With these settings, trajectories longer than 30 ps have been obtained for all cases at a rate of 7 and 20 seconds per MD step (0.5 fs) for the pure and the hybrid functionals respectively on 64 cores of a Nehalem based cluster. Compared to a standard hybrid functional calculation in the PBS without ADMM and multiple time-step MD [35], this is a speed-up of a factor 16 per MD step. All MD simulations have been done within the isokinetic ensemble [184] at a temperature of 330 K, using ADMM1 and the FIT3 auxiliary basis. The structure

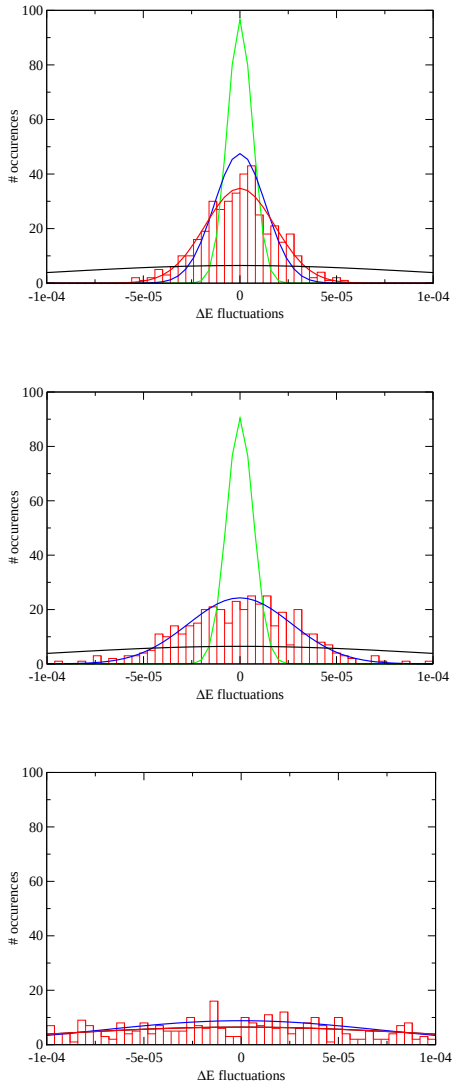

Figure 7.4: Shown are the centered distributions of energy differences (a.u.) between a standard PBE0 reference run and an ADMM method for bulk water. The top, middle, and bottom panel have been obtained with ADMM1, ADMM2, and ADMM3 respectively. ADMM1 and ADMM2 results have been computed using cFIT3 (red), FIT3 (blue), and aug-pFIT3 (green) auxiliary basis sets. ADMM3 employs blocking on a molecular level, with blocked (red) and full purification (blue). For clarity, Gaussian distributions are shown instead of binned data, except for one dataset per panel.

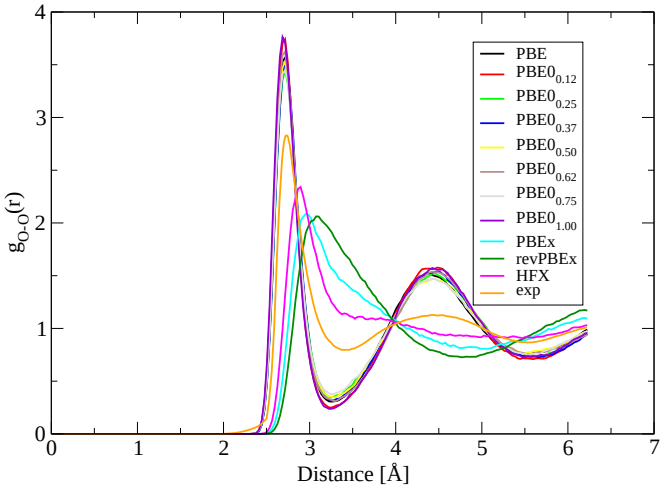

Figure 7.5: Oxygen-Oxygen pair correlation functions as obtained for bulk liquid water, based on a sample of 64 water molecules. Seven variants of PBE0, using various amounts of Hartree-Fock exchange, and PBE almost superimpose, but are overstructured as compared to the experimental result from Ref. [70]. PBE exchange (PBEx) only, revised PBE exchange (revPBEx) and pure Hartree-Fock yield pair correlations that are similar, and understructured as compared to experiment. A detailed comparison of the maximum values of the pair correlation functions is shown in Fig. 7.6.

has been analyzed using the oxygen-oxygen pair correlation function using the last 28 ps for each run, binning with a width of 0.03 Å. As shown in Fig. 7.5 PBE and all variants of PBE0 yield very similar pair correlation functions. Compared to experiment [70], the location of the peak is correct, but the liquid is overstructured. In order to quantify the structure, the maximum value of the pair correlation function is shown in Fig. 7.6. For PBE and all variants of PBE0 the height of the first peak falls in the range 3.45-3.75. There is no systematic trend with respect to the fraction of exchange, and the differences between the peak heights must be attributed to the limited statistics that can be collected within 30ps for a structured liquid. Within these statistical uncertainties, these ADMM results agree with the PBE0 results obtained using traditional HFX and the same basis in Ref. [35], where a maximum height of 3.4 was found for PBE and PBE0($\alpha = 0.25$) using 7.5ps of data. On the other hand, the liquid is significantly understructured for the pure Hartree-Fock, PBEx and revPBEx runs. The maximum pair cor-

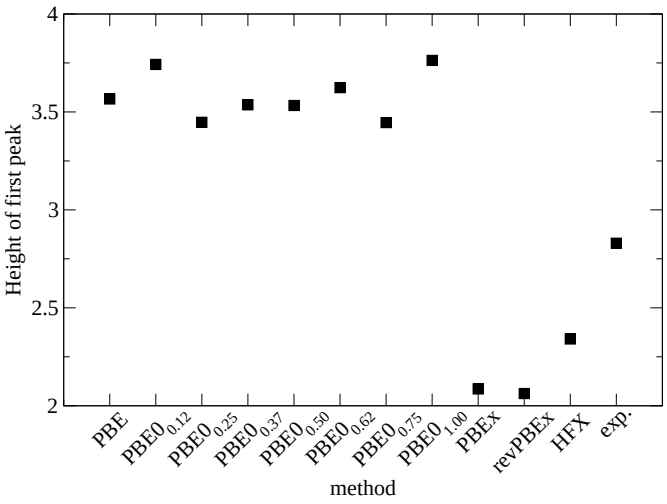

Figure 7.6: Shown is the height of the first peak for the oxygen-oxygen pair correlations shown in Fig. 7.5. For the variants of PBE0, no trend in peak height with respect to the fraction of exchange can be observed.

relation height obtained from the Hartree-Fock simulation is in agreement with the results in Ref. [90], 2.34 and 2.35 respectively, where a plane waves basis set has been employed. The large difference between a Hartree-Fock simulation and a PBE0($\alpha = 1.00$) simulation can only be attributed to the correlation functional, since all other terms in the Kohn-Sham equations are the same. Consistent with this and the observations made above, we find that the PBEx and revPBEx simulations, which do not include a correlation functional and employ a density functional to model exchange, qualitatively reproduce the Hartree-Fock simulations. The deviation between the Hartree-Fock and the revPBEx pair correlation function is somewhat larger than the deviation between the Hartree-Fock and the PBEx results. Finally, it is important to emphasize three limitations of our simulations. Firstly, due to the fact that the stress tensor is currently not implemented for hybrid functionals, these simulations have been performed at constant volume and not at constant pressure. In recent work, see e.g. Ref. [185] and Ref. [86], it has been shown that constant volume simulations might differ significantly from constant pressure simulations for this system. Indeed, the density of the liquid, and several other macroscopic quantities [186], most of them challenging to compute ab initio, might be more revealing about the quality of the underlying density functional than the pair correlation function. Secondly,

whereas the structure of the liquid is for the PBE0 functional not depending strongly on the fraction of exchange, this dependence might be different for other hybrid functionals. Thirdly, the fact that the structure of the liquid is effectively unchanged as the fraction of exchange is varied does not imply that the properties as a solvent, i.e. the interaction of the liquid with solutes is unchanged. In the future, the efficiency of ADMM might contribute to addressing some of these important issues.

7.4 Summary

We presented auxiliary density matrix methods that aim at reducing the cost of simulations based on hybrid density functionals. By constructing an approximate density matrix, which allows for a fast calculation of exchange, and by correcting the error introduced using a density functional, significant speedups have been achieved while accuracy has been retained. Wavefunction fitting methods that employ a small auxiliary basis to reduce the size of the density matrix appear to be a simple yet successful way to obtain an approximate density matrix. The accuracy of this approach has been investigated using a variety of tests. Calculations on the GMTKN24 database suggest that the predictivity of calculations based on wavefunction fitting essentially equals that of the more expensive traditional approach. Test calculations specifically aimed at difficult systems, such as BSSE calculations for the water dimer and the dissociation profile of H_2^+, have demonstrated that neither the deficiencies of the small auxiliary basis nor of the correcting functional impact the quality of the results significantly. Two variants of wavefunction fitting, either with purification (ADMM1) or without purification (ADMM2) have been tested, and no significant differences in accuracy have been found so far. Whereas ADMM1 has the advantage of yielding a pure auxiliary density matrix, ADMM2 is particularly simple to implement and is directly suitable for a linear scaling code. ADMM3, which relies on a blocking of the density matrix, has not been tested tho roughly yet, but might find its application in cases where clear subsystems, such as a solute in solution, can be easily defined. Exploiting the efficiency of the ADMM scheme, the effect of the range of exchange has been investigated for the PBE0-TC-LRC functional. The performance of this functional on the GMTKN24 database is optimal for 20% of exchange, and a range of 2.5Å. Furthermore, ADMM has been used to perform extensive simulations of bulk water, showing that for PBE0-like functionals the amount of Hartree-Fock exchange does not directly influence the structure of the liquid. In this case, the role of correlation is more significant. Finally, a calculation on a solvated protein has been used

to demonstrate that speedups in excess of a factor of twenty can be observed in actual applications.

7.5 Appendix

7.5.1 Wavefunction fitting

The one-particle wavefunctions represented with the high quality primary basis set (PBS) $\{\phi_\mu\}$ can be written in terms of molecular coefficients $C^{\mu i}$

$$\psi_i(\mathbf{r}) = \sum_\mu C^{\mu i}\phi_\mu(\mathbf{r}). \tag{7.35}$$

These wavefunctions are assumed to be orthonormal, i.e.

$$\int \psi_i(\mathbf{r})\psi_j(\mathbf{r})d\mathbf{r} = \delta_{ij}. \tag{7.36}$$

For the wavefunction fitting, a lower quality auxiliary basis set (ABS) $\{\hat{\phi}_\mu\}$ is introduced which yields a second set of molecular coefficients $\hat{C}^{\mu i}$ and auxiliary one-particle wavefunctions in the following form

$$\hat{\psi}_i(\mathbf{r}) = \sum_\mu \hat{C}^{\mu i}\hat{\phi}_\mu(\mathbf{r}). \tag{7.37}$$

The molecular coefficients $\hat{C}^{\mu i}$ are a priori unknown but can be determined by requiring that the corresponding occupied wavefunctions resemble as well as possible the original ones by minimizing their square difference over all space

$$\sum_j \int (\psi_j(\mathbf{r}) - \hat{\psi}_j(\mathbf{r}))^2 d\mathbf{r}. \tag{7.38}$$

Optionally, the auxiliary wavefunctions can be restricted to obey the orthonormality constraint

$$\int \hat{\psi}_i(\mathbf{r})\hat{\psi}_j(\mathbf{r})d\mathbf{r} = \delta_{ij}. \tag{7.39}$$

These two possibilities give raise two two slightly different minimization problems:

$$\min_{\hat{C}} \left[\sum_j \int \left(\psi_j(\mathbf{r}) - \hat{\psi}_j(\mathbf{r})\right)^2 d\mathbf{r} \right], \tag{7.40}$$

and

$$\min_{\tilde{C}} \left[\sum_j \int \left(\psi_j(\mathbf{r}) - \tilde{\psi}_j(\mathbf{r}) \right)^2 d\mathbf{r} + \sum_{k,l} \Lambda_{kl} \int \left(\tilde{\psi}_k \tilde{\psi}_l - \delta_{kl} \right) d\mathbf{r} \right], \quad (7.41)$$

where in the latter case, the Lagrangian multipliers Λ_{kl} enforce condition Eq. 7.39 and the notation $\tilde{C}$ has been introduce in order to distinguish the two different sets of molecular coefficients. The overlap matrices associated with the two basis set representations are given as

$$S_{mm'} = \int \phi_m(\mathbf{r}) \phi_{m'}(\mathbf{r}) d\mathbf{r} \quad \text{and} \quad \hat{S}_{nn'} = \tilde{S}_{nn'} = \int \hat{\phi}_n(\mathbf{r}) \hat{\phi}_{n'}(\mathbf{r}) d\mathbf{r}. \quad (7.42)$$

In order to retain a consistent notation, $\hat{S}$ and $\tilde{S}$ have been introduced, even though both matrices are identical. Furthermore, a mixed overlap matrix Q needs to be defined that takes the overlap of both sets of basis functions into account:

$$Q_{nm} = \int \hat{\phi}_n(\mathbf{r}) \phi_m(\mathbf{r}) d\mathbf{r}. \quad (7.43)$$

Within this notation, the Lagrange functions associated with the two minimization problems Eq. 7.40 and Eq. 7.41 can conveniently be expressed as

$$\hat{L} = \sum_j \left(\sum_{m,m'} C_{mj} C_{m'j} S_{mm'} + \sum_{n,n'} \hat{C}_{nj} \hat{C}_{n'j} \hat{S}_{nn'} - 2 \sum_{m,n} C_{mj} \hat{C}_{nj} Q_{nm} \right). \quad (7.44)$$

and

$$\begin{aligned} \tilde{L} \;=\; & \sum_j \left(\sum_{m,m'} C_{mj} C_{m'j} S_{mm'} + \sum_{n,n'} \tilde{C}_{nj} \tilde{C}_{n'j} \tilde{S}_{nn'} - 2 \sum_{m,n} C_{mj} \tilde{C}_{nj} Q_{nm} \right. \\ + \; & \left. \sum_{m,n} \sum_{k,l} \Lambda_{kl} \left(\tilde{C}_{nj} \tilde{C}_{mk} \tilde{S}_{nm} - \delta_{kl} \right) \right). \end{aligned} \quad (7.45)$$

Because of Eq. 7.36, or, equivalently $C^T S C = 1$ and due to Eq. 7.39 or $\tilde{C}^T \tilde{S} \tilde{C} = 1$ in the second case, this simplifies to

$$\hat{L} = \sum_j \left(\sum_{n,n'} \hat{C}_{nj} \hat{C}_{n'j} \hat{S}_{nn'} - 2 \sum_{m,n} C_{mj} \hat{C}_{nj} Q_{nm} \right) \quad (7.46)$$

and

$$\tilde{L} = -2 \sum_j \sum_{m,n} C_{mj} \tilde{C}_{nj} Q_{nm} + \sum_{k,l} \Lambda_{kl} \left(\tilde{C}_{nk} \tilde{C}_{ml} \tilde{S}_{nm} - \delta_{kl} \right), \quad (7.47)$$

respectively. From that, the unknown auxiliary molecular coefficients can be determined by taking the partial derivatives and equating them to zero. This yields

$$\frac{\partial \hat{L}}{d\hat{C}_{pq}} = -2(QC)_{pq} + 2(\hat{S}\hat{C})_{pq} \doteq 0 \tag{7.48}$$

and

$$\frac{\partial \tilde{L}}{d\tilde{C}_{pq}} = -2(QC)_{pq} + 2(\tilde{S}\tilde{C}\Lambda)_{pq} \doteq 0. \tag{7.49}$$

Thus, the final results for the MO coefficients are given by

$$\hat{C} = \hat{S}^{-1}QC \quad \text{and} \quad \tilde{C} = \tilde{S}^{-1}QC\Lambda^{-1}, \tag{7.50}$$

with the matrix of the Lagrangian multipliers

$$\Lambda = \left[(QC)^T \tilde{S}^{-1} QC\right]^{1/2}. \tag{7.51}$$

Defining $A := \hat{S}^{-1}Q = \tilde{S}^{-1}Q$ to be the projector between the PBS and ABS directly yields Eq. 7.12 and Eq. 7.16 presented in Sec. 7.2.2.

7.5.2 Purification

Most of the calculations that follow take advantage of the Cauchy integral theorem for matrix functions [172]. For an arbitrary matrix F, it states

$$f(F) = \frac{1}{2\pi i} \oint f(z) \frac{1}{zI - F} dz, \tag{7.52}$$

which, since

$$\frac{d}{dx}F^{-1} = -F^{-1}\frac{dF}{dx}F^{-1} \tag{7.53}$$

transforms into an explicit formula for the derivative of a matrix function

$$\frac{df(F)}{dx} = \frac{1}{2\pi i} \oint f(z) \frac{1}{F - zI} \frac{dF}{dx} \frac{1}{F - zI} dz. \tag{7.54}$$

Applying this formula, matrix function derivatives can be calculated through residues of its eigenvalues. Applying this to $f(x) = \Theta(z)$, where $\Theta(z)$ denotes the Heaviside function, the expression for the purified density matrix becomes

$$\tilde{P} = \hat{S}^{-1/2} \left[\frac{1}{2\pi i} \oint \frac{\Theta(z - 0.5)}{zI - \hat{S}^{1/2}\hat{P}\hat{S}^{1/2}} dz \right] \hat{S}^{-1/2} \tag{7.55}$$

or, after some rearrangements

$$\tilde{P} = \hat{S}^{-1}\left[\frac{1}{2\pi i}\oint \frac{\Theta(z-0.5)}{\hat{S}^{-1}z-\hat{P}}dz\right]\hat{S}^{-1}. \tag{7.56}$$

The evaluation of the contour integral can easily be performed via diagonalization. For that purpose, the following generalized eigenvalue problem needs to be solved:

$$\hat{P}R = \hat{S}^{-1}R\lambda, \tag{7.57}$$

where R defines the matrix containing the generalized eigenvectors of $\hat{P}$. Indeed, inserting $RR^{-1} = 1$ and $(\hat{S}^{-1}R)(\hat{S}^{-1}R)^{-1}$ from left and right into Eq. 7.56 gives

$$\begin{aligned}
\tilde{P} &= \hat{S}^{-1}\left[\frac{1}{2\pi i}\oint RR^{-1}\frac{\Theta(z-0.5)}{\hat{S}^{-1}z-\hat{P}}(\hat{S}^{-1}R)(\hat{S}^{-1}R)^{-1}dz\right]\hat{S}^{-1} \\
&= \hat{S}^{-1}R\left[\frac{1}{2\pi i}\oint \frac{\Theta(z-0.5)}{zI-D}dz\right]R^{-1} \\
&= \hat{S}^{-1}R\left[\frac{1}{2\pi i}\oint \frac{\Theta(z-0.5)}{zI-D}dz\right]R^{T}\hat{S}^{-1}
\end{aligned} \tag{7.58}$$

where in the last step, the relation $R^T\hat{S}^{-1}R = 1$ which is valid under the assumption that $\hat{P}$ is a symmetric matrix. The integral in brackets is evaluated using the Cauchy residue theorem and can be written in terms of a diagonal matrix L. Component-wise, this yields

$$L_{ii} = \frac{1}{2\pi i}\oint \frac{\Theta(z-0.5)}{z-\lambda_i}dz = \mathrm{Res}\left(\frac{\Theta(z-0.5)}{z-\lambda_i}, z=\lambda_i\right) = \Theta(\lambda_i - 0.5). \tag{7.59}$$

The final expression for $\tilde{P}$ is therefore

$$\tilde{P} = \hat{S}^{-1}RLR^T\hat{S}^{-1}. \tag{7.60}$$

In a similar fashion, the derivative of $\tilde{P}$ with respect to $\hat{P}$, that is needed in the expression for the Kohn-Sham matrix can be evaluated. After diagonalization of $\hat{P}$, this derivative reads

$$\frac{d\tilde{P}}{d\hat{P}} = \hat{S}^{-1}R\left[\frac{1}{2\pi i}\oint \Theta(z-0.5)\left(\frac{1}{D-zI}\right)R^{-1}\hat{S}\frac{d\hat{P}}{d\hat{P}}R\left(\frac{1}{D-zI}\right)dz\right]R^{-1}. \tag{7.61}$$

Again, the contour integral in brackets is computed via the Cauchy residue theorem. Since, in this case, the diagonal matrix D with the eigenvalues

appears twice, the result is now a matrix M that also contains off-diagonal elements

$$\begin{aligned} M_{kj} &= \frac{1}{2\pi i}\oint \frac{\Theta(z-0.5)}{(\lambda_k - z)(\lambda_j - z)}dz = \frac{1}{2\pi i}\oint g(z)dz \\ &= \mathrm{Res}(g,\lambda_k) + \mathrm{Res}(g,\lambda_j) \\ &= \begin{cases} \frac{\Theta(\lambda_k-0.5)-\Theta(\lambda_j-0.5)}{\lambda_k-\lambda_j}, & k \neq j \\ \delta(\lambda_k - 0.5), & k = j \end{cases}. \end{aligned} \tag{7.62}$$

The derivative Eq. 7.61 thus becomes

$$\frac{d\tilde{P}_{cd}}{d\hat{P}_{ef}} = \left[\hat{S}^{-1}R\left(M \otimes G_{ef}\right)R^{-1}\right]_{cd}, \tag{7.63}$$

with

$$G_{ef} = R^{-1}\hat{S}\frac{d\hat{P}}{d\hat{P}_{ef}}R. \tag{7.64}$$

This result can now be applied to the purified wavefunction fitting in order to obtain an expression for the Kohn-Sham matrix. In this case, $\hat{P}$ is a function of P, i.e. it holds that $\hat{P} = APA^T$ and the Kohn-Sham matrix written in terms of a derivative of the energy with respect to P is given as

$$\frac{d\tilde{E}[\tilde{P}]}{dP_{ab}} = \frac{d\tilde{E}}{d\tilde{P}_{cd}}\frac{d\tilde{P}_{cd}}{d\hat{P}_{ef}}\frac{d\hat{P}_{ef}}{dP_{ab}} = \tilde{K}_{cd}\frac{d\tilde{P}_{cd}}{d\hat{P}_{ef}}\frac{d\hat{P}_{ef}}{dP_{ab}}, \tag{7.65}$$

where implicit summation is assumed over same indices. The last derivative trivially amounts to

$$\frac{d\hat{P}_{ef}}{dP_{ab}} = \frac{d}{dP_{ab}}\left[APA^T\right]_{ef} = A_{ea}A_{fb}. \tag{7.66}$$

Under utilization of Eq. 7.63 this term simplifies to

$$\frac{d\tilde{E}[\tilde{P}]}{dP_{ab}} = \left[\left(A^T\tilde{S}R^{-1}\right)\left[\left(R^T\tilde{S}^{-1}\tilde{K}\tilde{S}^{-1}R^{-T}\right)\otimes M\right]R^TA\right]_{ab}. \tag{7.67}$$

Since $R^T\tilde{S}^{-1}R = 1$ this can be rewritten as

$$\frac{d\tilde{E}[\tilde{P}]}{dP} = A^TR\left[\left(R^T\tilde{S}^{-1}\tilde{K}\tilde{S}^{-1}R\right)\otimes M\right]R^TA. \tag{7.68}$$

If $\hat{P}$ is obtained from a blocking procedure, above expression needs to be filtered through B

$$\frac{d\tilde{E}[\tilde{P}]}{dP} = \left[A^T R \left[\left(R^T \tilde{S}^{-1} \tilde{K} \tilde{S}^{-1} R\right) \otimes M\right] R^T A\right] \otimes B \tag{7.69}$$

For the purification of the blocked density matrix, the McWeeny procedure based on the overlap matrix S can be replaced by a blocked McWeeny procedure where the overlap matrix is replaced by its blocked counterpart $S^\dagger = \hat{S} \otimes B$. Eq. 7.23 thus becomes

$$\bar{P}_{n+1} = f(\bar{P}_n) = 3\bar{P}_n S^\dagger \bar{P}_n - 2\bar{P}_n S^\dagger \bar{P}_n S^\dagger \bar{P}_n. \tag{7.70}$$

If the matrix B is chosen to be block diagonal, the eigenvalue problem Eq. 7.27 can thus be solved within the smaller diagonal subspaces only which significantly reduces the computational workload.

7.5.3 Wavefunction fitting with and without purification

As mentioned in Sec. 7.2.3 applying the purification scheme Eq. 7.23 to the density matrix $\hat{P}$ obtained from wavefunction fitting without the orthonormality constraint yields exactly the density matrix $\tilde{P}$ obtained through the fitting procedure including the constraint. This can easily be seen by plugging $\hat{P}$ into the McWeeny purification algorithm. The first two iterations amount to

$$\begin{aligned}
\bar{P}_1 &= 3\hat{P}\hat{S}\hat{P} - 2\hat{P}\hat{S}\hat{P}\hat{S}\hat{P} \\
&= 3\hat{C}\hat{C}^T\hat{S}\hat{C}\hat{C}^T - 2\hat{C}\hat{C}^T\hat{S}\hat{C}\hat{C}^T\hat{S}\hat{C}\hat{C}^T \\
&= 3\hat{C}\Lambda\hat{C}^T - 2\hat{C}\Lambda^2\hat{C}^T \\
&= \hat{C}\left(3\Lambda - 2\Lambda^2\right)\hat{C}^T =: \hat{C}g_1\hat{C}^T
\end{aligned} \tag{7.71}$$

and

$$\begin{aligned}
\bar{P}_2 &= 3\hat{P}_1\hat{S}\hat{P}_1 - 2\hat{P}_1\hat{S}\hat{P}_1\hat{S}\hat{P}_1 \\
&= 3\hat{C}\left(3\Lambda - 2\Lambda^2\right)\hat{C}^T\hat{S}\hat{C}\left(3\Lambda - 2\Lambda^2\right)\hat{C}^T \\
&- 2\hat{C}\left(3\Lambda - 2\Lambda^2\right)\hat{C}^T\hat{S}\hat{C}\left(3\Lambda - 2\Lambda^2\right)\hat{C}^T\hat{S}\hat{C}\left(3\Lambda - 2\Lambda^2\right)\hat{C}^T \\
&= 3\hat{C}g_1^2\Lambda\hat{C}^T - 2\hat{C}g_1^3\Lambda^2\hat{C}^T.
\end{aligned} \tag{7.72}$$

Recursively, that yields

$$\bar{P}_{n+1} = \hat{C}g_{n+1}\hat{C}^T, \tag{7.73}$$

with

$$g_{n+1} = 3g_n^2\Lambda - 2g_n^3\Lambda^2. \tag{7.74}$$

If the McWeeny procedure converges in the limit for $n \to \infty$, $g_n(\Lambda)$ is required to become a fixed point. Obviously this condition is fulfilled in the case of $g_n \to \Lambda^{-1}$, i.e.

$$\bar{P} = \hat{C}\Lambda^{-1}\hat{C}^T = \tilde{P}. \tag{7.75}$$

which matches exactly the corresponding equation for the purified wavefunction fitting.

7.5.4 Diagonalization in the occupied subspace for wavefunction fitting

As shown in App. 7.5.2, in order to obtain an expression for the Kohn-Sham matrix, a general eigenvalue problem of size N_{ABS}

$$\hat{P}R = \tilde{S}^{-1}R\lambda \tag{7.76}$$

needs to be solved. This might become the bottleneck in a ADMM calculation because N_{ABS} is not necessarily a small quantity. However, if $\hat{P}$ can be expressed in terms of molecular coefficients, as it is the case e.g. in wavefunction fitting, it is sufficient to diagonalize the occupied subspace only, which is typically much smaller than N_{ABS}. This can be achieved by introducing the following substitution $R \to R_\Lambda$:

$$R = \tilde{S}\hat{C}\Lambda^{-1/2}R_\Lambda = \tilde{S}\tilde{C}R_\Lambda. \tag{7.77}$$

Eq. 7.76 transforms thus into

$$\begin{aligned}
\hat{P}R &= \tilde{S}^{-1}R\lambda \\
\hat{C}\hat{C}^T R &= \tilde{S}^{-1}R\lambda \\
\hat{C}\hat{C}^T\tilde{S}\tilde{C}R_\Lambda &= \tilde{S}^{-1}\tilde{S}\tilde{C}R_\Lambda\lambda \\
\tilde{C}\Lambda^{1/2}\Lambda^{1/2}\tilde{C}^T\tilde{S}\tilde{C}R_\Lambda &= \tilde{C}R_\Lambda\lambda \\
(\tilde{S}\tilde{C})^T\tilde{C}\Lambda\tilde{C}^T\tilde{S}\tilde{C}R_\Lambda &= (\tilde{S}\tilde{C})^T\tilde{C}R_\Lambda\lambda \\
\Lambda R_\Lambda &= R_\Lambda\lambda,
\end{aligned} \tag{7.78}$$

where in the last step, the fact that $\tilde{C}\tilde{S}\tilde{C}^T = 1$ has been used. This eigenvalue problem is of the size $N_{mo} \times N_{mo}$ with N_{mo} the number of occupied orbitals in the system, and therefore significantly smaller in size than the general one. Unfortunately, its solution will only provide the eigenvectors of the occupied subspace

$$R_o = \tilde{S}\hat{C}\Lambda^{-1/2}R_\Lambda, \tag{7.79}$$

and the eigenvectors R_n for the null-space are unknown. However, since $RR^T = \tilde{S}$ it follows for the decomposition into occupied and unoccupied subspaces that

$$R_n R_n^T + R_o R_o^T = \tilde{S} \tag{7.80}$$

which motivates the notation $R = (R_n \quad R_o)$. Furthermore the matrix M has a very characteristic structure

$$M = \begin{pmatrix} M_n & M_{no} \\ M_{on} & M_o \end{pmatrix} \tag{7.81}$$

with

$$M_o = M_n = \begin{pmatrix} 0 & 0 & \dots \\ 0 & 0 & \dots \\ \vdots & \vdots & \end{pmatrix}, \quad M_{no} = M_{on}^T = \begin{pmatrix} M_{no} & M_{no} & M_{no} \dots \end{pmatrix}, \tag{7.82}$$

which directly follows from its definition in Eq. 7.62. Using this decomposition, Eq. 7.68 can be rewritten in terms of occupied and unoccupied parts:

$$\begin{aligned} \frac{d\tilde{E}[\tilde{P}]}{dP} &= A^T (R_n \quad R_o) \left[\begin{pmatrix} R_n^T \tilde{S}^{-1} \tilde{K} \tilde{S}^{-1} R_n & R_n^T \tilde{S}^{-1} \tilde{K} \tilde{S}^{-1} R_o \\ R_o^T \tilde{S}^{-1} \tilde{K} \tilde{S}^{-1} R_n & R_o^T \tilde{S}^{-1} \tilde{K} \tilde{S}^{-1} R_o \end{pmatrix} \otimes M \right] \cdot \\ &\cdot \quad (R_n \quad R_o)^T A \\ &= A^T (R_n \quad R_o) \begin{pmatrix} 0 & R_n^T \tilde{S}^{-1} \tilde{K} \tilde{S}^{-1} \tilde{R}_o \\ (R_n^T \tilde{S}^{-1} \tilde{K} \tilde{S}^{-1} \tilde{R}_o)^T & 0 \end{pmatrix} \cdot \\ &\cdot \quad (R_n \quad R_o)^T A, \end{aligned} \tag{7.83}$$

with $\tilde{R}_o$ denoting the eigenvectors of the occupied subspace with the columns scaled by the vectors M_{no}. This can further be simplified, yielding an expression that only depends on the eigenvectors R_o of the occupied subsystem:

$$\begin{aligned} \frac{d\tilde{E}[\tilde{P}]}{dP} &= A^T \begin{pmatrix} R_o \left(R_n^T \tilde{S}^{-1} \tilde{K} \tilde{S}^{-1} \tilde{R}_o \right)^T & R_n R_n^T \tilde{S}^{-1} \tilde{K} \tilde{S}^{-1} \tilde{R}_o \end{pmatrix} (R_n \quad R_o)^T A \\ &= A^T \left(R_o \tilde{R}_o^T \tilde{S}^{-1} \tilde{K} \tilde{S}^{-1} R_n R_n^T + R_n R_n^T \tilde{S}^{-1} \tilde{K} \tilde{S}^{-1} \tilde{R}_o R_o^T \right) A \\ &= A^T \Big(R_o \tilde{R}_o^T \tilde{S}^{-1} \tilde{K} \tilde{S}^{-1} (\tilde{S} - R_o R_o^T) \\ &\quad + (\tilde{S} - R_o^T R_o) \tilde{S}^{-1} \tilde{K} \tilde{S}^{-1} \tilde{R}_o R_o^T \Big) A. \end{aligned} \tag{7.84}$$

An explicit expression for the products $R_o\tilde{R}_o^T$ is still required. Again, due to the special structure of M, the matrix $\tilde{R}_o$ resulting from a column scaling of R_o with M_{no} can conveniently be obtained from the eigenvalues of Λ

$$\tilde{R}_o = R_o D_\Lambda^{-1} \tag{7.85}$$

where D_Λ contains the eigenvalues of the matrix Λ and fulfills $R_\Lambda D_\Lambda R_\Lambda^T = \Lambda$ and similarly $R_\Lambda D_\Lambda^{-1} R_\Lambda^T = \Lambda^{-1}$, yielding

$$\begin{aligned} R_o\tilde{R}_o^T &= \tilde{S}\hat{C}\Lambda^{-1/2}R_\Lambda(\tilde{S}\hat{C}\Lambda^{-1/2}R_\Lambda D_\Lambda^{-1})^T \\ &= \tilde{S}\hat{C}\Lambda^{-1/2}R_\Lambda D_\Lambda^{-1}R_\Lambda^T\Lambda^{-1/2}\hat{C}^T\tilde{S} \\ &= \tilde{S}\hat{C}\Lambda^{-1/2}\Lambda^{-1}\Lambda^{-1/2}\hat{C}^T\tilde{S} \\ &= \tilde{S}\hat{C}\Lambda^{-2}\hat{C}^T\tilde{S}. \end{aligned} \tag{7.86}$$

Inserting this result into Eq. 7.84 yields

$$\begin{aligned} \frac{d\tilde{E}[\tilde{P}]}{dP} &= A^T\Big(R_o\tilde{R}_o^T\tilde{S}^{-1}\tilde{K}\tilde{S}^{-1}(\tilde{S}-R_oR_o^T) \\ &\quad + (\tilde{S}-R_o^TR_o)\tilde{S}^{-1}\tilde{K}\tilde{S}^{-1}\tilde{R}_oR_o^T\Big)A \\ &= A^T\Big(\tilde{S}\hat{C}\Lambda^{-2}\hat{C}^T\tilde{S}\tilde{S}^{-1}\tilde{K}\tilde{S}^{-1}(\tilde{S}-R_oR_o^T) \\ &\quad + (\tilde{S}-R_o^TR_o)\tilde{S}^{-1}\tilde{K}\tilde{S}^{-1}\tilde{S}\hat{C}\Lambda^{-2}\hat{C}^T\tilde{S}\Big)A. \end{aligned} \tag{7.87}$$

For the last step, this equation needs to be back-transformed applying the substitution from Eq. 7.77. Since Λ is symmetric, its eigenvectors are orthonormal, i.e. $R_\Lambda R_\Lambda^T = 1$ and one finds

$$\begin{aligned} R_oR_o^T &= \tilde{S}\hat{C}\Lambda^{-1/2}R_\Lambda R_\Lambda^T\Lambda^{-1/2}\hat{C}^T\tilde{S} \\ &= \tilde{S}\hat{C}\Lambda^{-1}\hat{C}^T\tilde{S} = \tilde{S}\tilde{P}\tilde{S}. \end{aligned} \tag{7.88}$$

Thus, the final expression for the Kohn-Sham matrix is given as

$$\begin{aligned} \frac{d\tilde{E}[\tilde{P}]}{dP} &= A^T\Big(\tilde{S}\hat{C}\Lambda^{-2}\hat{C}^T\tilde{K}(1-\tilde{P}\tilde{S}) \\ &\quad + (1-\tilde{S}\tilde{P})\tilde{K}\hat{C}\Lambda^{-2}\hat{C}^T\tilde{S}\Big)A \end{aligned} \tag{7.89}$$

which indeed depends only on the inverse square of Λ which has the size $N_{\mathrm{mo}} \times N_{\mathrm{mo}}$ which can be evaluated through efficient Cholesky decomposition and does not require a diagonalization.

7.5.5 MO derivatives

For wavefunction optimization algorithms that do not rely on the existence of a Kohn-Sham matrix but rather utilize the MO derivatives

$$U = \frac{dE}{dC}, \tag{7.90}$$

such as the orbital transformation (OT) method [52] in `Quickstep` [14], the explicit construction of a Kohn-Sham matrix can be omitted. This is certainly the case for the purified wavefunction fitting because in that case the corresponding auxiliary density matrix can be obtained from molecular coefficients. Instead of calculating the derivative of the energy with respect to the density matrix, it is thus sufficient to compute the MO derivatives

$$U_{\text{total}} = \frac{dE[P]}{dC} + \frac{d\tilde{E}[\tilde{P}]}{dC}, \tag{7.91}$$

where only the second term is of interest here. Notice, that the auxiliary density matrix $\tilde{P}$ can be expressed either in terms of purified molecular coefficients

$$\tilde{P} = \tilde{C}\tilde{C}^T \quad \text{with} \quad \tilde{C} = \hat{C}\Lambda^{-1} = AC\Lambda^{-1} \tag{7.92}$$

or in terms of non-purified molecular coefficients

$$\tilde{P} = \hat{C}\Lambda^{-1}\hat{C}^T. \tag{7.93}$$

As a consequence, there exist two different approaches for calculating the desired MO derivative. The first method involves the auxiliary Kohn-Sham matrix

$$\frac{d\tilde{E}[\tilde{P}]}{dC} = \frac{d\tilde{E}}{dC} = \frac{d\tilde{E}}{d\tilde{P}}\frac{d\tilde{P}}{d\hat{C}}\frac{d\hat{C}}{dC} = \tilde{K}\frac{d\tilde{P}}{d\hat{C}}\frac{d\hat{C}}{dC}, \tag{7.94}$$

and the second method directly takes derivative of the energy with respect to the purified MO coefficients into account

$$\frac{d\tilde{E}[\tilde{P}]}{dC} = \frac{d\tilde{E}}{dC} = \frac{d\tilde{E}}{d\tilde{C}}\frac{d\tilde{C}}{dC} = \tilde{U}\frac{d\tilde{C}}{dC}, \tag{7.95}$$

with

$$\tilde{U} = \frac{d\tilde{E}[\tilde{P}]}{d\tilde{C}}. \tag{7.96}$$

The first case is algebraically straight forward, leading to

$$\frac{dE[\tilde{P}]}{dC} = 2\left(A^T\tilde{H}\hat{C}\Lambda^{-1}\right) - 2\left(A^T\tilde{S}\hat{C}\Lambda^{-1}\hat{C}^T\tilde{H}\hat{C}\Lambda^{-1}\right). \tag{7.97}$$

The second case is slightly more involved and requires the usage of the Cauchy integral formalism. The required derivative $\frac{d\tilde{C}}{dC}$ involves terms such as

$$\frac{d\Lambda^{-1/2}}{dC} \tag{7.98}$$

which can conveniently by expressed by

$$\frac{d\Lambda^{-1/2}}{dC} = \frac{1}{2\pi i}\oint f(z)\frac{1}{\Lambda - zI}\frac{d\Lambda}{dC}\frac{1}{\Lambda - zI}dz, \tag{7.99}$$

with $f(z) = z^{-1/2}$. For the evaluation of the contour integral, the matrix Λ needs to be diagonalized. Using the same notation as in Sec. 7.5.4, i.e. $R_\Lambda D_\Lambda R_\Lambda^T = \Lambda$ and D_Λ defined through the eigenvalues μ_i of Λ, the resulting matrix reads

$$\begin{aligned} N_{kj} &= \frac{1}{2\pi i}\oint \frac{z^{-1/2}}{(\mu_k - z)(\mu_j - z)}dz = \frac{1}{2\pi i}\oint g(z)dz \\ &= \mathrm{Res}(g, \mu_k) + \mathrm{Res}(g, \mu_j) \\ &= \begin{cases} \frac{\mu_k^{-1/2} - \mu_j^{-1/2}}{\mu_k - \mu_j}, & k \neq j \\ -\frac{1}{2}\mu_k^{-3/2}, & k = j \end{cases}. \end{aligned} \tag{7.100}$$

The final result for the MO derivatives is thus given by

$$\frac{d\tilde{E}[\tilde{P}]}{dC} = A^T\tilde{U}\Lambda^{-1/2} + Q^T AC(Y + Y^T), \tag{7.101}$$

with

$$Y = R_\Lambda\left(\left[R_\Lambda^T C^T A^T \tilde{U} R_\Lambda\right] \otimes N\right) R_\Lambda^T. \tag{7.102}$$

The first method, Eq. 7.97, has the advantage that only the inverse of Λ is needed whereas the second method, Eq. 7.101, requires the diagonalization of Λ.

7.5.6 Analytical ionic forces

The derivative of the energy with respect to the atomic positions $\mathbf{R}$

$$\frac{dE}{d\mathbf{R}} = \frac{dE[P]}{d\mathbf{R}} + \frac{d\tilde{E}[\tilde{P}]}{d\mathbf{R}} \tag{7.103}$$

can be calculated via the MO derivatives given in Eq. 7.101. That is, for the interesting term,

$$\frac{d\tilde{E}[\tilde{P}]}{d\mathbf{R}} = \frac{d\tilde{E}[\tilde{P}]}{d\tilde{C}}\frac{d\tilde{C}}{d\mathbf{R}} = \tilde{U}\frac{d\tilde{C}}{d\mathbf{R}}. \tag{7.104}$$

Component-wise, this yields

$$\frac{d\tilde{E}[\tilde{P}]}{d\mathbf{R}} = \tilde{U}_{ab}\left[\frac{dA}{d\mathbf{R}}C\Lambda^{-1/2}\right]_{ab} + \tilde{U}_{ab}\left[AC\frac{d\Lambda^{-1/2}}{d\mathbf{R}}\right]_{ab}, \tag{7.105}$$

where summation over same indices is assumed. In order to evaluate the second term, it is possible to apply the same mathematical formalism as in Eq. 7.99 and the final result reads

$$\begin{aligned}\frac{d\tilde{E}[\tilde{P}]}{d\mathbf{R}} &= -\tilde{U}_{ab}\left[\tilde{S}^{-1}\frac{d\tilde{S}}{d\mathbf{R}}\tilde{S}^{-1}QC\Lambda^{-1/2}\right]_{ab} \\ &\quad +\tilde{U}_{ab}\left[\tilde{S}^{-1}\frac{dQ}{d\mathbf{R}}C\Lambda^{-1/2}\right]_{ab} \\ &\quad +Y_{ab}\left[C^T\frac{dQ^T}{d\mathbf{R}}AC\right]_{ab} \\ &\quad -Y_{ab}\left[C^TQ^T\tilde{S}^{-1}\frac{d\tilde{S}}{d\mathbf{R}}\tilde{S}^{-1}QC\right]_{ab} \\ &\quad +Y_{ab}\left[C^TQ^T\tilde{S}^{-1}\frac{dQ}{d\mathbf{R}}C\right]_{ab},\end{aligned} \tag{7.106}$$

with Y_{ab} as in Eq. 7.102. This can further be simplified in terms of traces and becomes

$$\frac{d\tilde{E}}{d\mathbf{R}} = -\mathrm{tr}\left(W_{\tilde{S}}^T\frac{d\tilde{S}}{d\mathbf{R}}\right) + \mathrm{tr}\left(W_Q^T\frac{dQ}{d\mathbf{R}}\right), \tag{7.107}$$

with the weighted density matrices

$$W_{\tilde{S}} = \tilde{S}^{-1}\tilde{U}\Lambda^{-T/2}C^TA^T + ACYC^TA^T \tag{7.108}$$

and

$$W_Q = \tilde{S}^{-1}\tilde{U}\Lambda^{-T/2}C^T + ACY^TC^T + ACYC^T. \tag{7.109}$$

7.5.7 Eigenvalues

For purified wavefunction fitting, the Kohn-Sham matrix obtained through the McWeeny procedure or the Cauchy integral is not suitable for the calculation of orbital energies. This problem can be illustrated, by evaluating Eq. 7.89 for identical primary and auxiliary basis sets, i.e. $A = 1$, $\Lambda = 1$,

$\hat{C} = C$, $\tilde{S} = S$ and $\tilde{P} = CC^T$. In that case, the eigenvalues are given as

$$\begin{aligned} C^T \frac{d\tilde{E}[\tilde{P}]}{dP} C &= C^T \left[A^T (\tilde{S}\hat{C}\Lambda^{-2}\hat{C}^T\tilde{K}(1-\tilde{P}\tilde{S}) + (1-\tilde{S}\tilde{P})\tilde{K}\hat{C}\Lambda^{-2}\hat{C}^T\tilde{S})A \right] C \\ &= C^T \left[SCC^T\tilde{K} - SCC^T\tilde{K}PS + \tilde{K}CC^TS - SP\tilde{K}CC^TS \right] C \\ &= C^T\tilde{K}C - C^T\tilde{K}PS + C^T\tilde{K}C - SP\tilde{K}C \\ &= C^T\tilde{K}C - C^T\tilde{K}C + C^T\tilde{K}C - C^T\tilde{K}C, \end{aligned} \tag{7.110}$$

which is identically zero. Thus, Eq. 7.89 is not a suitable candidate for the calculation of the orbital energies and a different approach needs to be taken into account. The obvious choice is to derive a similar expression as in Eq. 7.33 for the non-purified wavefunction fitting, i.e. omitting the purification procedure. This assumption leads to the approximated Kohn-Sham matrix given in Eq. 7.34.

Chapter 8

Summary and Outlook

8.1 Summary

The first part of this work was dedicated to the development and implementation of a Hartree-Fock exchange kernel into the framework of the existing molecular dynamics package `CP2K`. In order to practically use the algorithms in the context of hybrid density functionals applied to large systems, the main focus was on linear scaling with respect to system size and parallel efficiency. The publication presented in Chapter 4 presents some results obtained from a first version of the algorithm. Extended molecular dynamics simulations of liquid water based on hybrid functionals and a multiple time-step algorithm have been performed with the conclusion, that the inclusion of exact exchange does not significantly improve structural properties. Furthermore, linear scaling behavior with respect to system size has been observed and reasonable parallel scalability up to 256 cores could be achieved.
The Γ–point approximation based on a method that only takes the largest exchange-energy contributions obtained from a minimum image convention in the basic super-cell into account was later found to be unstable, especially when higher quality basis sets are applied. In order to circumvent this problem, a new algorithm taking advantage of a truncated Coulomb operator has been developed and successfully applied to fairly large condensed phase systems. The publication in Chapter 5 illustrates how this approach solves the stability problem. In addition, a lot of effort has been spent in improving the parallel scalability of the method by fine-tuning the hybrid `MPI/openMP` implementation and by introducing a remarkably accurate cost model based on which the distribution of the workload can be achieved in a almost perfectly load balanced fashion.
Even though the construction of the Fock matrix scales linearly with in-

creasing system size, there is a large prefactor associated with the integral and density screening procedure. In order to reduce this prefactor, screening functions and data prefetching concepts have been introduced that allow for efficient treatment of exchange with much reduced overhead compared to a standard GGA calculation. The resulting code has been proven to run on the currently largest supercomputer available to the public and performs very well up to 64'000 cores and beyond.
Accuracy, stability and scalability could be shown by calculating the cohesive energy of a LiH crystal at the Hartree-Fock basis set limit. Chapter 6 presents results that have been obtained comparing this work and a different strategy based on short-range exchange and both techniques agreed to significant precision.

In the second part of this thesis, the slow-down of linear scaling algorithms in the presence of highly accurate basis sets has been addressed. Increasing the basis set quality has significant impact on the efficiency of screening based HFX algorithms. The associated screening thresholds need to be chosen tighter in the presence of more diffuse Gaussian basis functions which directly translates into more computational workload. In order to retain the efficiency of the highly optimized algorithms, auxiliary density matrix methods (ADMM) have been developed, that allow to mimic the effects of high quality basis sets by using an approximate description of the underlying density matrix. The publication introduced in Chapter 7 demonstrates the performance of this method by presenting data obtained from extensive benchmarking.

In summary, this work provides a very efficient framework to study large systems in gas and condensed phase within DFT using hybrid density functionals. Since nowadays most accurate approximations for the electron-electron interactions are based on a certain fraction of HFX, the resulting code will find applications in various fields in chemistry and solid-state physics.

8.2 Outlook

Although the parallelization of the Fock matrix construction is based on a hybrid `MPI/openMP` scheme, the communication involving of the two large matrices (density matrix and Fock matrix) will ultimately prevent scaling beyond 20'000 `MPI` tasks. In order to circumvent this problem, an algorithm that uses distributed versions of these matrices might be the solution. However, as mentioned in Chapter 3, retaining the quasi-optimal load balance of

the current implementation that takes the eight fold symmetry of the electron repulsion integrals (ERIs) into account is far from being straightforward. Of course, the symmetry criterion could by relaxed but this choice comes along with significant increase in memory requirement for the storage of already calculated ERIs and seems thus not very attractive.

Since General-purpose computing on graphics processing units (GPGPU) is becoming increasingly popular, a single precision variant of the current code would be of interest. An potentially successful ansatz would be to delegate the calculation of the ERIs to such a hardware or similar accelerator devices. Within the compression/decompression scheme it is typically sufficient to store the integrals with less than 32 bit precision and similarly it should be possible to evaluate them in single precision. Furthermore, the screening estimates for each bunch of integrals allows for automatic failure detection which is not possible on current graphics cards or similar hardware. Since the integral computation is one of the bottlenecks in a HFX calculation, significant speed-up can be expected from such an approach.

Some more work would need to be invested in order to extend the current scheme towards inclusion of perturbation theory based correlation effects. Methods such as MP2 basically rely on the same kernel routines for the ERI evaluation and the contraction with density matrix like structures. The main difficulty from a technical point of view emerges from the fact that the current ERI storage scheme is based on a simple first-in-first-out (FIFO) paradigm. An implementation of MP2 would require to access these data in variable ordering and an efficient method to communicate bunches of integrals among `MPI` processes would be needed. Once this is achieved, it should be straightforward to efficiently integrate periodic correlation effects into the current framework.

Bibliography

[1] Szabo, A. & Ostlund, N. S. *Modern Quantum Chemistry* (Dover Publications, Inc., Mineola, New York, 1996).

[2] Parr, R. G. & Yang, W. *Density-Functional Theory of Atoms and Molecules* (Oxford Science Publications, New York, 1989).

[3] Helgaker, T., Jørgensen, P. & Olsen, J. *Molecular Electronic Structure Theory* (John Wiley & Sons, Chichester, 2000).

[4] Born, M. & Oppenheimer, R. *Ann. Phys.-Berlin* **84**, 0457–0484 (1927).

[5] Roothaan, C. C. J. *Rev. Mod. Phys.* **23**, 69–89 (1951).

[6] Thomas, L. H. *Proc. Camb. Phil. Soc.* **23**, 542–548 (1927).

[7] Fermi, E. *Rend. Accad., Lincei* **6**, 602–607 (1927).

[8] Fermi, E. *Z. Phys.* **48**, 602–607 (1928).

[9] Fermi, E. *Rend. Accad., Lincei* **7**, 342–346 (1928).

[10] Hohenberg, P. & Kohn, W. *Phys. Rev. B* **136**, 864–871 (1964).

[11] Dirac, P. A. M. *Mathematical Proceedings of the Cambridge Philosophical Society* **26**, 376–385 (1930).

[12] Kohn, W. & Sham, L. J. *Phys. Rev. A* **140**, 1133 (1965).

[13] Lippert, G., Hutter, J. & Parrinello, M. *Theor. Chem. Acc.* **103**, 124–140 (1999).

[14] VandeVondele, J. *et al. Comput. Phys. Commun.* **167**, 103 (2005).

[15] Krack, M. & Parrinello, M. *Phys. Chem. Chem. Phys.* **2**, 2105–2112 (2000).

[16] Kudin, K. N. & Scuseria, G. E. *Phys. Rev. B* **61**, 16440–16453 (2000).

[17] Ahlrichs, R. *Phys. Chem. Chem. Phys.* **6**, 5119–5121 (2004).

[18] Harris, J. & Jones, R. O. *J. Phys. F* **4**, 1170–1186 (1974).

[19] Gunnarsson, O. & Lundqvist, B. I. *Phys. Rev. B* **13**, 4274–4298 (1976).

[20] Langreth, D. C. & Perdew, J. P. *Phys. Rev. B* **15**, 2884–2901 (1977).

[21] Harris, J. *Phys. Rev. A* **29**, 1648–1659 (1984).

[22] Ceperley, D. M. & Alder, B. J. *Phys. Rev. Lett.* **45**, 566–569 (1980).

[23] Becke, A. D. *Phys. Rev. A* **38**, 3098–3100 (1988).

[24] Lee, C., Yang, W. & Parr, R. G. *Phys. Rev. B* **37**, 785–789 (1988).

[25] Becke, A. D. *J. Chem. Phys.* **98**, 1372–1377 (1993).

[26] Becke, A. D. *J. Chem. Phys.* **98**, 5648 (1993).

[27] Vosko, S. H., Wilk, L. & Nusair, M. *Can. J. Phys.* **58**, 1200–1211 (1980).

[28] Perdew, J. P., Ernzerhof, M. & Burke, K. *J. Chem. Phys.* **105**, 9982–9985 (1996).

[29] Perdew, J. P., Ernzerhof, M. & Burke, K. *Int. J. Quantum Chem.* **64**, 285–295 (1997).

[30] Ernzerhof, M. & Scuseria, G. E. *J. Chem. Phys.* **110**, 5029–5036 (1999).

[31] Heyd, J., Scuseria, G. E. & Ernzerhof, M. *J. Chem. Phys.* **118**, 8207–8215 (2003).

[32] Heyd, J., Scuseria, G. E. & Ernzerhof, M. *J. Chem. Phys.* **124**, 219906 (2006).

[33] Obara, S. & Saika, A. *J. Chem. Phys.* **84**, 3963–3974 (1986).

[34] E. Valeev and J. T. Fermann. `http://www.chem.vt.edu/chem-dept/valeev/software/libint/libint.html` (2010).

[35] Guidon, M., Schiffmann, F., Hutter, J. & VandeVondele, J. *J. Chem. Phys.* **128**, 214104 (2008).

[36] The `CP2K` developers group. `http://cp2k.berlios.de/` (2010).

[37] Becke, A. D. & Johnson, E. R. *J. Chem. Phys.* **127**, 124108 (2007).

[38] Becke, A. D. *J. Chem. Phys.* **98**, 5648–5852 (1993).

[39] Gygi, F. & Baldereschi, A. *Phys. Rev. B* **34**, 4405–4408 (1986).

[40] Krukau, A. V., Vydrov, O. A., Izmaylov, A. F. & Scuseria, G. E. *J. Chem. Phys.* **125**, 224106 (2006).

[41] Cohen, A. J., Mori-Sanchez, P. & Yang, W. *J. Chem. Phys.* **126**, 191109–191109 (2007).

[42] Strout, D. L. & Scuseria, G. E. *J. Chem. Phys.* **102**, 8448–8452 (1995).

[43] Kohn, W. *Int. J. Quantum Chem.* **56**, 229–232 (1995).

[44] Goedecker, S. *Rev. Mod. Phys.* **71**, 1085–1123 (1999).

[45] Almlöf, J., Faegri, K. & Korsell, K. *J. Comp. Chem.* **3**, 385 (1982).

[46] Burant, J. C., Scuseria, G. E. & Frisch, M. J. *J. Chem. Phys.* **105**, 8969–8972 (1996).

[47] Schwegler, E. & Challacombe, M. *Theor. Chem. Acc.* **104**, 344–349 (2000).

[48] Ochsenfeld, C., White, C. A. & Head-Gordon, M. *J. Chem. Phys.* **109**, 1663–1669 (1998).

[49] Head-Gordon, M. & Pople, J. A. *J. Chem. Phys.* **89**, 5777–5786 (1988).

[50] Ahlrichs, R. *Phys. Chem. Chem. Phys.* **8**, 3072–3077 (2006).

[51] Izmaylov, A. F., Scuseria, G. E. & Frisch, M. J. *J. Chem. Phys.* **125**, 104103 (2006).

[52] VandeVondele, J. & Hutter, J. *J. Chem. Phys.* **118**, 4365–4369 (2002).

[53] Fülscher, M. P. & Widmark, P.-O. *J. Comp. Chem.* **14**, 8–12 (1992).

[54] Mitin, A. V., Baker, J., Wlinski, K. & Pulay, P. *J. Comp. Chem.* **24**, 154–160 (2002).

[55] de Leeuw, S. W., Perram, J. W. & Smith, E. R. *Proc. R. Soc. Lond. A* **373**, 27–56 (1980).

[56] Dovesi, R., Orlando, R., Roetti, C., Pisani, C. & Saunders, V. R. *Phys. Stat. Sol.* **217**, 63–88 (2000).

[57] Hammes-Schiffer, S. & Andersen, H. C. *J. Chem. Phys.* **101**, 375–393 (1994).

[58] Hedin, L. *Phys. Rev. A* **139**, 796–823 (1965).

[59] Tymczak, C. J., Weber, V., Schwegler, E. & Challacombe, M. *J. Chem. Phys.* **122**, 124105–124105 (2005).

[60] Tuckerman, M. E., Berne, B. J. & Martyna, G. J. *J. Chem. Phys.* **97**, 1990–2000 (1992).

[61] Anglada, E., Junquera, J. & Soler, J. M. *Phys. Rev. E* **68**, 055701 (2003).

[62] Martyna, G. J., Tuckerman, M. E., Tobias, D. J. & Klein, M. L. *Mol. Phys.* **87**, 1117–1157 (1996).

[63] Batcho, P. F. & Schlick, T. *J. Chem. Phys.* **115**, 4019–4029 (2001).

[64] Dunning, T. H. *J. Chem. Phys.* **90**, 1007–1023 (1988).

[65] Hashimoto, T., Hirao, K. & Tatewaki, H. *Chem. Phys. Lett.* **243**, 190–192 (1995).

[66] Davidson, E. R. *Chem. Phys. Lett.* **260**, 514–518 (1996).

[67] Gräfenstein, J., Kraka, E. & Cremer, D. *Phys. Chem. Chem. Phys.* **6**, 1096–1112 (2004).

[68] VandeVondele, J. & Sprik, M. *Phys. Chem. Chem. Phys.* **7**, 1363–1367 (2005).

[69] Soper, A. K. *Chem. Phys.* **258**, 121–137 (2000).

[70] Hura, G., Sorenson, J. M., Glaeser, R. M. & Head-Gordon, T. *J. Chem. Phys.* **113**, 9140–9148 (2000).

[71] Wernet, P. *et al. Science* **304**, 995–999 (2004).

[72] Leetmaa, M. *et al. J. Chem. Phys.* **125**, 244510 (2006).

[73] Rahman, A. & Stillinger, F. H. *J. Chem. Phys.* **55**, 3336 (1971).

[74] Laasonen, K., Sprik, M., Parrinello, M. & Car, R. *J. Chem. Phys.* **99**, 9080–9089 (1993).

[75] Sprik, M., Hutter, J. & Parrinello, M. *J. Chem. Phys.* **105**, 1142–1152 (1996).

[76] Silvestrelli, P. L. & Parrinello, M. *Phys. Rev. Lett.* **82**, 3308–3311 (1999).

[77] Vassilev, P., Hartnig, C., Koper, M. T. M., Frechard, F. & van Santen, R. A. *J. Chem. Phys.* **115**, 9815–9820 (2001).

[78] Izvekov, S. & Voth, G. A. *J. Chem. Phys.* **116**, 10372–10376 (2002).

[79] Asthagiri, D., Pratt, L. R. & Kress, J. D. *Phys. Rev. E* **68**, 041505 (2003).

[80] Chen, B., Ivanov, I., Klein, M. L. & Parrinello, M. *Phys. Rev. Lett.* **91**, 215503 (2003).

[81] Grossman, J. C., Schwegler, E., Draeger, E. W., Gygi, F. & Galli, G. *J. Chem. Phys.* **120**, 300–311 (2004).

[82] Kuo, I. F. W. *et al. J. Phys. Chem. B* **108**, 12990–12998 (2004).

[83] Fernandez-Serra, M. V. & Artacho, E. *J. Chem. Phys.* **121**, 11136–11144 (2004).

[84] VandeVondele, J. *et al. J. Chem. Phys.* **122**, 014515 (2005).

[85] Sit, P. H. L. & Marzari, N. *J. Chem. Phys.* **122**, 204510 (2005).

[86] McGrath, M. J. *et al. J. Phys. Chem. A* **110**, 640–646 (2006).

[87] Kuo, I. F. W., Mundy, C. J., McGrath, M. J. & Siepmann, J. I. *J. Chem. Theory Comput.* **2**, 1274–1281 (2006).

[88] McGrath, M. J., Siepmann, J. I., Kuo, I. F. W. & Mundy, C. J. *Mol. Phys.* **104**, 3619–3626 (2006).

[89] Lee, H.-S. & Tuckerman, M. E. *J. Chem. Phys.* **125**, 154507 (2006).

[90] Todorova, T., Seitsonen, A. P., Hutter, J., Kuo, I.-F. W. & Mundy, C. J. *J. Phys. Chem. B* **110**, 3685–3691 (2006).

[91] Mahoney, M. W. & Jorgensen, W. L. *J. Chem. Phys.* **112**, 8910–8922 (2000).

[92] VandeVondele, J. & Hutter, J. *J. Chem. Phys.* **127**, 114105 (2007).

[93] Mori-Sánchez, P., Cohen, A. J. & Yang, W. *to appear in Phys. Rev. Lett.* (2008).

[94] Peraro, M. D., Raugei, S., Carloni, P. & Klein, M. L. *Chem. Phys. Chem* **6**, 1715–1718 (2005).

[95] Guidon, M., Hutter, J. & VandeVondele, J. *J. Chem. Theory Comput.* **5**, 3010–3021 (2009).

[96] Perdew, J. P., Burke, K. & Ernzerhof, M. *Phys. Rev. Lett.* **77**, 3865–3868 (1996).

[97] Tao, J. M., Perdew, J. P., Staroverov, V. N. & Scuseria, G. E. *Phys. Rev. Lett.* **91**, 146401 (2003).

[98] Zhao, Y. & Truhlar, D. G. *Theor. Chem. Acc.* **120**, 215 (2008).

[99] Zhao, Y. & Truhlar, D. G. *J. Chem. Phys.* **125**, 194101 (2006).

[100] Zhao, Y. & Truhlar, D. G. *J. Phys. Chem. A* **110**, 13126 (2006).

[101] Zhao, Y. & Truhlar, D. G. *Acc. Chem. Res.* **41**, 157 (2008).

[102] Tymczak, C. J., Weber, V. T., Schwegler, E. & Challacombe, M. *J. Chem. Phys.* **122**, 124105 (2005).

[103] Spencer, J. & Alavi, A. *Phys. Rev. B* **77**, 193110 (2008).

[104] Ten-no, S. *J. Chem. Phys.* **126**, 014108 (2007).

[105] Pisani, C. & Dovesi, R. *Int. J. Quantum Chem.* **17**, 501–516 (1980).

[106] Wenzien, B., Cappellini, G. & Bechstedt, F. *Phys. Rev. B* **51**, 14701 (1995).

[107] Sorouri, A., Foulkes, W. M. C. & Hine, N. D. M. *J. Chem. Phys.* **124**, 064105 (2006).

[108] Carrier, P., Rohra, S. & Görling, A. *Phys. Rev. B* **75**, 205126 (2007).

[109] Ernzerhof, M. & Perdew, J. P. *J. Chem. Phys.* **109**, 3313–3320 (1998).

[110] Fousse, L., Hanrot, G., Lefèvre, V., Pélissier, P. & Zimmermann, P. *ACM Trans. Math. Softw.* **33**, 13 (2007).

[111] The `MPRF` Library. `http://www.mpfr.org` (2010).

[112] Caliari, M., Marchi, S. & Vianello, M. *ACM Trans. Math. Softw.* **35**, 1–11 (2008).

[113] The `CP2K` developers group. `http://cvs.berlios.de/cgi-bin/viewvc.cgi/cp2k/cp2k/tools/Fun2D/` (2010).

[114] Jensen, F. *J. Chem. Phys.* **115**, 9113 (2001).

[115] Jensen, F. *J. Chem. Phys.* **116**, 7372 (2002).

[116] Jensen, F. *J. Phys. Chem. A* **111**, 11198–11204 (2007).

[117] Lynch, B. J. & Truhlar, D. G. *J. Phys. Chem. A* **105**, 29362936 (2001).

[118] Lynch, B. J., Zhao, Y. & Truhlar, D. G. *J. Phys. Chem. A* **107**, 1384 (2003).

[119] Krack, M. *Theor. Chem. Acc.* **114**, 145–152 (2005).

[120] Gillan, M. J., Alfè, D., Gironcoli, S. & Manby, F. R. *J. Comp. Chem.* **29**, 2098 (2008).

[121] Manby, F. R., Alfè, D. & Gillan, M. J. *Phys. Chem. Chem. Phys.* **8**, 5178 (2006).

[122] Marsman, M., Grüneis, A., Paier, J. & Kresse, G. *J. Chem. Phys.* **130**, 184103 (2009).

[123] Paier, J. *et al. Phys. Rev. B* **80** (2009).

[124] Nolan, S. J., Gillan, M. J., Alfè, D., Allan, N. L. & Manby, F. R. *Phys. Rev. B* **80**, 165109 (2009).

[125] Schäfer, A., Huber, C. & Ahlrichs, R. *J. Chem. Phys.* **100**, 5829 (1994).

[126] Sulpizi, M., Raugei, S., VandeVondele, J., Carloni, P. & Sprik, M. *J. Phys. Chem. B* **111**, 3669 (2007).

[127] Stephens, P. J., Devlin, F. J., Chabalowski, C. F. & Frisch, M. J. *J. Phys. Chem.* **98**, 11623–11627 (1994).

[128] Dreizler, R. M. & Gross, E. K. U. *Density Functional Theory* (Springer Verlag, Berlin, 1990).

[129] Langreth, D. C. & Perdew, J. P. *Phys. Rev. B* **21**, 5469 (1980).

[130] Perdew, J. P. *et al. Phys. Rev. B* **46**, 6671 (1992).

[131] Becke, A. D. *J. Chem. Phys.* **98**, 1372 (1992).

[132] Marx, D. & Hutter, J. *Ab Initio Molecular Dynamics* (Cambridge University Press, Cambridge, 2009).

[133] Stroppa, A. & Kresse, G. *New J. Phys.* **10**, 063020 (2008).

[134] Paulus, B. *Phys. Rep.* **428**, 1 (2006).

[135] Janesko, B. G., Henderson, T. M. & Scuseria, G. E. *Phys. Chem. Chem. Phys.* **11**, 443 (2009).

[136] Pisani, C. *et al. J. Chem. Phys.* **122**, 094113 (2005).

[137] Pisani, C. *et al. J. Comput. Chem.* **29**, 2113 (2008).

[138] Casassa, S., Halo, M., Maschio, L., Roetti, C. & Pisani, C. *Theor. Chem. Acc.* **117**, 781 (2007).

[139] Ayala, P. Y. & Scuseria, G. E. *J. Comput. Chem.* **21**, 1524 (2000).

[140] Ayala, P. Y., Kudin, K. N. & Scuseria, G. E. *J. Chem. Phys.* **115**, 9698 (2001).

[141] Izmaylov, A. & Scuseria, G. *Phys. Chem. Chem. Phys.* **10**, 3421 (2008).

[142] Sun, J. & Bartlett, R. J. *J. Chem. Phys.* **104**, 8553 (1996).

[143] Frisch, M. J. *et al.* Gaussian Inc. Wallingford CT 2009.

[144] Kohn, W. *Phys. Rev.* **115**, 809 (1959).

[145] Cloizeaux, J. *Phys. Rev. A* **135**, 685 (1964).

[146] Baroni, S., Parravicini, G. P. & Pezzica, G. *Phys. Rev. B* **32**, 4077 (1995).

[147] Ayala, P. Y., Scuseria, G. E. & Savin, A. *Chem. Phys. Lett.* **307**, 227 (1999).

[148] Iyengar, S. S., Scuseria, G. E. & Savin, A. *Int. J. Quant. Chem.* **79**, 222 (2000).

[149] Press, W. H., Teukolsky, S. A., Vetterling, W. T. & Flannery, W. P. *Numerical Recipes in Fortran* (Cambridge University Press, Cambridge, 1992), 2nd edn.

[150] Murnaghan, F. D. *Proc. Natl. Acad. Sci. U.S.A.* **30**, 244 (1944).

[151] Heyd, J. & Scuseria, G. *J. Chem. Phys.* **121**, 1187 (2004).

[152] Paier, J. *et al. J. Chem. Phys.* **124**, 154709 (2006).

[153] Dovesi, R., Ermondi, C., Ferrero, E., Pisani, C. & Roetti, C. *Phys. Rev. B* **29**, 3591 (1984).

[154] Guidon, M., Hutter, J. & VandeVondele, J. *J. Chem. Theory Comput.* **6**, 2348–2364 (2010).

[155] Williamson, A. J. *et al. Phys. Rev. B* **55**, R4851–R4854 (1997).

[156] Kent, P. R. C. *et al. Phys. Rev. B* **59**, 1917–1929 (1999).

[157] Binkley, J. S., Pople, J. A. & Hehre, W. J. *J. Am. Chem. Soc.* **102**, 939–947 (1980).

[158] Pietro, W. J. *et al. J. Am. Chem. Soc.* **104**, 5039–5048 (1982).

[159] Harihara, P. C. & Pople, J. A. *Theoret. Chimica Acta* **28**, 213–222 (1973).

[160] Krishnan, R., Binkley, J. S., Seeger, R. & Pople, J. A. *J. Chem. Phys.* **72**, 650–654 (1980).

[161] Weigend, F. & Ahlrichs, R. *Phys. Chem. Chem. Phys.* **7**, 3297–3305 (2005).

[162] Weigend, F. *Phys. Chem. Chem. Phys.* **4**, 4285–4291 (2002).

[163] Boman, L., Koch, H. & de Merás, A. S. *J. Chem. Phys.* **129**, 134107 (2008).

[164] Sodt, A. & Head-Gordon, M. *J. Chem. Phys.* **128**, 104106 (2008).

[165] Liang, W. & Head-Gordon, M. *J. Phys. Chem. A* **108**, 3206–3210 (2004).

[166] Friesner, R. A. *Chem. Phys. Lett.* **116**, 39 – 43 (1985).

[167] Neese, F., Wennmohs, F., Hansen, A. & Becker, U. *Chem. Phys.* **356**, 98–109 (2009).

[168] Yanai, T., Fann, G. I., Gan, Z., Harrison, R. J. & Beylkin, G. *J. Chem. Phys.* **121**, 6680–6688 (2004).

[169] McWeeny, R. *Rev. Mod. Phys.* **32**, 335–369 (1960).

[170] Palser, A. H. R. & Manolopoulos, D. E. *Phys. Rev. B* **58**, 12704–12711 (1998).

[171] Niklasson, A. M. N., Tymczak, C. J. & Challacombe, M. *J. Chem. Phys.* **118**, 8611–8620 (2003).

[172] Rinehart, R. F. *Proc. Amer. Math. Soc* **7**, 2–5 (1956).

[173] Goedecker, S., Teter, M. & Hutter, J. *Phys. Rev. B* **54**, 1703–1710 (1996).

[174] Gómez-Abal, R., Li, X., Scheffler, M. & Ambrosch-Draxl, C. *Phys. Rev. Lett.* **101**, 106404 (2008).

[175] Duchemin, I. & Gygi, F. *Comput. Phys. Commun.* **181**, 855 – 860 (2010).

[176] Goerigk, L. & Grimme, S. *J. Chem. Theory Comput.* **6**, 107–126 (2010).

[177] Goerigk, L. & Grimme, S. `http://toc.uni-muenster.de/GMTKN/GMTKNmain.html` (2010).

[178] Grimme, S. *J. Comp. Chem.* **27**, 1787–1799 (2006).

[179] Boys, S. F. & Bernardi, F. *Mol. Phys.* **19**, 553 (1970).

[180] Ruzsinszky, A., Perdew, J. P. & Csonka, G. I. *J. Phys. Chem. A* **109**, 11006–11014 (2005).

[181] Sodupe, M., Bertran, J., Rodriguez-Santiago, L. & Baerends, E. *J. Phys. Chem. A* **103**, 166–170 (1999).

[182] Maršálek, O. *et al.* In preparation.

[183] Zhang, Y. & Yang, W. *Phys. Rev. Lett.* **80**, 890 (1998).

[184] McGrath, M. J. *et al. ChemPhysChem* **6**, 1894–1901 (2005).

[185] Schmidt, J. *et al. J. Phys. Chem. B* **113**, 11959–11964 (2009).

[186] Vega, C., Abascal, J. L. F., Conde, M. M. & Aragones, J. L. *Faraday Discuss.* **141**, 251–276 (2009).